Excited state dynamics of isolated DNA base pairs and related chromophore clusters

Inaugural-Dissertation
zur Erlangung des Doktorgrades
der Freien Universität Berlin
Fachbereich Physik

vorgelegt von
Elena Samoylova
aus Ust-Kamenogorsk, Kazakhstan
Berlin 2009

Tag der Prüfung: 22.06.2009

Gutachter dieser Arbeit:
1. Prof. Dr. I.V. Hertel
2. Prof. Dr. R. Bittl

Die Arbeit wurde durchgefuhrt am :
Max Born Institut für Nichtlineare Optik und Kurzzeitspektroskopie Berlin unter der Betreuung von Dr. Thomas Schultz

Kurzzusammenfassung

Der Gegenstand dieser Arbeit ist die Photophysik tiefliegender angeregter Zustände in den Chromophoren von DNS Bestandteilen, wie DNS-Basen, Basenpaaren und ihren Clustern mit Wassermolekülen. Die elektronische Struktur der angeregten Zustände wurde mit Hilfe der Femtosekunden Elektronen-Ionen Koinzidenzspektroskopie (FEICO) untersucht. Die Populationsdynamik dieser Zustände wurde mit Pump-Probe Methoden beobachtet. Die experimentellen Resultate wurden mit Hilfe von *ab initio* und semi-empirischen Rechnungen analysiert.

In dem Modellsystem 2-Aminopyridin Dimer ($(2\text{-AP})_2$) wurde ein intermolekularer Proton-gekoppelter Elektronentransfer detailliert untersucht. Die gleiche Reaktion wurde von der Theorie für Watson-Crick Basenpaare vorhergesagt and könnte eine Schlüsselrolle für die Photostabilität des genetischen Materials spielen.

In isolierten DNS Basen Adenin und Thymin werden die Spektroskopie und Dynamik durch Beiträge der tiefliegenden angeregten $\pi\pi^*$ und $n\pi^*$ Zustände dominiert. In Adenin zerfallen die angeregten Zustände innerhalb von 1 ps in den Grundzustand, wärend in Thymin ein Grossteil der Population innerhalb von 7 ps zerfällt. Die verbleibende Population in Thymin wurde als langlebig identifiziert (> 1 ns) und mit Hilfe von *ab initio* Rechnungen untersucht.

Im Adenin-Thymin Basenpaar wurde die Interpretation der Dynamik durch Clusterfragmentation erschwert. Die Zuordnung von zeitaufgelösten Signalen zu Adenin-Thymin, $(\text{Adenin})_2$ oder $(\text{Thymin})_2$ Clustern verlangte deswegen eine getrennte Untersuchung von $(\text{Adenin})_2$ und $(\text{Thymin})_2$ Homodimeren. In $(\text{Adenin})_2$ verläuft die Relaxation wie im Adenin-Monomer via $\pi\pi^*$ und $n\pi^*$ Zustände. In $(\text{Thymin})_2$ und Adenin-Thymine Clustern wurde zusätzlich ein neuer Relaxationprozess mit ~ 40 ps Lebensdauer identifiziert und einem Intermolekularzustand zugeordnet.

Methylierte Adenin und Thymin Basen zeigten zu unmethylierten Basen eine ähnliche Dynamik. Ein neuer Relaxationkanal wird in $(9\text{-Methyladenin})_2$ gefunden und mit der Existenz von Excimer Zuständen in gestapelter Clustergeometrie erklärt.

In $A(H_2O)_n$ Clustern wurde eine beschleunigte Relaxationdynamik beobachtet. Möglicherweise spielen $\pi\sigma^*$ Zustände eine Rolle in der Relaxation dieser Clustern.

Im Gegensatz dazu wurde in $A_2(H_2O)_n$ ($n \geq 2$) Clustern eine langlebiger angeregter Zustand mit einer ns Lebensdauer gefunden. Dieser Zustand könnte ein Excimer Zustand in gestapelter Clustergeometrie sein.

Abstract

The subject of this thesis is the photophysics of low-lying excited electronic states of simple DNA constituents, such as bases, base pairs, and their clusters with water. The electronic structure of excited states was determined by means of femtosecond electron-ion coincidence (FEICO) spectroscopy. The population dynamics of these states was investigated using a pump-probe method. The obtained experimental results were analyzed with the help of *ab initio* and semi-empirical calculations.

In a model system 2-aminopyridine dimer ($(2\text{-AP})_2$), an intermolecular proton-coupled electron transfer reaction was investigated in detail. The same reaction type was predicted to play a key role in photostability of DNA Watson-Crick base pairs.

In the isolated DNA bases adenine and thymine, contributions of two low-lying $\pi\pi^*$ and $n\pi^*$ excited states dominated the spectroscopy and the excited state dynamics. In adenine, the excited states completely decayed to the ground state within 1 ps, whereas in thymine, most of population decayed within 7 ps. The remaining signal in thymine dynamics was found to be long-lived (>1 ns), but the character of this state can only be discussed in context of *ab initio* calculations.

In adenine-thymine base pairs, the interpretation of the excited state dynamics was hampered by fragmentation of the clusters. The assignment of transients to the adenine-thymine, $(\text{adenine})_2$ or $(\text{thymine})_2$ clusters, therefore had to rely on a separate investigation of $(\text{adenine})_2$ and $(\text{thymine})_2$ homodimers. In $(\text{adenine})_2$, excited state relaxation proceeded via the $\pi\pi^*$ and $n\pi^*$ states, similar to adenine. No additional dynamic processes due to intermolecular interactions were found. In $(\text{thymine})_2$ and adenine-thymine clusters again, the characteristic features of the base monomers were found. Additionally, new relaxation processes with ∼40 ps life time were identified and assigned to a dimer state.

Methylated adenine and thymine exhibited similar dynamics to the nonmethylated bases. A new excited state transient was found in $(\text{9-methyladenine})_2$ and was tentatively assigned, based on theoretical calculations in literature, to a stacked cluster geometry.

In $\text{A}(\text{H}_2\text{O})_n$ clusters, acceleration of the excited state dynamics was observed. This was explained by the quenching of transients with $n\pi^*$ character and the observation of only one excited state of $\pi\pi^*$ character. Additionally, the role of a $\pi\sigma^*$ state was discussed.

In contrast to the $\text{A}(\text{H}_2\text{O})_n$ clusters, a longer-lived excited state with a ns life time was found in the $\text{A}_2(\text{H}_2\text{O})_n$ ($\geq$2) clusters. The appearance of this state was assigned to a structural change of the clusters from a planar to a stacked geometry.

Publications

T. Schultz, E. Samoylova, W. Radloff, H.-H. Ritze, *"Observation of proton transfer in 2-aminopyridine dimer by electron and mass spectroscopy"*(submitted to JPC A).

J. González-Vázquez, L. González, E. Samoylova, T. Schultz, *"Thymine relaxation after UV irradiation: the role of tautomerization and $\pi\sigma^*$ states"*, Phys. Chem. Chem. Phys. **11**,(2009), 3927-3934.

E. Samoylova, T. Schultz, I. V. Hertel, W. Radloff, *"Analysis of ultrafast relaxation in photoexcited DNA base pairs of adenine and thymine"*, Chem. Phys. **347**, (2008), 376-382.

N. Gador, E. Samoylova, V. R. Smith, A. Stolow, D. M. Rayner, W. Radloff, I. V. Hertel, and T. Schultz, *"Electronic structure of adenine and thymine base pairs studied by femtosecond electron-ion coincidence spectroscopy"*, J. Phys. Chem. A **111**, (2007), 11743-11749.

E. Samoylova, V. R. Smith, H.-H. Ritze, W. Radloff, M. Kabeláč, and T. Schultz, *"Ultrafast deactivation processes in aminopyridine clusters: excitation energy dependence and isotope effect"*, J. Am. Chem. Soc. **128**, No.49, (2006), 15652-15656.

Elena Samoylova, V. R. Smith, H.-H. Ritze, W. Radloff, V. I. Hertel, Thomas Schultz, *"Photochemistry and dynamics of base pairs"*, Proceedings of VIIth International Conference on Femtochemistry: Fundamental Ultrafast Processes in Chemistry, Physics, and Biology, Washington, DC, USA, (2006), 367-371.

H.-H. Ritze, H. Lippert, E. Samoylova, V. R. Smith, I. V. Hertel, W. Radloff, and T. Schultz, *"Relevance of $\pi\sigma^*$ states in the photoinduced processes of adenine, adenine dimer, and adenine-water complexes"*, J. Chem. Phys. **122**, (2005), 224320.

E. Samoylova, H. Lippert, S. Ullrich, W. Radloff and T. Schultz, *"Dynamics of photoinduced processes in adenine and thymine base pairs"*, J. Am. Chem. Soc. **127**, (2005), 1782-1786.

Thomas Schultz, Elena Samoylova, Wolfgang Radloff, Ingolf V. Hertel, Andrzej L. Sobolewski, Wolfgang Domcke *"Efficient deactivation of a model base pair via excited-state hydrogen transfer"*, Science **306**, (2004), 1765-1768.

Table of Contents

List of Figures

List of Tables

List of Abbreviations

2-AP - 2-aminopyridine
7-AI - 7-azaindole
A-T - adenine-thymine
CASSCF - complete-active-space self-consistent field
CASPT2 - complete-active-space second-order perturbation theory
CC - coupled cluster
CI - conical intersection
CIS - configuration interaction with single electron excitation
CIPSI - multireference perturbation configuration interaction
CD - cluster distribution
CPA - chirped pulse amplification
CPD - cyclobutane pyrimidine dimer
CT - charge transfer
DNA - deoxyribonucleic acid
DPT - double-proton transfer
EKE - electron kinetic energy
ES - excited state
FEICO - femtosecond electron-ion coincidence
FROG - frequency-resolved optical gating
G-C - guanine-cytosine
GS - ground state
HOMO - highest occupied molecular orbital
HV - high voltage
IB - iodobenzene
IC - internal conversion
IP - ionization potential
LE - locally excited
LUMO - lowest unoccupied molecular orbital
MCP - multi-channel plate
MRPT2 - multireference second-order perturbation theory
PC - polarizable continuum

PCET - proton-coupled electron transfer
PD - photodiode
PES - potential energy surface
PM3 - parametric method 3
R2PI - resonant two-photon ionization
RI-MP2 - second-order resolution-of-the-identity Møller-Plesset
REMPI - resonance enhanced multiphoton ionization
SPT - single proton transfer
SPIDER - spectral phase interferometry for direct electric-field reconstruction
TDC - time-to-digital converter
TDDFT - time-dependent density functional theory
TOF - time-of-flight
TOPAS - travelling-wave parametric amplifier of superfluorescence
WC - Watson-Crick

Chapter 1

Introduction

This work describes the photoinduced excited state dynamics of isolated DNA bases, base pairs and the model system 2-aminopyridine dimer. Additionally, the effects of microhydration on the excited state dynamics of the bases and base pairs were studied. The aim of the work is to improve the current understanding of fundamental processes in isolated biomolecules in the gas phase as well as intermolecular interactions in small clusters in presence or absence of a microenvironment.

Photoinduced processes in biologically relevant molecules under isolated conditions were a subject of extensive investigations in the last years (see e.g.[1, 2]). Gas phase research, as compared to condense phase studies, has the advantage to extract direct information about inherent properties of biological molecules, avoiding the complexity introduced by the environment. Complex systems can be understood by extrapolating results about small model systems following a so called "reductionist approach". This approach implies the ability to use a detailed knowledge about intra- and intermolecular interactions, dynamics, molecular conformations, and functions in isolated molecules to build a systematic understanding of complex biomolecular assemblies in the condense phase and in vivo. Moreover, the results of experiments in the gas phase can be directly compared with highly developed quantum-chemical *ab initio* or DFT calculations, which inherently describe molecular features in vacuo.

Photoinduced chemical reactions in biologically relevant molecules can take place on the time scales of several femtoseconds (1 fs = 10^{-15} s) to many milliseconds (1 ms = 10^{-3} s). The fastest of these processes can be nowadays characterized in real time using "pump-probe" methods based on Ti:Sa lasers [3]. These laser sources can generate pulses with a duration of <10 fs, providing the necessary time resolution for "pump-probe" experiments. A "pump" laser pulse, in such experiments, excites

molecules to a transient state, the dynamics of which is of interest. A "probe" pulse is used to detect the population of the state which was excited. By varying the time delay between the pump and the probe pulses, one can measure the decay of the population from the transient state and determine the life time of this state. Ionization spectroscopy is a common method for pump-probe experiments in the gas phase ([3–5]).

In the presented work, femtosecond pump-probe spectroscopy with ion and electron detection was used to study excited state dynamics in isolated DNA bases, base pairs and their microhydrated clusters. The electronically excited states may be involved in the complex reaction chain which lead to DNA photodamage and may thus impair the biological function of DNA which consists of carrying and protecting genetic information in living organisms. Solar UV radiation ($\lambda < 400$ nm [6]) can damage DNA and destroy the genetic information. Absorption of a UV photon with the energy of 4-5 eV populates electronic excited states and can initiate photochemical reactions causing photodamage. However, DNA exhibits very high photostability, perhaps due to selection pressure during a long period of molecular evolution, i.e., being under photochemical attack for billions of years. One key property leading to this remarkable photostability of DNA could be the rapid decay of the electronic excited states to the stable ground state.

Femtosecond spectroscopy allowed us to study these fast decay mechanisms in DNA constituents. To avoid the complexity of real DNA, a "reductionist approach" (fig. 1.1) was used. Simple building blocks of life (DNA bases) were investigated first. As the next step, the photophysics of DNA base pairs, starting with the model system 2-aminopyridine dimer, was studied. And, finally, it was shown how a microenvironment (several water molecules) affects the excited state properties of bases and base pairs.

Details of the obtained results are described in the following chapters:

- **Chapter 2** describes the experimental methods which were used. The principles of molecular beam experiments will be introduced first, followed by a description of mass and electron detection, as well as the coincidence measurements. Although all experiments were carried out in the vacuum apparatus built by V. Stert and W. Radloff at the MBI in the previous years, several new aspects were introduced to optimize the setup for gas phase experiments of DNA bases. Characteristics of the fs laser systems at the MBI will be given briefly. The data acquisition and evaluation methods will be presented at the

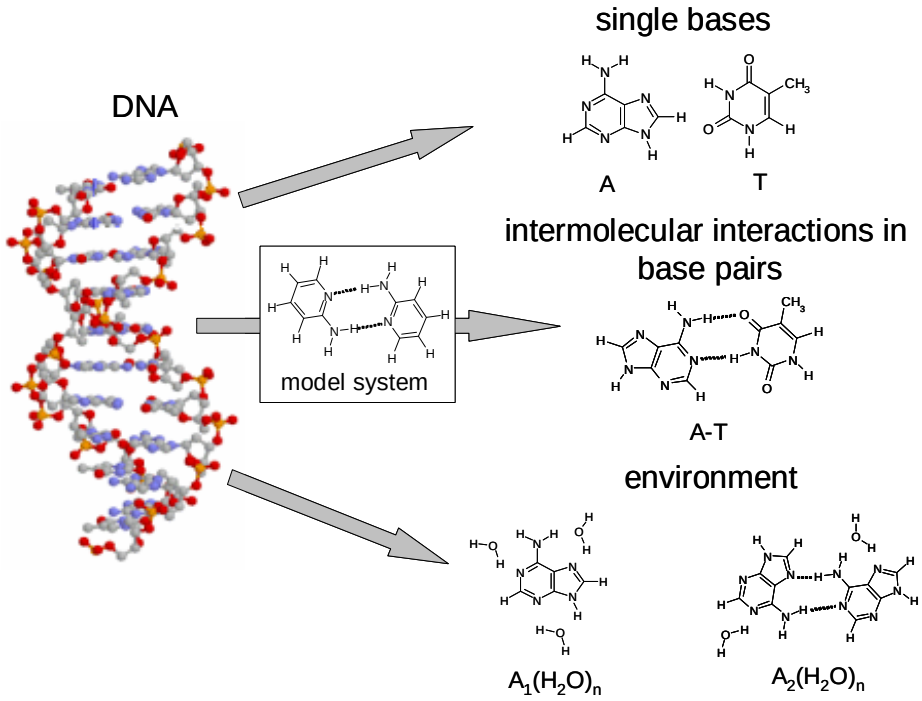

Figure 1.1: Learning pathway to understand important photophysical properties of the excited states of DNA. To avoid complexity of real DNA a "reductionists approach" was used. Based on this approach we tried to understand first the photophysics of single bases, then base pairs and microhydrated clusters.

end of the chapter.

- Experimental results obtained for 2-aminopyridine (2-AP) clusters are shown in **Chapter 3**. The dimer of this molecule was chosen as a model system for hydrogen-bound DNA base pairs. The presented results were in a perfect agreement with *ab initio* calculations on $(2\text{-AP})_2$ by A. Sobolewski and W. Domcke [7]. Additionally, spectroscopy of the 2-AP monomer and bigger clusters will be discussed. Absence of isomers in the gas phase and sufficient evaporation of 2-AP at low temperatures resulted in easier experiments as compared to the study of DNA bases and base pairs.

- **Chapter 4** begins with the mass and electron spectroscopy of the excited states in the isolated DNA bases adenine (A), thymine (T). The obtained results for each base were in good agreement with literature data. Results on the DNA base pair A-T are also presented. A novel relaxation process was observed and

assigned tentatively.

- **Chapter 5** treats the effects of microhydration. Clusters of adenine and thymine monomers, as well as adenine dimer with a few water molecules were investigated. Drastical changes in the excited state dynamics of hydrated monomers and dimers were revealed in the experiments and were assigned to structural changes in the cluster.

- **Chapter 6** describes excited state dynamics in methylated adenine, thymine, and their dimers. Methylated A and T could be a closer mimics of corresponding nucleosides and nucleotides. The obtained results were similar to those for nonmethylated A and T clusters.

- **Chapter 7** gives an outlook on experimental developments. First attempts to introduce a hole-burning technique for isomer-selective measurements are presented.

- **Chapter 8** summarizes the results of this work.

Chapter 2

Experimental methods

This chapter describes the experimental techniques and methods which were used in this work. It contains sections about the molecular beam apparatus, mass and electron detection methods, pump-probe laser experiments, and data acquisition.

In fig. 2.1 a schematic view of the experimental apparatus is shown (more detailed view is given in Appendix A). The molecules were evaporated in a metal oven and then expanded through a pulsed valve into vacuum. The skimmed molecular beam was intersected by two laser pulses to excite and ionize the molecules. The created electrons and ions were detected by two time-of-flight spectrometers equipped with multi-channel plate (MCP) detectors. A detailed description of the experiment is given in the separate sections of this chapter.

2.1 Principles of molecular beam experiments

Molecular beam methods offer the opportunity to study molecules in a collision-free environment with negligible perturbations. At such experimental conditions we could investigate unique molecular properties. On the other hand, working with molecular beams, we could introduce well-defined perturbations in order to measure their effect (e.g. cluster formation). Additionally, molecular beam methods allow to work with cooled molecules where the initial population of states can be controlled by adjusting the beam temperature.

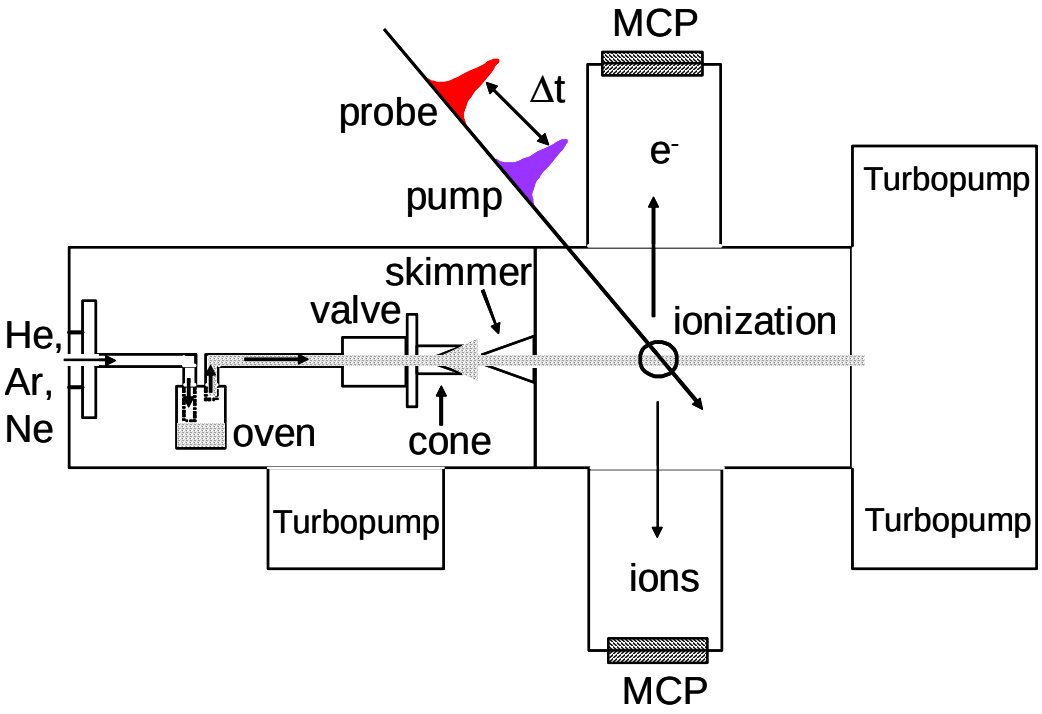

Figure 2.1: Schematic view of the experimental apparatus.

2.1.1 Molecular source and free-jet expansion

Solid samples (Sigma Aldrich, 99 % purity) were placed in a stainless steel oven and evaporated at $60 - 80\,^{\circ}\mathrm{C}$ (for 2-aminopyridine) and $200 - 220\,^{\circ}\mathrm{C}$ (for DNA bases). The evaporated molecules were expanded into vacuum through a 1 mm nozzle of a pulsed valve (General valve, series 9). Helium, argon or neon (0.7-2 bars) were used as carrier gases for expansion.

The principles of supersonic expansion will be briefly described below and refer to the fig. 2.2. More details can be found in ref. [8]. In the "high pressure region" of the expansion (see fig. 2.2), which corresponded to the heated nozzle in our experiments, the molecular is characterized by the initial pressure P_0 (1 bar) and the initial temperature T_0 ($200\,^{\circ}\mathrm{C}$). At these conditions many collisions take place and the velocities of molecules are slow and of random directions. When the molecules enter the "low pressure region" through a small orifice D, their velocities become nearly equalized in the direction of the gas flow. The expansion occurs, when the Mach number M becomes ≥ 1. M characterizes the ratio between the molecular velocity v and the speed of sound u. Due to a pressure difference between the "high and low

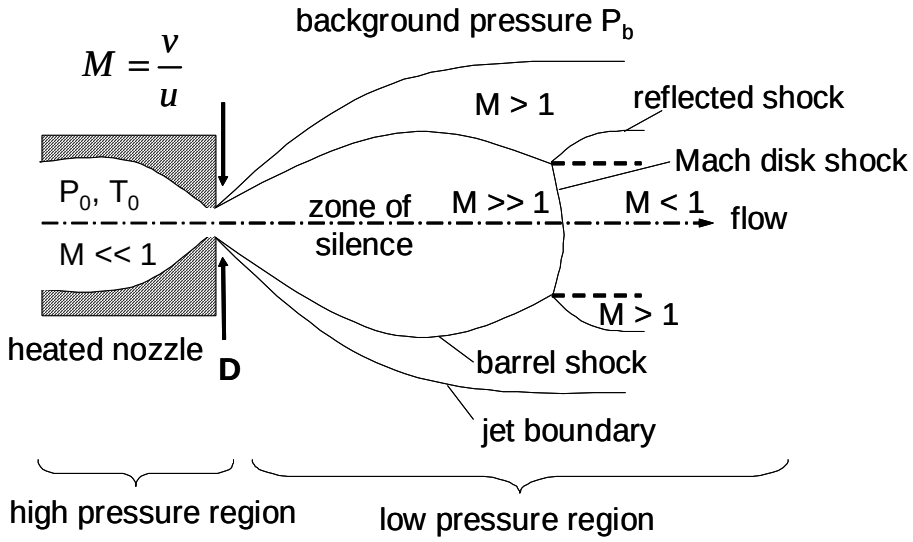

Figure 2.2: Schematic representation of a continuum free-jet expansion (reproduced from ref. [8]). Evaporated molecules with pressure and temperature P_0, T_0 are expanded into vacuum. The Mach number M characterizes the molecular beam velocity v relative to the local speed of sound u. The molecular beam is extracted from the "zone of silence". The shock-regions (barrel-shock, reflected shock, Mach disk shock) destroy the molecular beam.

pressure regions" (P_0-P_b), the gas flow accelerates to a supersonic speed. Since "information" propagates with the speed of sound, the flow, which moves faster, does not "know" about the boundary conditions (chamber walls) and the background pressure P_b. Because of this the gas can overexpand ($M \gg 1$) and therefore must be recompressed ($M > 1$) by a system of shocks, the barrel shock at the sides and the Mach disk shock normal to the centerline. The mach disk location can be found with the formula $(x_M/D) = 0.67(P_0/P_b)^{0.5}$. The region called "zone of silence" represents an area of isentropic expansion and was used for our experiments. The skimmer (Beam Dynamics, 1 mm orifice diameter) was places in this region to extract the cold centerline beam. Estimated length of the "zone of silence" for our experimental conditions (D=1 mm, P_0=1 bar, P_b=10^{-7} bar) was 212 cm. The skimmer was placed several cm from the nozzle. By dividing the vacuum chamber (fig. 2.1) into two parts, we introduced a secondary supersonic [8] expansion region (not shown in fig. 2.2) behind the skimmer. The secondary expansion helped to minimize collisions introduced by sharp edges of the skimmer. Ionization of the molecular beam with the laser took place in the secondary expansion region.

2.1.2 Molecular beam experiments with non-volatile biomolecules

Free-jet expansion of atomic and molecular beams was introduced many decades ago and was successfully used to study atoms and small gaseous and volatile molecules [9]. To carry out such kind of experiments with big non-volatile, temperature sensitive biological molecules (e. g. DNA bases), it is necessary to solve several technical problems. To increase the volatility of the molecules we used thermal evaporation. However, a heating to high temperatures ($200 - 220\,^{\circ}\mathrm{C}$) can cause partial decomposition of the sample and therefore contamination of the oven and the valve. The former leads to blocking of the sample lines, and the latter to unstable valve operation. Additionally, all elements of the setup in contact with the sample, should be heated homogeneously to avoid large temperature gradients. It is also desirable to do the heating as fast as possible and in controlled manner.

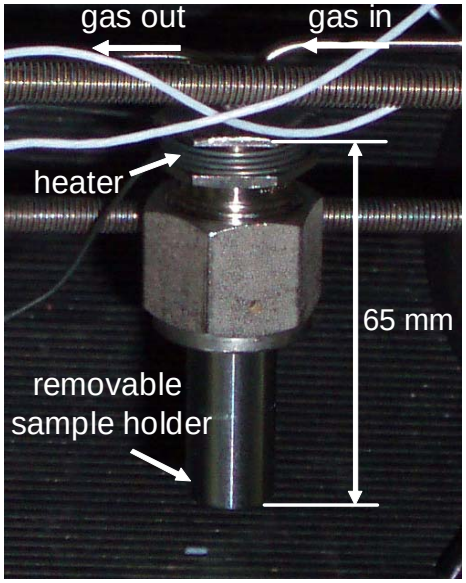

Figure 2.3: A photograph of the sample oven, developed for optimization of experiments with DNA bases in the gas phase.

A molecular source was built to fulfill these requirements. First of all, an oven was constructed (fig. 2.3). Because of its small size and a "smart design" we could easily access the sample and clean the oven. The heating wire was placed only at the oven top and provided equal heating for the whole oven without big temperature gradients. The removable sample holder could be easily disconnected from the heated head and cleaned from contamination. We tried to minimize the latter by placing

a glass wool in the gas outlet tube. The glass wool filtered gaseous molecules from decomposed ones (soot). The heating time of the oven from a room temperature to $200 - 220\,^{\circ}\mathrm{C}$ was $\sim$20 min. The temperature of the oven was kept stable with the accuracy of $\pm 1\,^{\circ}\mathrm{C}$ by the temperature controllers (Omron, E5GN).

Secondly, the pulse valve should also be heated and therefore was modified. A standard "General valve", series 9 nozzle is made to operate at temperatures up to $125\,^{\circ}\mathrm{C}$ for short heating [10]. Therefore, the coil wire of such a nozzle was replaced with a capton-isolated wire (Allectra, d = 0.025 mm), which could be heated up to $300\,^{\circ}\mathrm{C}$. After this modification, the nozzle was always heated to temperatures $5 - 10\,^{\circ}\mathrm{C}$ higher than the oven to avoid condensation of molecules on the cooler surface of the nozzle and to prevent clogging of the nozzle.

Thirdly, we minimized the length of the connecting metal tube between the oven and the valve to decrease the temperature gradient in the tube. This prevented the condensation of the molecules on the tube walls. During the experiments the temperature of the oven, valve and the connecting tube was constantly measured.

Fourthly, heating of the skimmer was also necessary to prevent clogging of its small orifice (1 mm). Two small halogen lamps were used to heat the skimmer from the top and the bottom. The skimmer except of its sharp tip was covered with a thin layer of graphite to make the heating more efficient. Without heating the skimmer clogging took place within a few hours of pulsed operation. Cleaning of the skimmer was always conjugated with breaking of the vacuum and a readjusting the molecular source (oven and valve) position, which is a very time consuming endeavor and should be avoided.

2.1.3 Cluster formation

Clusters of DNA bases and 2-AP molecules were formed in the supersonic-jet expansion. Molecules in the molecular beam are characterized by low temperatures (few to tens of K), and cluster formation may happen via three-body collision in the cold zone of the expansion. Several experimental parameters were adjusted to control clustering efficiency: the temperature of the oven, the pressure of the carrier gases, and the time delay between nozzle opening and the laser pulse. The latter allowed to select zones of different temperature and density in the pulsed molecular beam. The beginning of the gas pulse from the nozzle is characterized by a high temperature and clustering is poor. In the end of a gas pulse, molecules are cold, but clustering is

weak due to the low density of molecules [8, 9]. The optimal conditions for clustering were found in the middle of the gas pulse, where the temperature is low enough for clustering and the density of molecules is still high. Additionally, a small angle cone was attached to the nozzle to increase the number of collisions for better clustering.

For experiments with water clusters, the carrier gases were seeded with water vapor at room temperature. A U-shaped glass reservoir with distilled water was attached to the sample line outside the vacuum chamber. The carrier gas was flowing over or bubbled through the reservoir to pick up water molecules and carry them through the heated sample to the pulsed valve.

2.2 Time-of-flight mass spectroscopy

For the mass-selective investigation of molecules and clusters we used time-of-flight (TOF) mass spectroscopy. Key to this method is the acceleration of ions with an electric field. Ions with different masses will acquire different velocities and therefore will arrive at different times at the detector. By converting the measured arrival times into masses, one can identify the mass of the detected species. One problem that arose in the early days of TOF mass spectroscopy was the disability to distinguish molecules which have identical masses but slightly different TOFs due to different starting positions. Even small differences in arrival times at the detector will cause broadening of the corresponding mass peaks. This is due to the fact that ions, formed in different spacial positions, pick up different amounts of energy in the electric field and will have different velocities. A solution to overcome this broadening of mass signals and achieve better resolution was offered by Wiley and McLaren in the 1955. They suggested the use of two electric fields for ion acceleration [11] as it shown in fig. 2.4.

The second field E_d helps to correct TOFs of ions with identical masses (I_1 and I_2) if they had different starting positions. After passing the zone d, ions with different velocities and different time-of-flights picked-up additional energy to arrive at the detector at the same time. The TOFs of the ions will be independent of the starting position and depend only on their mass.

The total energy of the particle at the end of the drift tube is [11]

$$U = U_0 + U_s + U_d + U_D = U_0 + qsE_s + qdE_d, \tag{2.1}$$

where U_0 is the initial kinetic energy of the particle, U_s, U_d and U_D are the energies in

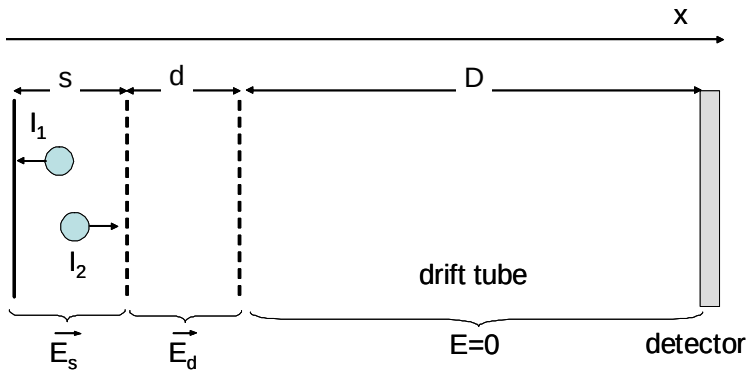

Figure 2.4: Wiley-McLaren type mass spectrometer. Ions (I_1 and I_2) are accelerated in the repeller region s and accelerator region d by the fields E_s and E_d and fly in a field-free region D in the drift tube towards the detector.

the zone s, d and the drift tube, and q is the electron charge. The total time-of-flight of the particle is

$$T_{all} = T_s + T_d + T_D. \tag{2.2}$$

The time-of-flight for the zone s can be found as (see also [11])

$$T_s = \frac{\sqrt{2m}}{qE_s}\Big(\sqrt{U_0 + qE_s s} - \sqrt{U_0}\Big). \tag{2.3}$$

To find the time-of-flight in the zone d one should redefine U_0 using Eq. (2.1) as

$$U_0^d = U - qdE_d. \tag{2.4}$$

Then we obtain

$$T_d = \frac{\sqrt{2m}}{qE_d}\Big(\sqrt{U} - \sqrt{U_0 + qE_s s}\Big). \tag{2.5}$$

And the time-of-flight in the drift tube in the absence of a field will be

$$T_d = \frac{\sqrt{2m}D}{2\sqrt{U}}. \tag{2.6}$$

The necessary condition for space focusing (ions of any given mass arrive at the detector at the same time independent of the starting position) in the double-field mass-spectrometer is

$$\left.\frac{dT_{all}}{ds}\right|_{s_0} = 0 \tag{2.7}$$

where s_0 is the starting position. If this condition is fulfilled then the final time-of-flights of ions are independent of their starting positions and depend only on the ratio between the accelerating voltages $E_s s/E_d d$. The mass spectrometer used in this work was built on this principle. With s=10 mm, d=50 mm, D=500 mm, and $(E_s s + E_d d)_{max}$ = 2000 V one can find a ratio $E_s s/E_d d$, ~1/10. Optimization of the mass resolution in the experiments was done by adjusting this ratio with a variable resistor R_2 (Fig. 2.5). The resistors R_3-R_5 introduced a smooth electric field in the accelerator zone. Additionally, we used weak electric fields along the X- and Y-axes to guide the ions into the detector. A focusing of the ion beam onto the detector was achieved by an ion Einzel lens. It consisted of a cylindrical positive electrode located between two neutral electrodes on the sides.

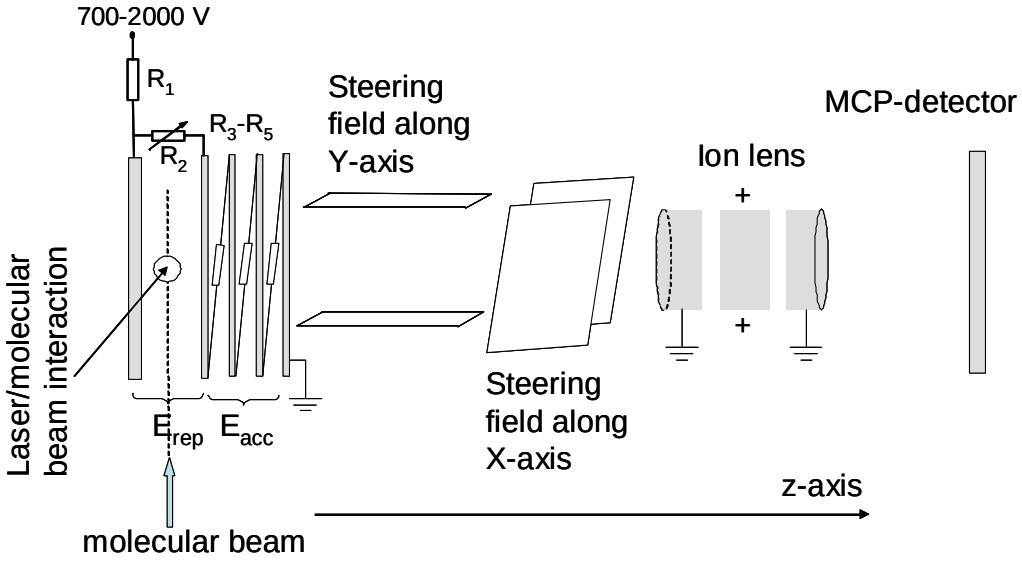

Figure 2.5: Schematic of the experimental mass-spectrometer. To guide the ions to the detector, pulsed high voltage up to 2 kV was used. The resistor R_2 is variable between 0 and 1 kΩ to adjust the ratio between the accelerator voltage and the repeller voltage. The resistances R_3-R_5 are 50 kOm and were used to decrease the electric field in the accelerator zone homogenously. The steering fields and the ion lens guided the molecular beam into the detector.

An important modification was done to the TOF mass spectrometer in this thesis. In the original configuration [12], ions were detected either by a simple mass spectrometer or by an electron-ion coincidence spectrometer. In the first case, ions were extracted and detected parallel to the molecular beam axis. In the second case, ions were extracted perpendicular to the beam, but then deflected onto the ion detector

with an ion mirror. In a new configuration used in this thesis, only the ion detector accommodated in the coincidence spectrometer was used and ion extraction and detection was always perpendicular to the molecular beam. This significantly increased the mass resolution and helped to detect ions over a great m/z range which could not be simultaneously focused onto the ion detector before. The mass resolution of the spectrometer is determined by the initial velocity distribution of ions. In the molecular beam, this distribution is larger in the flow direction of the beam than perpendicular to it. Therefore, perpendicular extraction/detection scheme resulted into better mass resolution even with a slightly shorter TOF tube (see fig. 2.6). The resolution of the mass spectrometer with parallel ion extraction was $M/\Delta M \simeq 250$. It is increased for the case of the perpendicular extraction to $\simeq 500$.

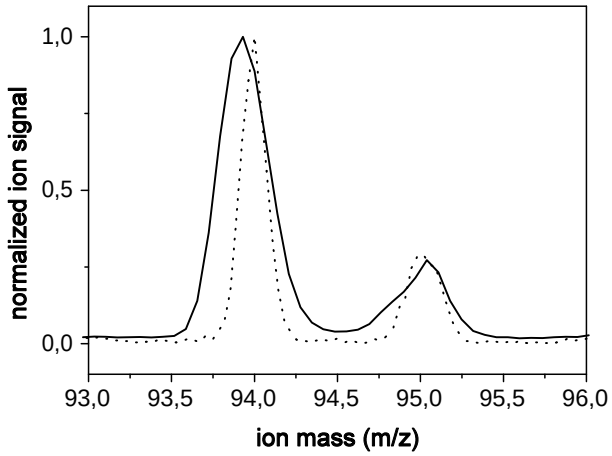

Figure 2.6: Mass spectra of 2-AP (m/z=94) for ion extraction parallel (solid line) and perpendicular (dashed line) to the molecular beam. The spectra illustrate the increased mass resolution for perpendicular ion extraction as discussed in the text. The small peaks at m/z = 95 correspond to the isotopic peaks due to the natural abundance of ^{13}C and ^{2}D. The mass spectra were measured with a sampling resolution of 10 ns (solid line) and 1 ns (dashed line).

2.3 Time-of-flight electron spectroscopy

2.3.1 The "magnetic bottle" electron spectrometer

Electrons were also detected with a time-of-flight spectrometer, the scheme of which is presented in fig. 2.7.

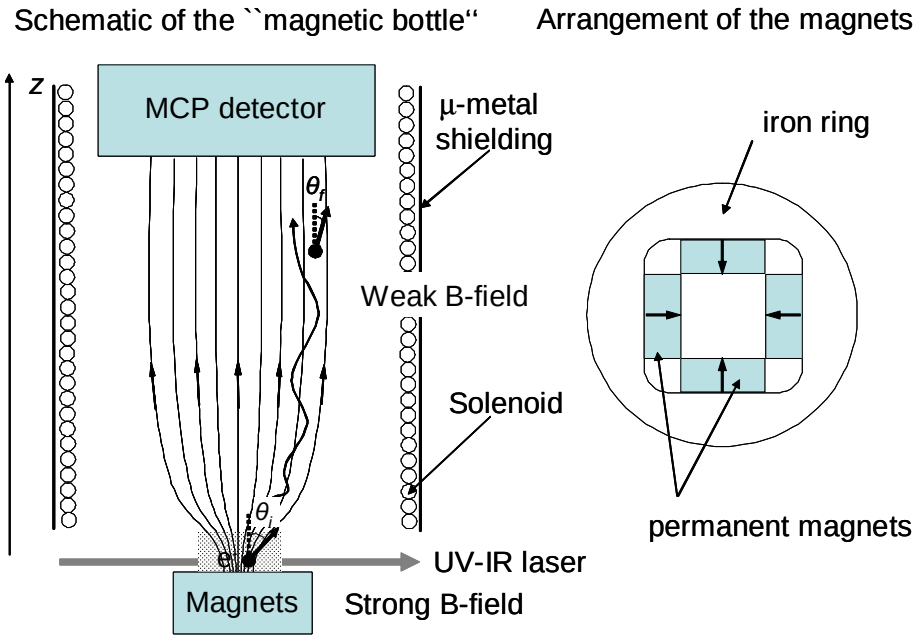

Figure 2.7: The magnetic bottle electron spectrometer (a) and the arrangement of magnets to generate a turning magnetic field (b). Electrons with big initial angles θ_i are parallelized in the magnetic field ($\theta_f << \theta_i$), and can be collected at the end of a flight tube.

Due to their kinetic energy after ionization the electrons flying along the z-axis of the spectrometer can reach the detector. In order to collect electrons emitted in a wide range of initial angles, $0 < \theta < 90\,^\circ$ (see fig. 2.7), a "magnetic bottle" spectrometer was used. The spectrometer is based on a strongly inhomogeneous magnetic field created by permanent magnets and a solenoid. Electrons emitted at an angle to the field lines in the strong-field region are turned by the field towards the detector. In the region of small z, the Lorenz force causes the electrons to spiral around a magnetic field line and they follow this field line into a region of weak and uniform field in which the field lines are again parallel. In going from the strong-field to the weak-field regions, the Lorentz force has a component along the path of the guiding

center of the electron motion. This causes the longitudinal velocity component to increase, and since the total velocity is constant the transverse component decreases giving the effect of parallelization and unspiralling. Even electrons that are initially emitted nearly perpendicularly to the fields lines in the strong-field region finish by being nearly parallel to the field lines in the weak-field region, if the field strengths in the two regions are sufficiently different. According to [13], the initial angular momentum of the electron is given by

$$l_i = \frac{m^2 v^2 sin^2\theta_i}{eB_i} \tag{2.8}$$

where m, v and e are the mass, velocity, and charge of the electron, θ_i is the initial angle of the velocity with respect to the time-of-flight axis, and B_i is the initial, strong magnetic field. From conservation of angular momentum, the final velocity angle of the electron, θ_f, in the lower magnetic field, B_f , is given by the relation:

$$\frac{sin\theta_f}{sin\theta_i} = \left(\frac{B_f}{B_i}\right)^{\frac{1}{2}} \tag{2.9}$$

If the ratio of the final and initial fields is large, then the final electron velocity vector will be nearly parallel to the TOF axis for a large range of initial angles. For the electron spectrometer, used in this work, B_i was 100-150 mT and B_f was 0.3 mT [12]. For the maximum initial angle near $\theta_i = 90°$, the final angle is $\theta_f = \arcsin(B_f/B_i)^{0.5} = 2.56°$. The spectrometer resolution is limited by the different lengths of the electron trajectories (in our case $\leq$50 meV). It is therefore important to have a large ratio of the final and initial fields so that electrons are turned around fast and have similar length of their trajectories in the TOF tube. Also, for the best energy resolution, it is important that the initial field gradient is as large as possible while remaining in the adiabatic limit, otherwise the Eq. (2.8) and Eq. (2.9) can not be used. The adiabaticity parameter is defined by

$$\chi = \frac{2\pi mv}{eB_z^2}\left|\frac{dB_z}{dz}\right|, \tag{2.10}$$

which is the fractional change in the field that the electron experiences in one cyclotron orbit. If χ is less than 1, then adiabatic conditions are fulfilled. That means that the change in the field acting on an electron during one orbit is negligible as compared to the total field and the electron will process around one field line in the z-direction. For the spectrometer used in this work, we applied a magnetic field strength of 110 mT over a 5 mm distance of the ionization region. According to Eq. (2.10), the

adiabaticity parameter was estimated to be 0.066, and it changes along the TOF length, because of the different fractional change of the magnetic field. To avoid distortion of the applied magnetic field by the earth magnetic field, the electron spectrometer was shielded by a μ-metal cylindrical hose. To increase the collection efficiency for low-energy electrons, which can be affected by a contact potential, an additional small battery voltage (0.2-1 V) was used to accelerate slow electrons to the detector.

2.3.2 Calibration of the electron spectrometer

Prior to electron spectroscopy experiments on molecules of interest, the electron spectrometer was calibrated to properly convert measured time-of-flight values into energy. Nitric oxide (NO) was used for calibration.

Ionization of NO. Nitric oxide is a linear diatomic molecule with well separated energy levels as shown in fig. 2.8 [14]. It was chosen as a calibration compound because its ionization energies are in the same energy range as the ones of our samples, and the vibrational structure of NO can be resolved well.

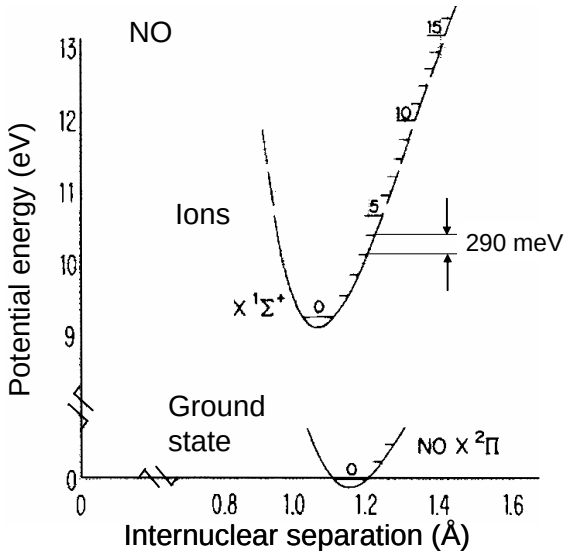

Figure 2.8: Calculated potential energy surfaces of NO for the ground and the ionic states (adapted from ref. [14]).

For calibration, NO was ionized in multiphoton one-color (pump or probe only) or two-color (pump-probe) experiments. The available laser photon energies in the

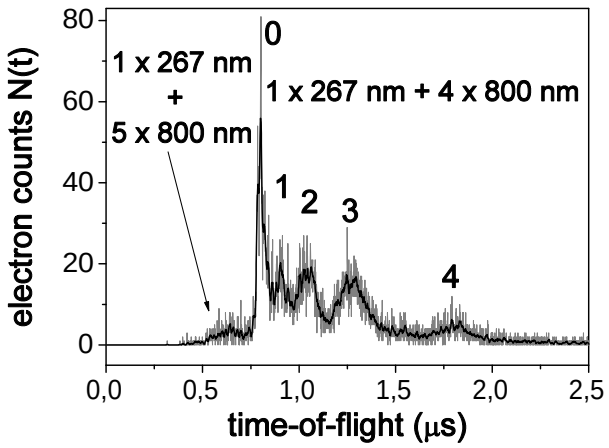

Figure 2.9: Electron spectrum of NO plotted as a function of the TOF. The gray line depicts the experimentally measured data points, the black line is the same curve with 10 pts smoothing to guide the eye. Peak positions 0...4 can be assigned to the ionization potentials of vibronic states in the cation as given in table 2.1. The signal below 0.75 μs is due to absorption of one extra probe photon.

range 9 - 11 eV allowed to observe several vibrational bands in the calibration spectra. A typical time-of-flight spectrum of NO is shown in fig. 2.9. The time axis of the spectrum was converted into an energy axis. If the electron would fly completely field-free, its kinetic energy at the detector would be

$$E_{kin} = \left(\frac{mx^2}{2}\right)\frac{1}{t^2} \tag{2.11}$$

where m, x, and t are the electron mass, the length and the time of flight of the electrons. Hence, we parametrize Eq. (2.11) appropriately taking $(mx^2/2)$ as an instrument constant (IC), allowing for starting time $t_0 \neq 0$ and a starting potential U_0 for the electrons which may also be $\neq 0$. Second, the arrival times of electrons and their kinetic energies should be corrected by the uncertainty of start time t_0 and energy E_0. Thus we write Eq. (2.11) as

$$E_{kin} + eU_0 = \frac{IC}{(t - t_0)^2}. \tag{2.12}$$

The spectrum shown in fig. 2.9 has five distinct bands. The arrival times t for the bands 0...4 were estimated from the band maxima in the spectrum. These times were assigned to the expected electron kinetic energies, which can be calculated with the

formula

$$E_n^{kin} = E_{laser} - IP_n, \tag{2.13}$$

where E_{laser} is the total photon (laser) energy, and IP_n are the known ionization potentials. The total photon energy can be found from Eq. (2.14)

$$E_{laser} = \sum h\nu_{pu} + \sum h\nu_{pr}. \tag{2.14}$$

For the spectrum shown in the fig. 2.9 E_{laser} is 10.85 eV, assuming excitation with one photon of 267 nm (4.65 eV) and ionization with 4 photons of 800 nm (4×1.55 eV). The ionization potentials IP_n for NO were taken from literature [15]. The table 2.1 shows the literature ionization potentials, the expected kinetic energies of electrons and the measured arrival times taken from fig. 2.9. Substituting the values from the table in Eq. (2.12), calibration constants IC, t_0, and eU_0 were calculated, and the time axis was converted into energy axis.

Table 2.1: Ionization potentials [15], expected and observed kinetic energies for a 1×267 nm + 4×800 nm ionization process and the observed arrivals times of electrons.

n	IP_n, eV [15]	E_k^{exp}, eV	E_k^{obs}, eV (from fig. 2.10)	t, μs (from fig. 2.9)
0	9.264	1.586	1.651	0.800
1	9.554	1.296	1.377	0.904
2	9.841	1.009	1.124	1.042
3	10.123	0.727	0.819	1.272
4	10.402	0.448	0.472	1.815

It is also necessary to correct the spectral amplitudes (Jacobian correction) so that the number of electrons plotted as a function of energy $N(E)$ should be equivalent to the number of electrons detected in the corresponding time window $N(t)$. The signal integrals must be maintained and $N(t)dt = N(E)dE$. $N(E)$ can be found as

$$N(E) = \frac{N(t)dt}{dE}, \tag{2.15}$$

where $N(t)$ is the measured signal, and dE/dt can be evaluated using Eq. (2.12):

$$\frac{dE}{dt} = -\Big(\frac{2IC}{(t-t_0)^3}\Big). \tag{2.16}$$

With substitution $(t-t_0)$ from Eq. (2.12) into Eq. (2.16) we obtain from Eq. (2.15) a correction factor for the number of electron counts as a function of energy

$$N(E) = -\frac{1}{2}N(t)\frac{(IC)^{\frac{1}{2}}}{(E-eU_0)^{\frac{3}{2}}}. \tag{2.17}$$

Using the formulas of Eq. (2.12) and Eq. (2.17) one can convert the arrival times of electrons into the kinetic energies and correct the spectral amplitudes. For the electron spectrum of NO in fig. 2.9, the calibrated spectrum is shown in fig. 2.10.

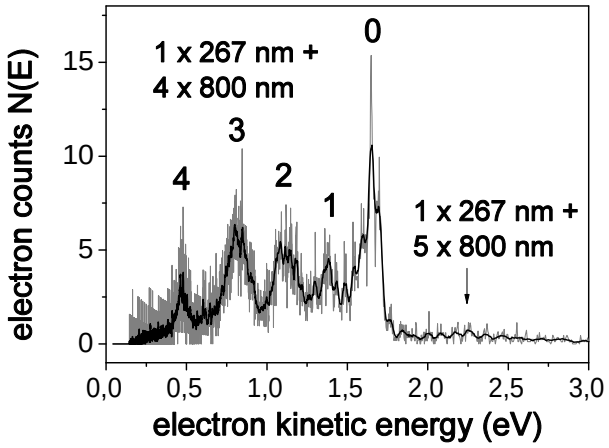

Figure 2.10: Calibrated electron spectrum of NO as a function of the kinetic energy, intensity scaled according to Eq. (2.17). The spacing between the peaks is in agreement with the literature value of 290 meV [15].

The signal-to-noise ratio of the electron spectra varied for different measurements. Therefore, the error of calibration also changed usually between 30 and 100 meV.

2.4 Coincidence measurements

Electron spectroscopy yields information about the electronic structure of one molecular species at a time. If more than one species is present in the molecular beam, e.

g. clusters, different molecules, their electron spectra would not be distinguishable. To distinguish electron spectra from different species in the molecular beam, we used femtosecond electron-ion coincidence (FEICO) technique which was first introduced by the group Radloff and Hertel [16]. To to correlate the measured electrons to the measured ions the number of detected electrons and ions should be drastically decreased and the average number $\bar{n}$ of ionization events per laser shot should be $\ll 1$. If the experimental conditions are stable, then the probability to produce n electron-ion pairs is described by a Poisson distribution

$$p(n) = \frac{\bar{n}^n}{n!} \exp(-\bar{n}). \tag{2.18}$$

If a single detected ion and a single detected electron are due to ionization of a single molecule/cluster, then such an event is a "true" coincidence. It also possible that one ion and one electron arrive at the detector from two different ionization events and this is considered as a "false" (non-correlated) coincidence. The distribution for true and false coincidences as a function of $\bar{n}$ are presented in fig. 2.11 [17]. The maximum probability for true coincidences is reached at $\bar{n} \sim 1.5$. At this point, the number of false coincidences is very large. In order to minimize the latter, it is necessary to keep the coincidence rate much lower. In our experiments, the coincidence rate was kept below 10 % and the number of false coincidences did not exceed 10% of the total number of coincidences.

Such low coincidence rates and the necessity to subtract one-color pump only and probe only ionization signals lead to very time consuming measurements to obtain reasonable signal amplitudes to interpret the spectra. For example, to collect 1000 counts in a cluster mass channel, which is only 5% of the total signal with a repetition rate of 100 Hz, detector efficiencies of 40% (electrons) and 35% (ions), an ionization rate of 10%, and assuming that a pump-probe signal is only ∼30% of the total signal in this mass, then the estimated measurement time is

$$T = \frac{1000}{100 \times 0.1 \times 0.05 \times 0.4 \times 0.35 \times 0.3} \simeq 12h. \tag{2.19}$$

2.5 Femtosecond laser systems

Time-resolved characterization of short-lived excited states in molecules and clusters requires the use of short-pulse light sources for excitation and ionization. Nowadays, commercial laser systems based on a Ti:Sa (titanium sapphire, Ti:Al_2O_3) crystal

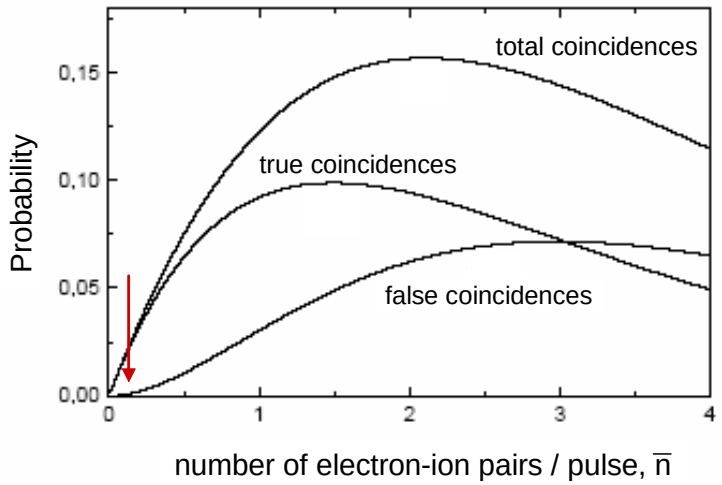

Figure 2.11: True, false, and total coincidences as a function of a number of electron-ion pairs per laser pulse (reproduced with permission from ref. [17]). The arrow indicates the experimental coincidence rate of 0.1.

provide short (τ<50 fs) and intense laser light pulses. This is achieved with mode-locking and a chirped-pulse amplification (CPA) methods, the principles of which are shortly described below.

Generation of ultrashort laser pulses. The output of a Ti:Sa laser operating in the CW regime consists of an almost random sequence of light pulses, corresponding to the superposition of many longitudinal modes. In the mode locking regime, however, these modes form short and intense laser pulses. Assuming that $2n+1$ longitudinal modes are oscillating with the same amplitude E_0, and the phases φ_l of the modes are locked with

$$\varphi_l - \varphi_{l-1} = \varphi = const, \tag{2.20}$$

then the total electric field at any given point is described with the formula

$$E(t) = \sum_n E_0 exp\Big(i[(\omega_0 + l\Delta\omega)t + l\varphi]\Big), \tag{2.21}$$

where ω_0 is the frequency of the central mode, $\Delta\omega$ is the frequency difference between two consecutive modes, and the value of the phase for the central mode is, for simplicity, zero. The amplitude of the pulses can be found as

$$A(t) = E_0 \frac{sin[(2n+1)\Delta\omega)t/2]}{sin(\Delta\omega t/2)}, \tag{2.22}$$

The pulse duration for each generated pulse will be [18]

$$\tau_p \cong \frac{2\pi}{(2n+1)\Delta\omega} = \frac{1}{\Delta\nu_L}, \tag{2.23}$$

where $\Delta\nu_L = (2n+1)\Delta\omega/2\pi$ is the total laser bandwidth. From Eq. (2.23), one can see that the duration of each pulse is roughly equal to the inverse of the oscillating bandwidth. In a realistic laser not all modes have equal amplitudes and the spectral envelope is assumed to have a Gaussian shape. If the mode locking condition holds (Eq. (2.20)), then the field amplitude will be given by the Fourier transform of the spectral amplitude. The pulse duration, in a general case, is then expressed as $\tau_p = \beta/\Delta\nu_L$, where β is a numerical factor that depends on the particular shape of the spectral intensity distribution. A pulse of this sort is so called *transform-limited*. If the mode locking condition (Eq. (2.20)) is not fulfilled, the output pulse may be far from being transform-limited. The carrier frequency then becomes time-dependent, and the pulse has *a chirp*.

The average energy per pulse of a mode locked Ti:Sa oscillator is usually in the nJ range. For gas phase ionization experiments this is not sufficient. Further amplification is achieved with the CPA method. The output pulse from the fs oscillator is first stretched to picosecond pulse durations. It then passes through an amplifier cavity where the pulse is amplified to an energy in the μJ or mJ range. After amplification, the pulse is re-compressed to the original fs pulse duration.

Amplified commercial Ti:Sa laser systems were used in the application laboratories at the MBI. The laser systems were chosen according to the excitation wavelengths required. DNA bases have a good absorbance in the wavelength range of 260-270 nm, and could be excited with a third harmonic (267 nm) of a Clark laser system with a corresponding nonlinear frequency conversion setup. The Multicolor laser system provided tunable wavelength output and was used for experiments with the model system (2-AP) in the wavelengths range between 250 nm and 296 nm. The characteristics of both laser systems are given below.

Clark system. The Clark laser system (fig. 2.12) is based on a commercial Ti:Sa oscillator (Clark, MXR) pumped by a diode laser. The oscillator produces nJ pulses with 1 MHz repetition rate. The laser pulses are amplified with a regenerative amplifier (Clark, TRA-1000), pumped with a Q-switched frequency-doubled Nd:YAG laser at the wavelength of $\lambda = 532$ nm (Clark, ORC-1000).

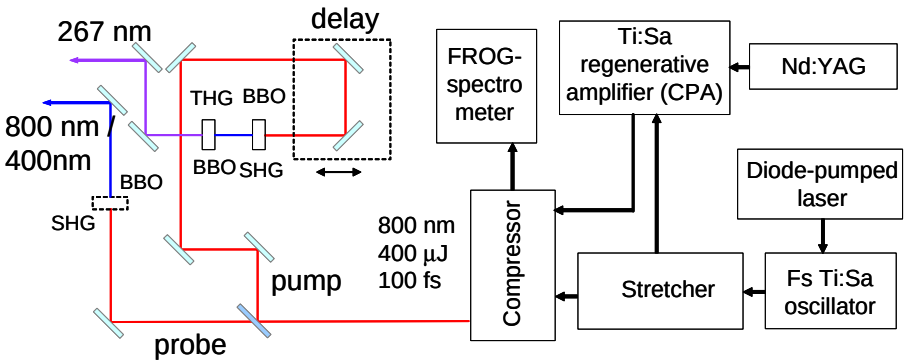

Figure 2.12: Schematic representation of the Clark laser system.

After amplification, pulses at 800 nm with 1 kHz repetition rate are compressed to ∼100 fs with a pulse energy of 400 μJ. For pulse characterization, a commercial FROG-spectrometer was used. For the pump-probe experiments, the output of the laser was split into two beams of equal intensity. One beam was nonlinearly converted with a BBO (β-barium borate, $\theta = 29.2\,°$, 0.7 mm) crystal into 400 nm by second harmonic generation (SHG). The third harmonic, 267 nm was obtained by frequency mixing in a BBO crystal ($\theta = 29.2\,°$, 0.7 mm) of 800 nm and 400 nm. The obtained UV pulse was delayed in time and used as pump pulse for excitation of the molecules. The second beam was used to probe the molecules by ionization. For the probe pulse, the fundamental frequency of 800 nm or its second harmonic of 400 nm (BBO, $\theta = 55.5\,°$, 0.3 mm) were used.

Multicolor system. The Multicolor laser system (fig. 2.13) gave us the opportunity to tune the excitation wavelength. The commercial femtosecond Ti:Sa oscillator (TSUNAMI, Spectra Physics) generates 80 MHz, 50 fs pulses with a wavelength of 800 nm. The pulses are then amplified with a regenerative amplifier (SPITFIRE, Spectra Physics) to 2 mJ at 700 Hz. The amplified output laser pulses pass through the TOPAS (Travelling-Wave Optical Parametric Amplifier of Superfluorescence, Light Conversion, model 4/800/f), where the fundamental wavelength at 800 nm is converted into the near IR. The resulting beam is frequency doubled with a non-linear crystal into the visible light, and then into the UV light (BBO, $\theta = 65\,°$, 0.1 mm). For pump-probe experiments, the pump pulse wavelength was varied between 250 nm and 296 nm. The wavelength of the delayed probe pulse was 800 nm or 400 nm.

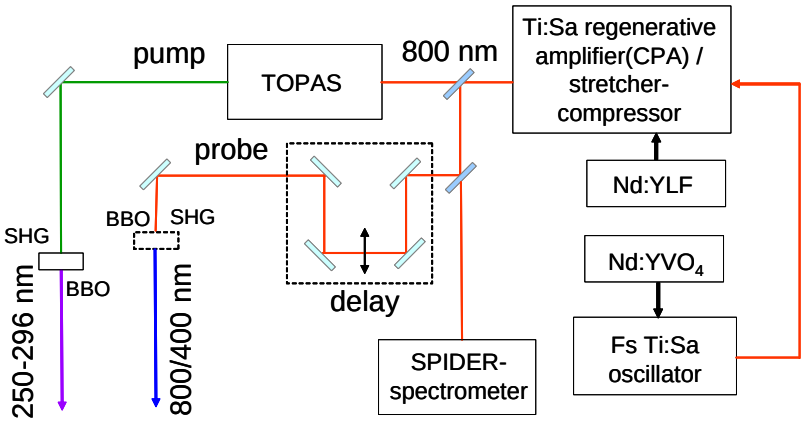

Figure 2.13: Schematic representation of the Multicolor laser system.

Pump-probe experiments. A schematic of the pump-probe optical setup with collinear overlap between the pump and the probe pulses is shown in fig. 2.14.

In the original setup [12] a lens was used for focusing of the two pulses into the chamber. In later experiments the lens was replaced with a focusing mirror M6 (Al, R=750 mm). This replacement allowed us to fulfill a necessary requirement for pump-probe experiments that the beam diameters should be similar. The refractive index in a lens is wavelength dependent, what leads to different focusing positions for the pump and the probe beams. This means that at interaction with the molecules, the laser beam diameters will be different. Focusing with a mirror solved this problem, and both laser beams could be focused in the same position. In the new setup, the angle α (see fig. 2.14) was kept small to reduce optical abberations due to astigmatism. The replacement of the lens with a mirror resulted in better pump-probe contrast and much easier alignment of the laser beams. The focusing mirror M6 was placed on a one-dimensional translation stage to adjust the focus position depending on the beam sizes. The latter changed for every experiment due to many laser users in the application labs at MBI. To further increase the pump-probe contrast in the experiments, a fine adjustment of the overlap between the pump and the probe beams was necessary. The beams were first roughly overlapped through a hole in a razor blade. Then the fine adjustment was done by alignment of the probe beam relative to the pump beam with a motorized mount (Standa, 8MMA60-1) for the mirror M3.

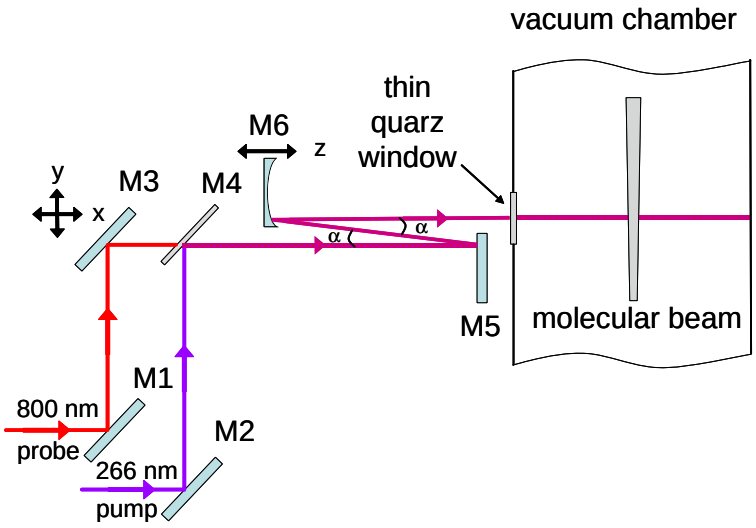

Figure 2.14: Collinear pump-probe optical setup with a focusing mirror. $M1$, $M2$, $M3$, $M4$ are dichroic mirrors, $M5$ is a plane Al mirror, $M6$ is a focusing Al mirror. Mirror $M3$ is mounted on a two-dimensional motorized holder for fine adjustment of the pump-probe overlap. Mirror $M6$ is mounted on a translation stage for focus size adjustment.

2.6 Data acquisition

Most **time-resolved measurements** were carried out detecting only ion signals. The master trigger for the experiments (fig. 2.15) was the fs laser (pump or probe), which was monitored by a photodiode (PD). A pulse divider reduced the 1kHz/700 Hz repetition rate of the laser to 100-200 Hz repetition rate of the pulsed valve. After a time delay 1, the pulsed nozzle was opened. The opening of the nozzle was synchronized with the next laser pulse. The next laser pulse (delay 2) activated the high-voltage (HV) Behlke-switch of the mass-spectrometer. The ions created by ionization of the pulsed molecular beam were accelerated by the HV field towards the MCP detector. The signal from the detector was amplified and discriminated (Novelec, AD100B) and then read out with a data acquisition cards (Fast ComTech, P7888) with a sampling rate of 1GHz or 100 MHz (Becker-Hickl, ADA-100). The data were then evaluated with LabView (National Instruments, version 4.0 and 6.0) programs. The measured mass spectra at each time delay were stored. The integrated intensities for each mass peak were plotted as a function of time delay. The time-dependent curves obtained were fitted with the convolution

$$s(t) = g(t) \otimes f(t), \tag{2.24}$$

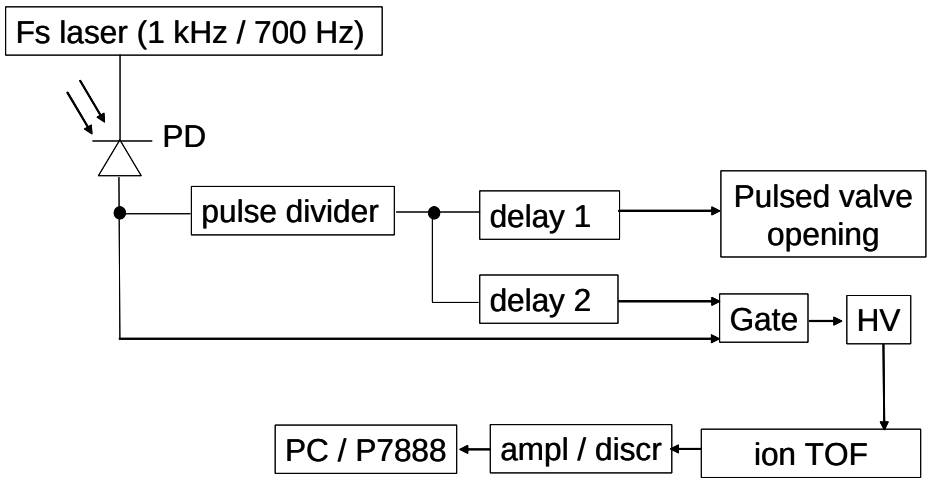

Figure 2.15: Block-scheme of ion signal acquisition.

where $s(t)$ is the fit curve, $g(t)$ is a Gaussian pulse characterizing the cross-correlation function of the two laser pulses, and $f(t)$ is the decay function, consisting of one or several exponentials. To fit parallel decay channels

$$f(t) = \delta(t) + \sum_n A_n exp\Big(-\frac{t}{\tau_n^d}\Big) \tag{2.25}$$

was used, where $\delta(t)$ was introduced to fit non-resonant contribution of the dynamics (not always used), A_n are the corresponding amplitudes of the decay components, τ_n^d are the life times of the decay components (excited states). For several subsequent decay channels (no more than 2 for our data)

$$f(t) = \delta(t) + \Big[A_1 exp\Big(-\frac{t}{\tau_1^d}\Big) + A_2\Big(1 - exp\Big(-\frac{t}{\tau_1^r}\Big)exp\Big(-\frac{t}{\tau_2^d}\Big)\Big)\Big], \tag{2.26}$$

was used, where τ_1^d is a decay time of a first transient. The second transient is described by a decay time τ_2^d and a rise time τ_1^r ($\tau_1^r \sim \tau_1^d$). Our experimental data often were fitted by a combination of Eq. (2.25) and Eq. (2.26).

For **the coincidence measurements**, data acquisition and evaluation was more complex (fig. 2.16). The electrons were collected after photoionization with a "magnetic bottle" electron spectrometer. The ions were extracted with a pulsed electric field after a delay 2 (∼300 ns) with respect to the electrons. The signals from the electron and ion MCP detectors were read out by a 8-channel time-to-digital converter (TDC) (LeCroy, 4208). Each channel of the TDC could store only one ion or electron count and the TDC was used in a configuration to detect up to 4 electron

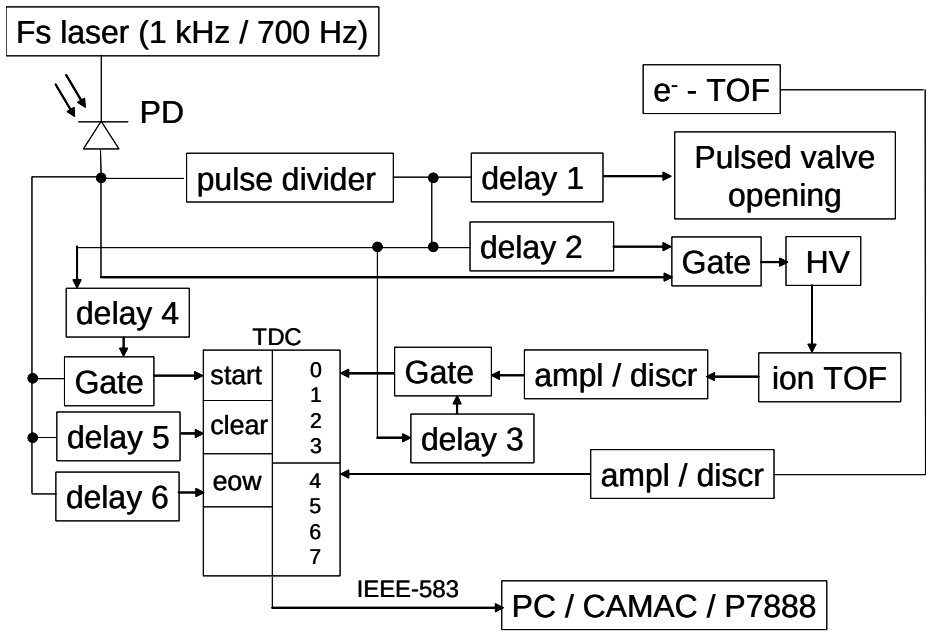

Figure 2.16: Block-scheme of electron-ion coincidence signal acquisition.

and 4 ion counts. A coincidence corresponded to the case when one ion channel and one electron channel registered a count. The trigger for the TDC ("start") was the gated signal from the PD. Before a new measurement started, the previous data were removed with the signal "clear". The measurement time window was controlled by the signal "end of window" (eow) and was usually set to 100 μs. The communication between the TDC and the measurement computer took place via a CAMAC-controller (Granville-Phillips, 6001) and the corresponding input/output interface (IEEE-583). The data were evaluated with LabView programs. An example of a coincidence spectrum is given in fig. 2.17a. Each point in the spectrum is due to one coincidence event. By accumulating enough data points one can obtain a coincidence electron spectrum for many masses simultaneously. E. g., such a spectrum for 2-aminopyridine monomer ($(2\text{-AP})_1$) before and after calibration is shown in fig. 2.17b, and c, respectively.

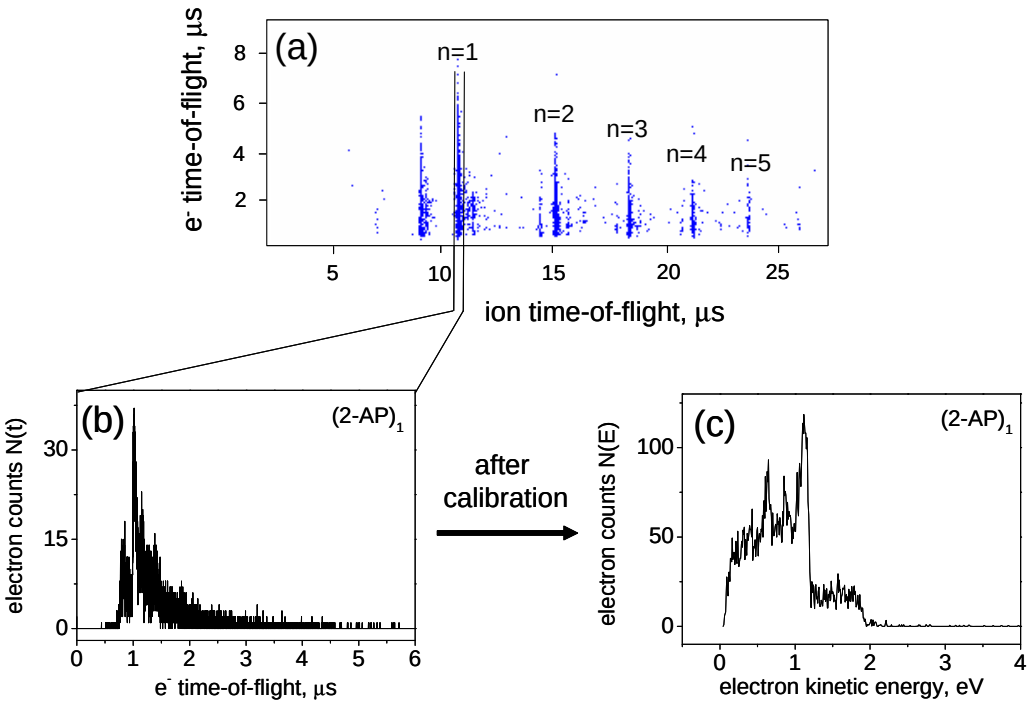

Figure 2.17: Electron-ion-coincidence spectrum of $(2\text{-AP})_n$, n=0...5 (a), and evaluated electron spectrum of $(2\text{-AP})_1$ before (b) and after (c) calibration. Each dot in (a) corresponds to one coincidence.

Chapter 3

The model system 2-aminopyridine

3.1 H-transfer reaction in 2-AP dimer: literature overview

Hydrogen-bound 2-aminopyridine (2-AP) dimer was chosen as a mimic of Watson-Crick (WC) DNA base pairs because of the similarity in their structures (see fig. 3.1). High-level *ab initio* calculations [7] predicted a fast proton-coupled electron transfer (PCET) reaction along an intermolecular H-bond in 2-AP dimer. The same reaction was predicted to play an important role in DNA base pairs and might be a key mechanism to increase the photostability by offering a very efficient coupling between a reactive excited state and the stable ground state.

Experimental investigation of the excited state relaxation in DNA base pairs can be quite difficult because the bases have very short excited state life times and there exist many cluster isomers. Therefore, the PCET reaction (called H-transfer below) was first studied in detail in 2-AP dimer by time-resolved measurements and FEICO spectroscopy. The results of this chapter as well as of the other chapters are compared with theoretical calculations. A short glossary of chemical notations used in the text are given in Appendix B.

A number of theoretical and experimental studies investigated H-bound complexes that mimic base pairs in systems with reduced complexity. One well investigated model system is 7-azaindole (7-AI) dimer. A proton transfer reaction in this dimer provides a fast isomerization of the base pair like structure to its tautomeric form (fig. 3.2). Early time-resolved measurements found two time constants in the excited

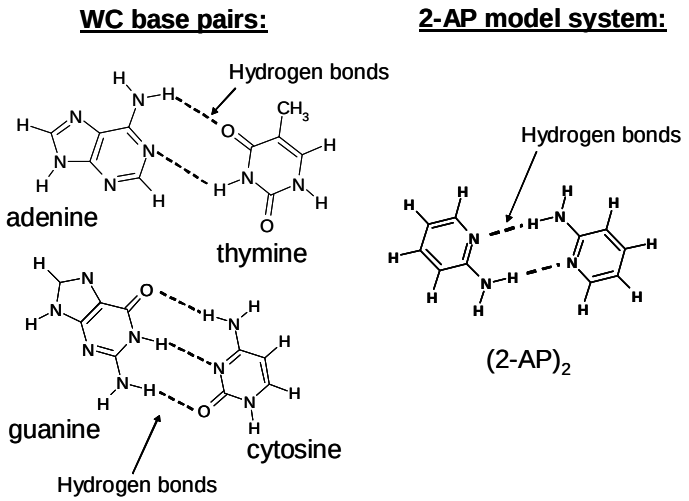

Figure 3.1: The Watson-Crick (WC) DNA base pairs compared to the mimetic model system $(2\text{-AP})_2$.

state dynamics of $(7\text{-AI})_2$, with fs and ps life times [19]. It was assigned to a step-wise isomerization process via single-proton transfer (SPT).

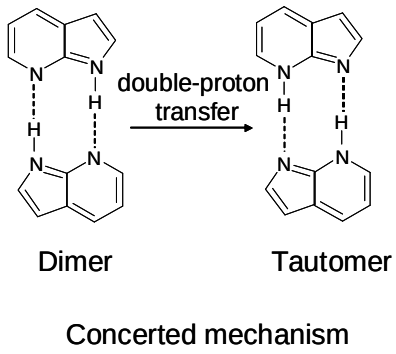

Figure 3.2: Concerted mechanism for double-proton transfer in $(7\text{-AI})_2$.

However, in later experimental studies [20, 21] it was confirmed that 7-AI dimer undergoes a simultaneous double-proton transfer (DPT) on the ps time scale (fig. 3.2). The fast fs transient was explained as an internal conversion between vibrationally excited ^1L_b-type and the ^1L_a-type states. Hence, the 7-AI dimer is not an ideal model system for the photoinduced H-transfer in DNA base pairs, since theoretical studies [7, 22] showed that only SPT plays a role in DNA base pairs. Additionally, $(7\text{-AI})_2$ lacks an amino group involved in the hydrogen bonding of WC base pairs and shows

strong fluorescence in contrast to DNA. $(2\text{-AP})_2$ was proposed [7] to be a better model system for adenine-thymine (A-T) and guanine-cytosine (G-C) base pairs.

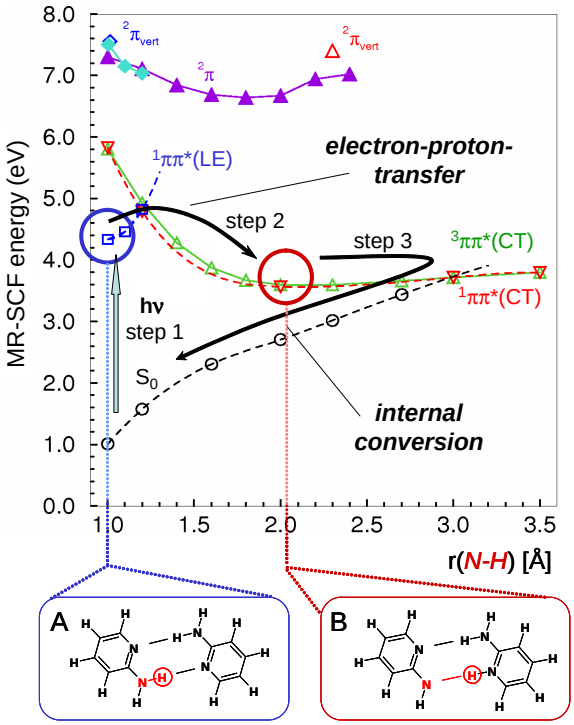

Figure 3.3: *Ab initio* PES of the electronic ground state S_0 (empty circles), the locally excited (LE) state (empty squares), and the charge transfer (CT) state (dark empty triangles) of 2-AP dimer as a function of a single-proton transfer coordinate r_{N-H} [7]. The curves above 6 eV are cationic states for the LE state (filled light squares) and for the CT state (filled dark triangles). The structures A and B correspond to molecular structures before and after the H-transfer. The vertical arrow ($h\nu$, step 1) illustrates vertical excitation from S_0 to the $\pi\pi^*$ (LE) state. Step 2 and step 3 show the relaxation pathway.

The mechanism of H-transfer in $(2\text{-AP})_2$ was first investigated in detail by theory. Fig. 3.3 shows potential energy surfaces (PES) for $(2\text{-AP})_2$ calculated with the CASSCF [1] method with a perturbative treatment of dynamical electron correlation effects ([7]). Energies are shown for the ground state (GS), low-lying excited states (ES) and ionic states. According to the calculations, after excitation of the $\pi\pi^*$ (LE) state with a photon $h\nu$ (vertical arrow, step 1), the population can relax from the LE state to the lower-lying $\pi\pi^*$ (CT) state (step 2). The LE to CT transition corresponds to a transfer of an electron from the highest π orbital of one monomer to

[1] complete-active-space self-consistent-field

the lowest π^* orbital of the other. The CT state is then stabilized by the subsequent transfer of a proton along one of the hydrogen bonds as shown in fig. 3.3A, and B. The population in the CT state can then decay via internal conversion back to the GS (step 3). The latter radiationless relaxation should be rapid due to strong coupling between the GS and the CT state in the proton transfer geometry [7]. The described relaxation pathway could be a very efficient ES quenching mechanism for hydrogen-bound complexes. In contrast, in 2-AP monomer, where formation of a CT is not possible due to absence of a partner, the ES life time was estimated to be much longer (1.5 ns), using rotational spectroscopy in the gas phase [23].

A single H-transfer reaction similar to that described for $(2\text{-AP})_2$ was predicted for the most stable WC conformers of G-C and A-T base pairs by recent *ab initio* calculations [24]. Frequency-resolved experiments in the group of de Vries investigated the corresponding systems [25]. Since the study of WC conformers of DNA base pairs is difficult due to their abundance in the molecular beam, chemical substitution was used to obtain measurable amount of WC conformers. Natural WC structures and unnatural base pairs were investigated. The absorption spectra for natural and unnatural structures of G-C base pairs (fig. 3.4) showed a pronounced difference in the spectral line width for the different species.

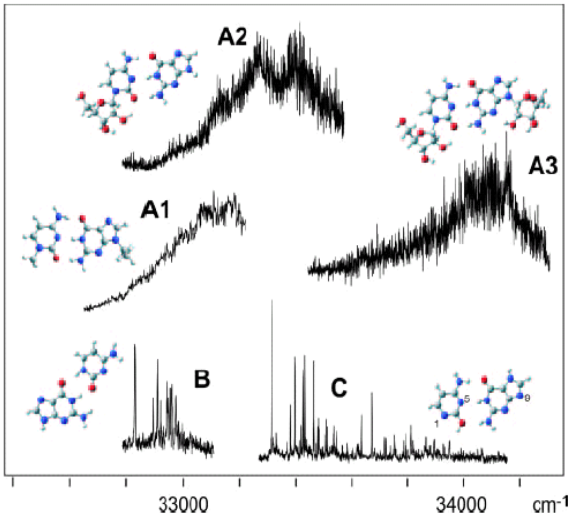

Figure 3.4: REMPI spectra of guanine-cytosine base pairs (reproduced with permission from ref. [25]). WC-type structures were expected for base pairs between 9-ethylguanine and 1-methylcytosine (A1), cytidine and guanine (A2), cytidine and guanosine (A3). For base pairs between guanine and cytosine (B and C) non-WC structures are expected.

The non-WC conformers B and C exhibited spectra with narrow line-widths, whereas the WC structures A1-A3 showed only very broad bands. The difference in the line width for these structures was assigned to different life time broadening. It was estimated that the WC structures have a very short excited state life times ($\sim 10^{-14}$ s) in contrast to the non-WC structures ($> 10^{-12}$ s) [25]. These results indirectly imply a specific ultrafast excited state relaxation pathway for the WC structures possibly related to the predicted H-transfer. Before our work, no direct time-resolved measurements of the excited state dynamics in isolated DNA base pairs were published in the literature.

3.2 Mass and electron spectroscopy of 2-AP clusters: experimental evidence for the H-transfer reaction

The predicted H-transfer reaction [7] was observed and characterized by the excited state dynamics measurements of 2-AP clusters. Semi-empirical and quantum chemical calculations were performed to identify cluster structures and explain their complex dynamics. The electronic structure of the $(2\text{-AP})_1$ and $(2\text{-AP})_2$ was studied using electron coincidence spectroscopy.

3.2.1 Excited state dynamics in 2-AP clusters

In cluster experiments, mass spectroscopy is a necessary experimental tool to assign the cluster species in the molecular beam. As described in sec. 2.1, different cluster distributions (CD) could be obtained by varying experimental parameters. A narrow CD in our experiments corresponded to $(2\text{-AP})_n$ clusters with the ratio between the cluster sizes n=1 : n=2 : n=3 of 100 : 1 : 0.01. Otherwise it was classified as a broad CD. Examples of mass spectra for a very broad CD with $(2\text{-AP})_n$, n=1...5 and a narrow CD, n=1, 2 are shown in the fig. 3.5a, and b.

The dominant signals in the spectra belong to the clusters of 2-AP. Small signals with the masses 67, 117, and 146 are due to covalent fragmentation of 2-AP resulting in -HCN loss, indole (added for calibration purposes), and the residual molecule

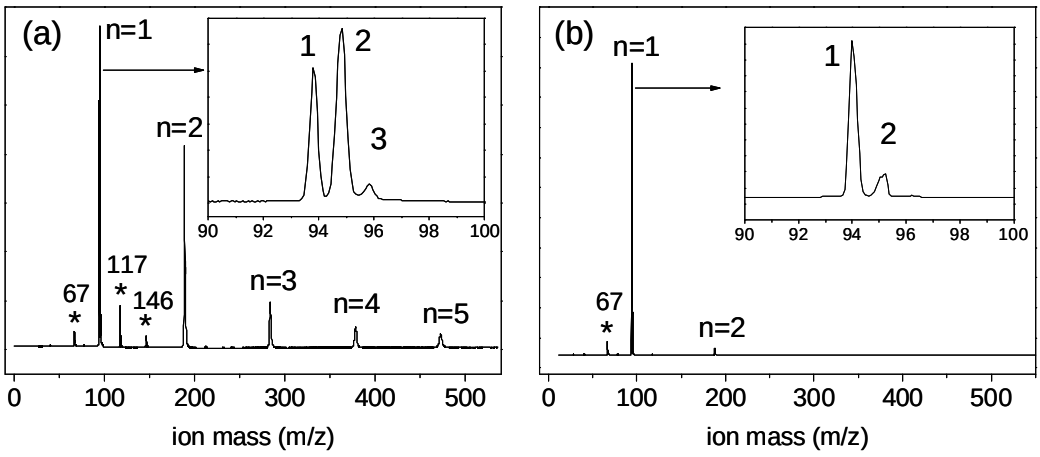

Figure 3.5: Mass spectra of $(2\text{-AP})_n$ clusters with a broad (a) and narrow (b) cluster distribution measured with 250 nm (a) or 293 nm (b) excitation and 800 nm multi-photon ionization. The inserts show the monomer signal. The monomer peak contains the ion mass signal from the molecular beam (1), a background gas signal (2), and a small isotopic peak from the background gas due to ^{13}C and ^{2}D isotopes (3). The isotopic signal from the molecular beam is hidden under background peak (middle). The big peak due to background gas (a) indicates not an ideal molecular beam adjustment. This peak was significantly decreased in later experiments (b). The peaks marked with asterisks are due to fragments and described in the text.

dimethylaminobenzonitrile, respectively. The signal amplitudes for the clusters are roughly proportional to the amount of the corresponding clusters in the molecular beam. Since the mass spectra were measured with the parallel extraction scheme (see sec. 4.1), the mass peaks have a double structure (shown in the inserts for $(2\text{-AP})_1$ in fig. 3.5). The peak on the left with m/z $\simeq$ 94 corresponds to the ion mass from the molecular beam, whereas the broader peak in the middle (m/z $\simeq$ 95) is due to the same molecules which are resident in the spectrometer and lack an additional velocity component of the molecular beam (background gas). The small peak on the right (m/z $\simeq$ 96) is an isotopic signal of the background gas, whereas the isotopic signal of the molecular beam (m/z $\simeq$ 95) is not seen due to the background signal. The background peak for the monomer is quite intense, which indicates not an ideal adjustment of the mass spectrometer in the early experiments (fig. 3.5a). In later measurements, the background signals were significantly suppressed, which is shown in fig. 3.5b (insert). The double structure is seen for the monomer and the dimer,

whereas for the bigger clusters the two mass peaks merged together into one broad peak due to the limited mass resolution.

The cluster distribution in our experiments was an important observable to interpret the obtained results. The CD was varied frequently to check how the width of the cluster distribution affected the measured dynamics. We observed that bigger clusters, which are weakly bound by hydrogen bonds easily fragmented into smaller clusters or the monomer. We could distinguish two types of fragmentation, neutral and ionic, which will be described in sec. 3.3. Both fragmentation channels contributed to the observed cluster dynamics. We also observed covalent fragmentation of $(2\text{-AP})_1$ with a -HCN loss (mass 67 in the mass-spectrum), which was laser intensity dependent and did not affect the measured dynamics.

The excited state dynamics for clusters was observed by accumulating mass-spectra for different time delays between the pump and the probe pulses. The amplitudes of each mass peak were plotted as a function of the time delay. Fig. 3.6 shows time-resolved mass traces for the 2-aminopyridine monomer and dimer, measured with 274 nm excitation and 800 nm ionization.

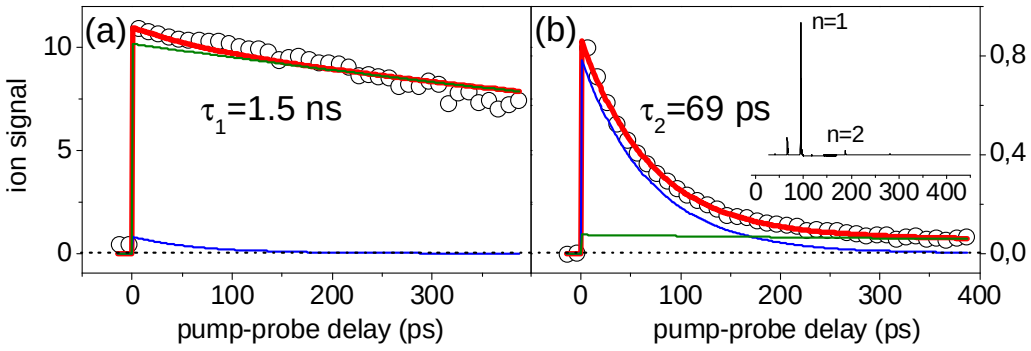

Figure 3.6: Time-resolved ion signals of 2-AP monomer (a) and dimer (b) with 274 nm excitation and 800 nm ionization. The thick lines are the total fit curves for the experimental points (circles). The fit contributions are shown with the thin lines. The contributions with small amplitudes in both traces are due to fragmentation. The constants τ_1 and τ_2 are the life times of the LE states in the monomer and the dimer.

The time-dependent signal of the monomer was fitted with a mono-exponential decay with a life time of 1.5 ns (fig. 3.6a). Due to the limited range of pump-probe delays available with our setup (400 ps), we could not determine this life time with confidence and the value was adopted from the rotational band contour analysis in the literature [23]. The 1.5 ns decay was assigned to the life time of the first locally

excited (LE) state of $\pi\pi^*$ character in the monomer [23]. A shorter-lived signal in the monomer mass channel (visible only as ∼10% of the total signal) was attributed to dynamic processes in the dimer which subsequently fragmented into the monomer mass channel.

The excited state dynamics for the 2-AP dimer measured at the same excitation wavelength looks drastically different (fig. 3.6b). Ignoring a signal due to fragmentation of bigger clusters, the ES life time for $(2\text{-AP})_2$ was measured as 69 ps. The significant shortening of the life time in comparison with the monomer confirmed the theoretical prediction of a different relaxation mechanism in the dimer. Therefore, the 69 ps decay was assigned to the H-transfer reaction from the LE state to the CT state as shown in fig. 3.3. The further decay of the CT state to the ground state was not observed in our data, which indicates that relaxation process is very rapid.

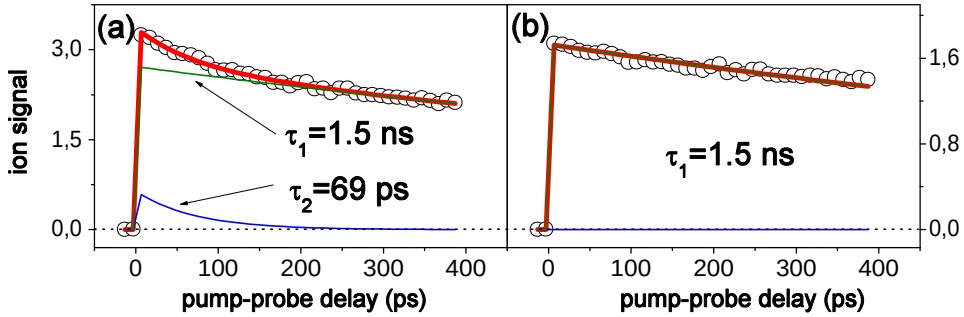

Figure 3.7: Time-resolved ion signal of 2-AP trimer (a) and tetramer (b) with 274 nm excitation and 800 nm ionization. The thick lines are fit curves for the experimental points (circles). The fit contributions are shown with the thin lines. The dynamics for the trimer consists of two exponentially decaying traces, with the life times τ_1 and τ_2. The excited state of $(2\text{-AP})_4$ decays mono-exponentially with the life times τ_1.

The photoinduced excited state dynamics was also investigated for bigger $(2\text{-AP})_n$ clusters with n $\geq$ 3. It was expected that bigger H-bound clusters should show a similar dynamics to that of the dimer due to the same H-transfer reaction.

In the dynamics of the trimer, a double-exponential decay with a ps and a ns life time was found (fig. 3.7a). Both of these transients were assigned to the specific dynamics of the trimer, indicating that the trimer exhibits dynamics resembling the monomer (ns life time) and the dimer (ps life time). However, we can expect

an additional contribution (∼10%) to the ns transient due to fragmentation of the tetramer.

For the tetramer, the dynamics consisted of a single-exponential decay (fig. 3.7b) with a life time of 1.5 ns, identical to the monomer decay. No characteristic dynamics indicating the presence of a H-transfer channel was found. The same dynamic behavior was observed in clusters with n > 4.

3.2.2 Cluster structure simulations

To interpret the complex dynamics measured for the (2-AP) clusters, a fundamental understanding of the relevant cluster structures is necessary. We performed semi-empirical PM3 calculations with the HyperChem 7 package to identify stable molecular structures for the $(2\text{-AP})_n$ clusters, n=1...4. A number of different starting geometries were used for the optimization of each cluster species.

The calculations identified only one stable configuration for the monomer and the dimer. The structure of the monomer (fig. 3.8a) was a quasi-planar molecule with a pyramidal amino group. The structure for the dimer showed a quasi-planar H-bound configuration (fig. 3.8b). The structures for the monomer and the dimer obtained with our PM3 semi-empirical calculations were in a good agreement with those obtained by high-level *ab initio* calculations [7].

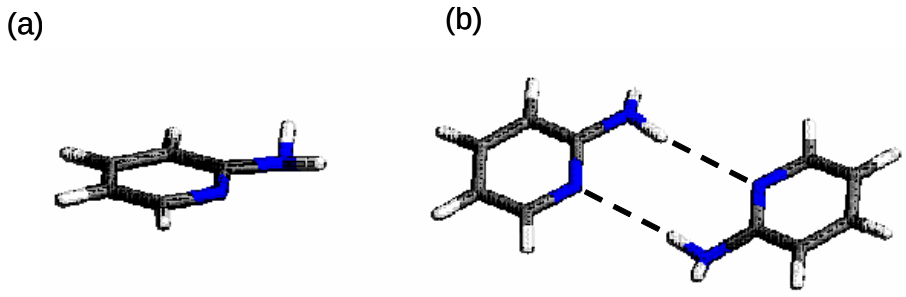

Figure 3.8: Semi-empirical structures of 2-AP monomer (a) and dimer (b).

For the trimer and tetramer, no high-level calculations existed. Our PM3 calculations identified several different cluster structures. For the trimer, the structures could be assigned to two different classes. In the first class (fig. 3.9a,b), two molecules were bound with two strong double H-bonds similar to the structure found in the dimer. The third molecule was held in the cluster by a π-stacking interaction of the aromatic

rings.

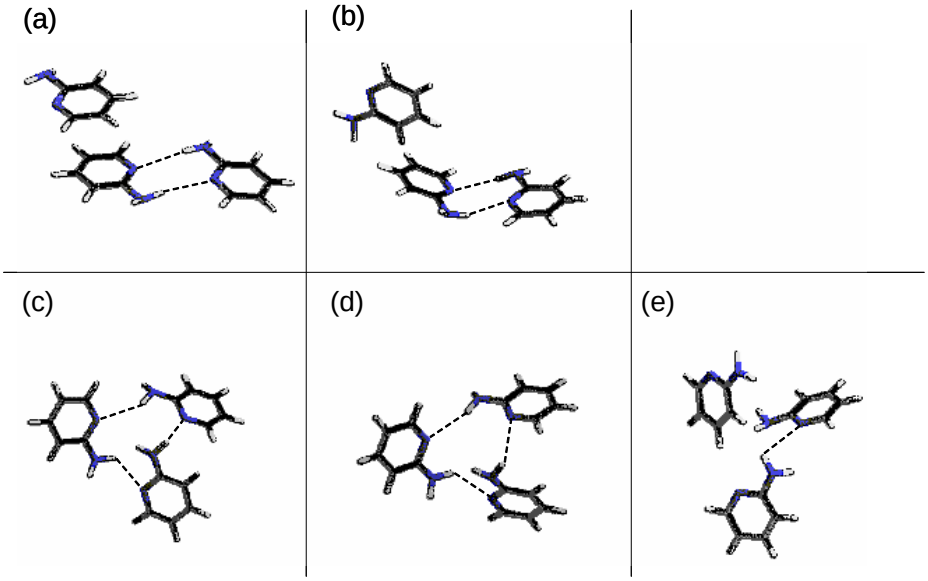

Figure 3.9: Semi-empirical structures of 2-AP trimer.

The second class of trimer structures is shown in fig. 3.9c-e. In these structures, only single H-bonds between two adjacent 2-aminopyridines were found.

The semi-empirical structure simulations for the trimer were later complimented by higher-level *ab initio* calculations of M. Kabeláč in the group of P. Hobza in Prague. The calculations revealed many almost isoenergetic structures. Non of them was dominant at the PES, as well as non of them was much more stable than the others. Fig. 3.10 shows seven lowest-energy *ab initio* optimized structures in their stability order.

The isomer (a) represents the global minimum structure, although not the most populated one at room temperature. The structures (b)-(g) differ in energy only slightly and are local minimum structures. Three different classes of structures were identified: a stacked configuration (S), a t-shaped configuration (T), and hydrogen-bound configuration (HB). Most of the structures were found in T/T configuration (67 %), where all three molecules are t-shaped oriented relative to each other (fig. 3.10a,c,e). 27 % of the structures were found in S/T configuration, where two molecules were stacked and the third one was t-shaped oriented relative to them (fig. 3.10d,f). And only a few percents of trimers (HB) contained double H-bonds (fig. 3.10b).

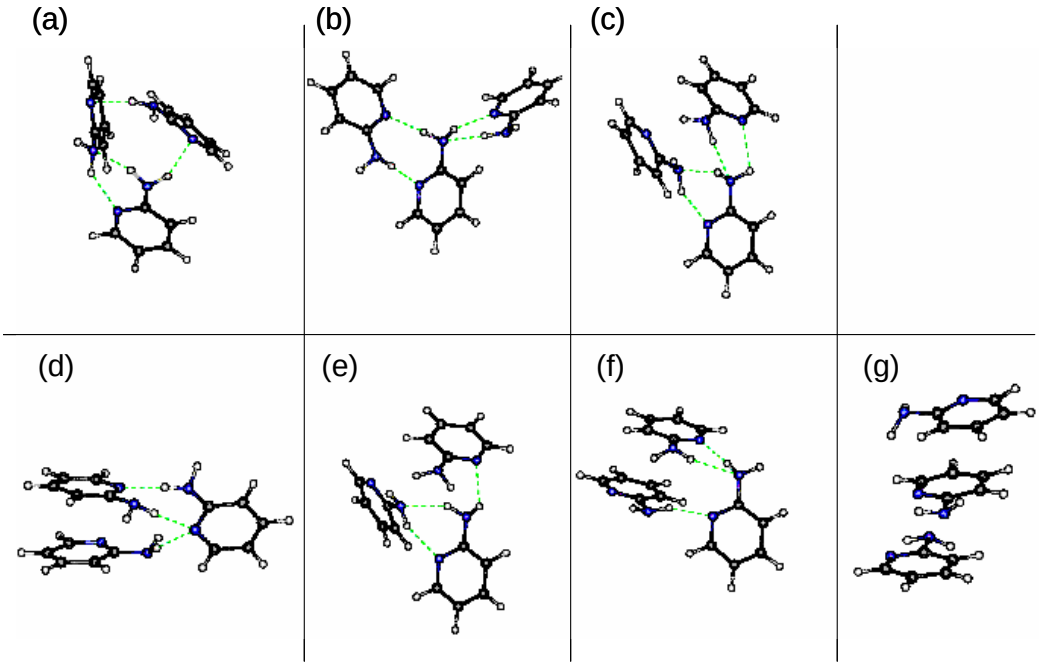

Figure 3.10: The most stable *ab initio* optimized trimer configurations. The structure (a) is a global minimum structure, the structures (b)-(g) are local minimum structures.

Comparing the structures in the figs. 3.9 and 3.10, we concluded that the general features of the trimer clusters were reproduced with the semi-empirical PM3 method. However, this simplified method is not suited for a detailed characterization of molecular aggregates. For example, in all cases, strength of the H-bonds was underestimated by PM3. The lengths of the H-bonds in the PM3 simulations varied between 0.2 and 0.3 nm as compared to *ab initio* calculated bond lengths of $\sim$ 0.2 nm.

The PM3 simulations were also performed for the tetramer. Two stable structures are shown in fig. 3.11 and are highly symmetric. No double H-bonds were found between the molecules.

Thus, the simple semi-empirical simulations helped to interpret the measured dynamics of the clusters: the 1.5 ns decay was associated with a relaxation of the excited monomer which does not have a partner for a H-transfer, and the 69 ps decay was attributed to the doubly H-bound dimer as predicted by *ab initio* calculations [7]. The dynamics of $(2\text{-AP})_3$ contained both, the ns and the ps decays. The structure calculations showed that many isomers can be present in the molecular beam. Some

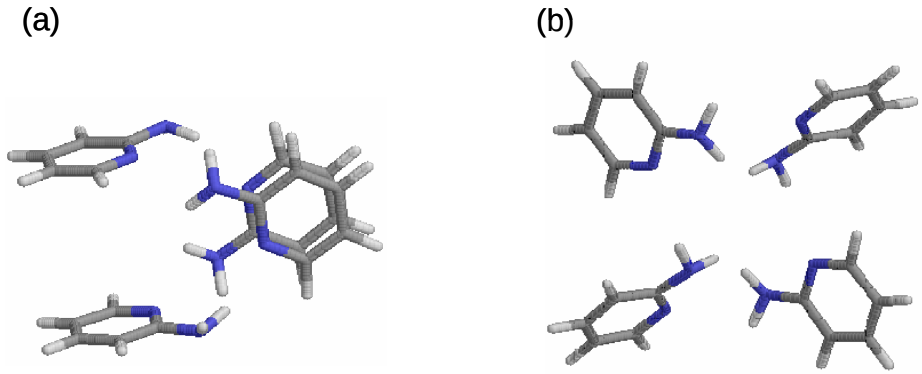

Figure 3.11: Semi-empirical structures of 2-AP tetramer.

of them have doubly H-bound substructures and may relax via a H-transfer with a 69 ps life time. Other isomers do not have this structure and are expected to decay from the LE state to the ground state with a 1.5 ns life time like the monomer. In the tetramer, where no doubly H-bound molecules were found, the dynamics was identical to that of the monomer [26].

3.2.3 Electronic structure of 2-AP monomer and dimer

Further information about the H-transfer reaction was obtained by combining the time-resolved measurements with coincidence electron spectroscopy. Two excitation wavelengths of 274 nm and 250 nm were used to access different vibrational levels of the LE $\pi\pi^*$ state in the monomer and the dimer. Ionization was done with two photons of 400 nm. The measurements were carried out at zero delay between the pump and the probe pulses and at 20 ps delay. The cluster distribution was kept as narrow as possible to avoid fragmentation of larger clusters. But a small amount of bigger clusters of $(2\text{-AP})_n$ with $n \geq 3$ was present in the molecular beam. For all pump-probe spectra one-color contributions were subtracted.

Monomer

In the photoelectron spectra of the monomer, only one electronic band corresponding to the ionization of the LE state was expected. Since the life time of the LE state in the monomer was measured to be 1.5 ns with 274 nm excitation (fig. 3.6a), the shape

and the amplitude of the electron spectrum should not change significantly within the ps time range investigated here. Indeed, the spectra at delays $\Delta t = 0$ ps and $\Delta t = 20$ ps shown in fig. 3.12a look very similar. We can compare the obtained electron spectra with the excited state dynamics of the monomer discussed in subsec. 3.2.1 and shown in fig. 3.12c. As the excited state population decays slowly, with the life time of the LE $\pi\pi^*$ state (τ_1=1.5 ns), the signal amplitude does not change significantly within 20 ps delay time. The similarity between the amplitudes of the photoelectron spectra and the time-resolved ion spectra therefore indicates that the population remains within the same electronic $\pi\pi^*$ state of the monomer when the molecules are excited with a moderate excess energy of 0.363 eV (274 nm).

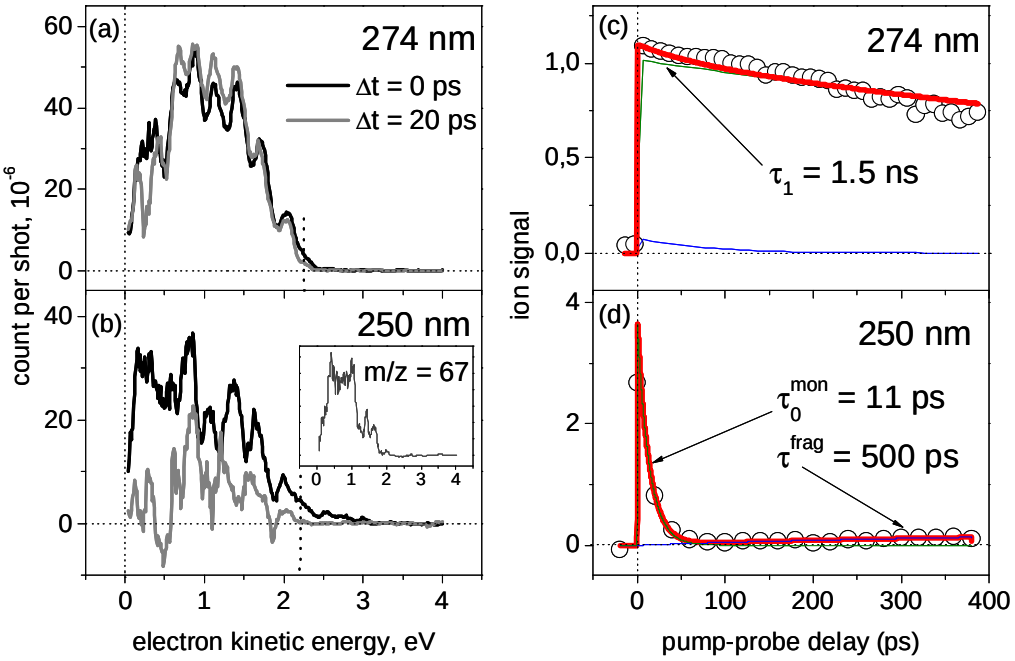

Figure 3.12: Electron spectra (left) and the excited state dynamics (right) of 2-AP monomer excited at 274 and 250 nm and ionized with 2 photons of 400 nm. Signals for the pump-probe delays $\Delta t = 0$ ps (black) and $\Delta t = 20$ ps (grey) are shown. The insert in fig.3.12b shows a spectrum of the covalent fragment of $(2\text{-AP})_1$ (m/z = 67). The vertical dotted line shows the electron kinetic energies which correspond to the experimentally observed adiabatic ionization potentials IP_{ad}^{exp}. Intensities of the electron signals (a, b) are in good agreement with those of the time-resolved ion signals (c, d).

Different results were obtained with 250 nm excitation (fig. 3.12b). The decrease of the amplitude of the delayed spectrum correlates well with the decay of the time-

resolved ion signals shown in fig. 3.12d. We observed an accelerated dynamics of the monomer (τ_0^{mon}=11 ps) when molecules are excited with a large excess energy of ≃0.8 eV (250 nm). Within 20 ps delay time the signal amplitude decreased significantly which is also reflected in the electron spectra. A detailed explanation of the faster monomer dynamics with 250 nm excitation will be presented later (see also fig. 3.13). The electron spectra at $\Delta t = 0$ ps and $\Delta t = 20$ ps in fig. 3.12b are similar in the electron kinetic energy range between 1 and 3 eV. Below 1 eV, we observed a reduced signal for the delayed spectrum, which could be due to the covalent fragmentation of the monomer (see fig. 3.5). In the insert of fig. 3.12b the electron spectrum of the covalent fragment with mass 67 is shown. The signal peak between 0 and 1 eV in the fragment spectrum coincides with the loss of the monomer signal in this range. The slightly negative signals observed in the delayed spectrum of the monomer may have resulted from the subtraction of one-color signals in the presence of fragmentation. We could assume two different scenarios. The first scenario assumes that the pump and the probe spectra are fragmentation free. A fragmentation due to sufficient excess energy in the ion then occurs only after the simultaneous absorption of both, the pump and the probe photons. As second possibility, an extra pump photon could be absorbed during measurements of the pump-probe spectra. This large excess energy in the ionic state will lead to a very efficient fragmentation of the excited molecule. In both cases, the sum of the measured one-color pump and probe signals can exceed the pump-probe signal leading to negative amplitudes in the spectra after subtraction. Additionally, laser energy fluctuations on a long time scale can also distort the signal, since the pump-probe and one-color spectra were measured sequentially.

From the electron spectra obtained from $(2\text{-AP})_1$ (fig. 3.12a, and b), vertical and adiabatic ionization potentials were calculated (Eq. (2.13)). The experimental value of the adiabatic IP was determined as an onset of the broad electron band in the spectra. For the spectrum obtained with 1×(274 nm) + 2×(400 nm) ionization, this onset was at E_{el}^{max}=2.25 eV leading to the experimental adiabatic ionization potential IP_{ad}^{exp}=8.48 eV (dotted vertical lines). This value was ∼0.37 eV higher than the literature value of 8.11 eV [27]. This difference may be explained with the fact that ionization took place via a resonant excited state. According to the Frank-Condon principle, the excess energy in the excited state should be transferred into the cationic state. The $\pi\pi^*$ state origin in $(2\text{-AP})_1$ was reported in the literature at 4.162 eV (298 nm). Therefore, excitation at 274 nm (4.53 eV) leads to population of vibronic states 0.368 eV above the $\pi\pi^*$ origin. This is almost exactly the difference

between the measured IP_{ad}^{exp} and the literature value. For the 1×(250 nm) + 2×(400 nm) ionization process (fig. 3.12b), the IP_{ad}^{exp} value was 8.96 eV, which was again higher than the literature value of 8.11 eV. The energy difference of 0.85 eV again matched the excess energy in the excited state of ∼0.8 eV.

Vertical ionization potentials were determined as the maxima of the electron bands. The values obtained from our spectra were 9.85 eV and 10.31 eV for 274 nm and 250 nm excitation, correspondingly. Taking into account the excess vibrational energy in the ES, we extrapolate an IP_v of 9.48 eV and 9.51 eV for vibrationally cold molecules.

A vibrational progression with a spacing of ∼0.30 eV was found in the monomer spectra (fig. 3.12a). Based on preliminary calculations [28], we can suggest that this progression is due to a structural change along an intramolecular H-transfer coordinate for amino-imino tautomerization of the monomer.

Concerning the time-resolved dynamics of the monomer in fig. 3.12c,d, a significant shortening of the life time at different excitation wavelengths was observed. The dynamics measured with 250 nm excitation, contained two transients. A transient with a rise time of 500 ps was assigned to excited state fragmentation of bigger clusters. Types of fragmentation will be further discussed in the sec. 3.3.1. The 11 ps trace was assigned as the life time of the LE state in the monomer. The shorter life time could indicate a different relaxation mechanism, when the $\pi\pi^*$ state is excited with a high excess energy. To shed some light on such alternative relaxation pathways, *ab initio* calculations were performed in our group by Dr. H.-H. Ritze.

In the *ab initio* calculations, C_1 symmetry was assumed using a aug-cc-pVDZ basis set (see Appendix B). The energies of the neutral ground and excited electronic states were determined by means of the second-order approximate Resolution-of-the-Identity Coupled Cluster (RI-CC2) method. Ionization potentials were determined with the Complete Active Space Second-order Perturbation Theory (CASPT2). Geometry optimizations were conducted at the RI-MP2 (Second-order Resolution-of-the-Identity Møller-Plesset theory) level (for the determination of ionization potentials) and at the RI-CC2 level (determination of electronic excitation energies) [29].

The calculations revealed another electronic excited state of $n\pi^*$ character above the bright LE $\pi\pi^*$ state in the monomer. The calculated vertical excitation energy of the $n\pi^*$ state was 5.234 eV. For an approximate planar geometry, assumed for the calculations, a conical intersection of the $\pi\pi^*$ and $n\pi^*$ states was found at $\sim$ 4.75 eV. This intersection point can be easily reached by 250 nm (4.96 eV) excitation, but

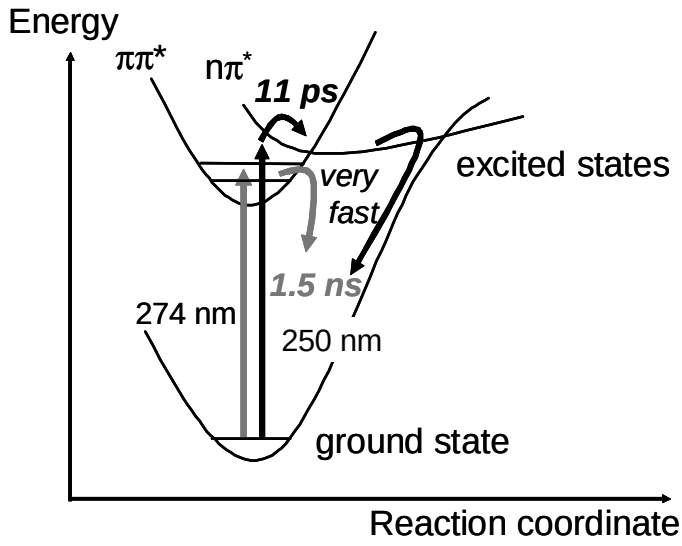

Figure 3.13: Schematics of the proposed excited state decay mechanism in $(2\text{-AP})_1$. An intersection with the higher electronic $n\pi^*$ state accelerates the relaxation of the optically excited LE $\pi\pi^*$ state and leads to observed excited state life time of 11 ps. The intersection point can be reached with 250 nm excitation, but not with 274 nm.

not with 274 nm (4.53 eV). No higher-lying electronic states accessible with a photon wavelength of 250 nm were identified by the calculations. Therefore, we propose that a conical intersection (CI) between the $\pi\pi^*$ and $n\pi^*$ electronic states accelerates the excited state relaxation of the LE state. The subsequent relaxation of the $n\pi^*$ state could be very rapid, and no additional transient was identified in the dynamics of the monomer (fig. 3.12d).

Dimer

The electron coincidence spectra of $(2\text{-AP})_2$ measured with 274 nm or 250 nm excitation are shown in fig. 3.14 and fig. 3.15. The monomer spectra plotted with dotted lines are shown for comparison.

The spectra of the dimer measured with 274 nm excitation at $\Delta t = 0$ and $\Delta t = 20$ ps resemble each other. They are also similar to the monomer spectra except for the much smaller signal amplitudes due to the small amount of dimers in the molecular beam. The negative amplitudes are due to subtraction of one-color signals as discussed before, and therefore the interpretation of the band shapes is only unambiguous for the energy range above ∼1 eV. Since the one-color signals were measured separately,

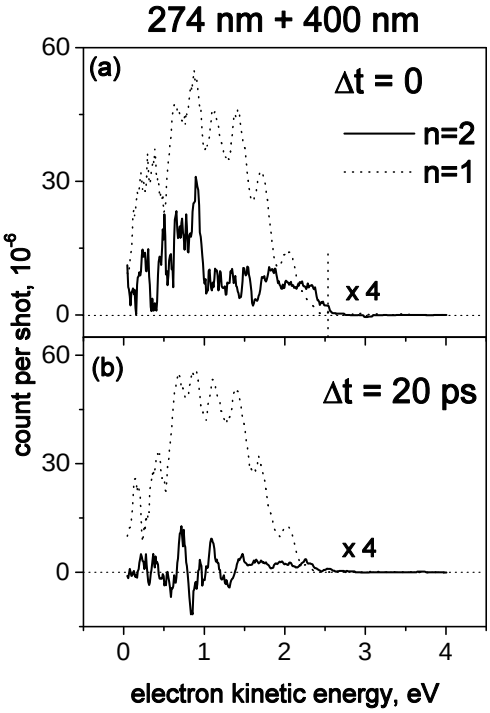

Figure 3.14: Electron spectra of 2-AP dimer (solid line) measured with 1×(274 nm) + 2×(400 nm) ionization process at $\Delta t = 0$ (a) and $\Delta t = 20$ ps (b). The amplitudes of the dimer signals are multiplied for easier viewing. The monomer spectra (dotted curves) are shown for comparison. The vertical dotted line shows the electron kinetic energies which correspond to the experimentally observed adiabatic ionization potentials IP_{ad}^{exp}.

the structure of the band below ∼1 eV could be distorted by the subtraction of one-color signals. Nevertheless, the similarity between the monomer and the dimer spectra at $\Delta t = 0$ indicates that an electronic state of the same $\pi\pi^*$ character was populated upon vertical excitation. At the delay $\Delta t = 20$ ps, the shape of the dimer spectrum remained unchanged, whereas its amplitude is decreased. This indicates a relaxation of the initially excited electronic state, but no change in the electronic character of the excited state. The decrease of the amplitude in the spectra at $\Delta t = 0$ and $\Delta t = 20$ ps is in a good agreement with the time-resolved dynamics of the dimer measured with 274 nm excitation (fig. 3.6b).

The experimentally observed adiabatic ionization potential IP_{ad}^{exp} obtained from the dimer spectrum at $\Delta t = 0$ (dotted vertical line) was 8.17 eV, which is 0.30 eV lower than the value for the monomer at the same excitation wavelength. Since the

adiabatic IP for $(2\text{-AP})_2$ was not measured before, comparison with literature values was not possible.

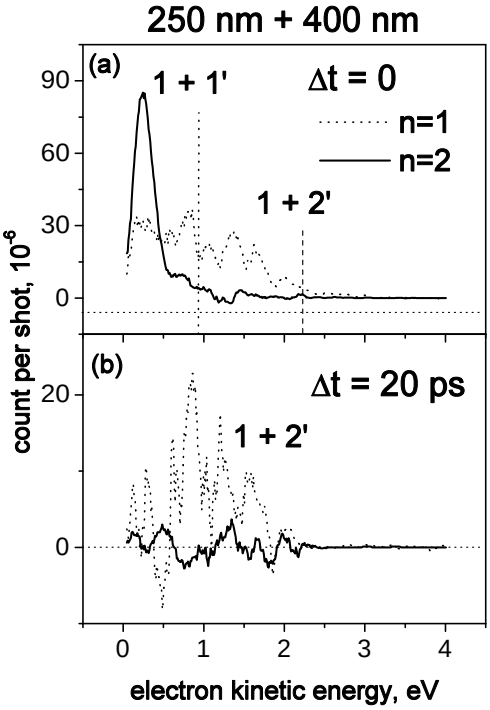

Figure 3.15: Electron spectra of 2-AP dimer (solid line) measured with a 1×(250 nm) + 1×(400 nm) and 2×(400 nm) ionization process at $\Delta t = 0$ (a) and $\Delta t = 20$ ps (b). The monomer spectra (dotted curves) are shown for comparison. The vertical dotted and dashed lines show the electron kinetic energies which we assigned as the observed adiabatic ionization potential IP_{ad}^{exp} for 1×(250 nm) + 1×(400 nm) and 1×(250 nm) + 2×(400 nm) ionization.

With a higher excitation energy (250 nm), the electron spectra of the dimer at $\Delta t = 0$ differ significantly from the monomer spectrum (fig. 3.15a). The amplitudes of the signals are shown without scaling. The dimer amplitude is approximately a factor of two higher than that of the monomer. This can not be explained with a bigger amount of dimers in the molecular beam, because mass spectra measured at 274 nm and 250 nm showed nearly identical cluster distributions. The high amplitude of the dimer spectrum can be explained with a different, more efficient ionization process, e.g ionization with a single 400 nm photon. The electronic band observed as a result of this process shows a lower adiabatic ionization potential of ∼7.11 eV (dotted line). Ionization via one pump and one probe photons (1+1') should be more efficient than

ionization of the monomer, for which two probe photons are necessary (1+2'). The higher energy part of the spectrum ($E_k > 1$ eV), which is characterized by a small amplitude, was assigned to the higher order ionization (1+2') process in the dimer, which is also expected. The IP_{ad}^{exp} for this process was higher (8.96 eV) as compared to the corresponding value for the monomer (8.11 eV).

At a delay of $\Delta t = 20$ ps (fig. 3.15b) the intense band in the dimer spectrum vanished and the remaining spectrum, albeit very weak, resembled that at $\Delta t = 0$ ps. The very different IP_{ad}^{exp} for $(2\text{-AP})_2$ excited with 250 nm indicates, that the intense band in the electron spectrum is not due to ionization of the LE $\pi\pi^*$ state in the dimer with the life time of ~70 ps. Time-resolved measurements of $(2\text{-AP})_2$ showed that the intense band in the electron spectrum observed at 250 + 400 nm ionization is characterized by a much shorter life time. Fig. 3.16 shows excited state dynamics of the dimer measured with low (274 nm) and high (250 nm) vibrational excess energy in the LE $\pi\pi^*$ state.

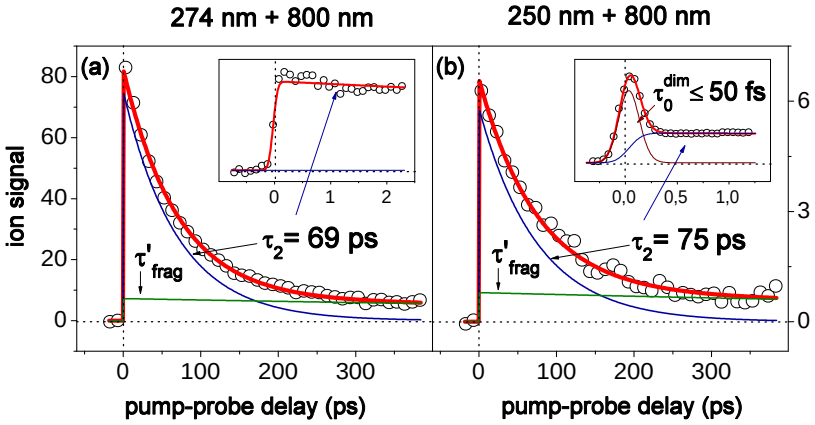

Figure 3.16: Time-resolved ion signals of $(2\text{-AP})_2$ measured with 274 nm and 250 nm excitation and 800 nm ionization wavelengths. The life time τ_2 characterizes the relaxation of the LE $\pi\pi^*$ state. The inserts show the dynamics on a very short time interval. An additional time constant τ_0^{dim} was found after excitation of high vibronic states at 250 nm and assigned to a vibrational dynamics in the ES (see inset). The time constant $\tau_{frag}^{'}$ was due to ionic fragmentation of bigger clusters.

On the picosecond time scale, dynamics for 250 and 274 nm show a single-exponential decay with $\tau_2 = 69$ ps and $\tau_2 = 75$ ps life times. As shown in the main traces of fig. 3.16, additional long lived signals with $\tau_{frag}^{'} = 1.5$ ns were assigned to

the fragmentation of bigger clusters. The inserts in the fig. 3.16 show the dynamics on a few picoseconds time scale. With low excess energy excitation (fig. 3.16a), no fast fs dynamics was observed. After higher energy excitation with 250 nm (fig. 3.16b), we observed fs decay component with a life time of $\leq$50 fs. The limited time resolution of our experiments did not allow to determine this life time more precisely. This short-lived signal was correlated with the intense electronic band in the dimer spectrum shown in the fig. 3.15a.

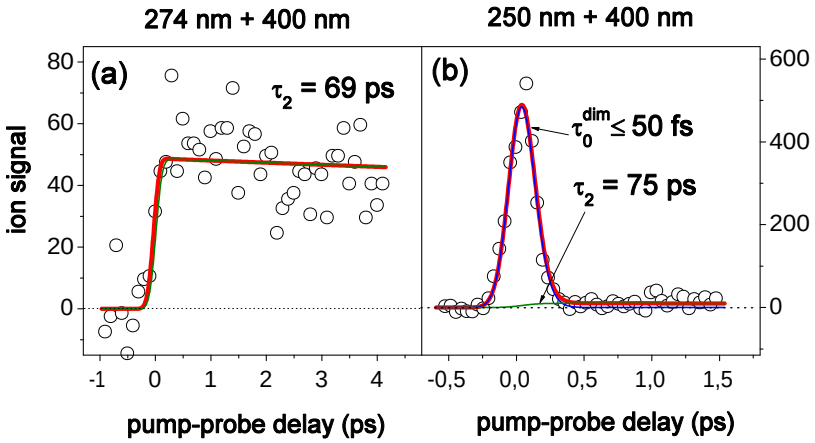

Figure 3.17: Time-resolved ion signals of $(2\text{-AP})_2$ measured with 274 nm and 250 nm excitation and 400 nm ionization wavelengths. The dynamics reproduce those observed with 800 nm ionization as seen in the inserts of fig. 3.16, but the τ_0^{dim} amplitude is strongly enhanced.

Identical excited state relaxation was observed with 400 nm probe pulses. The short time dynamics measured with 274 nm excitation (fig. 3.17a) was nearly identical to that shown in fig. 3.16a (insert). With 250 nm excitation, the amplitude of the trace with fs life time τ_0^{dim} was much stronger then that with ps life time τ_2. The latter was still visible as a small signal at positive delays. The time-resolved dynamics obtained with the 2×400 nm ionization process (fig. 3.17) can be directly correlated with the electron spectra of the dimer in fig. 3.15. The signal amplitude of the electron spectrum obtained with 1+1' ionization decayed almost to zero and corresponded to the transient with a life time of ∼50 fs. The remaining signal (1+2' ionization) was assigned to the LE state of the dimer with the 75 ps life time, was seen as a small signal in fig. 3.17b.

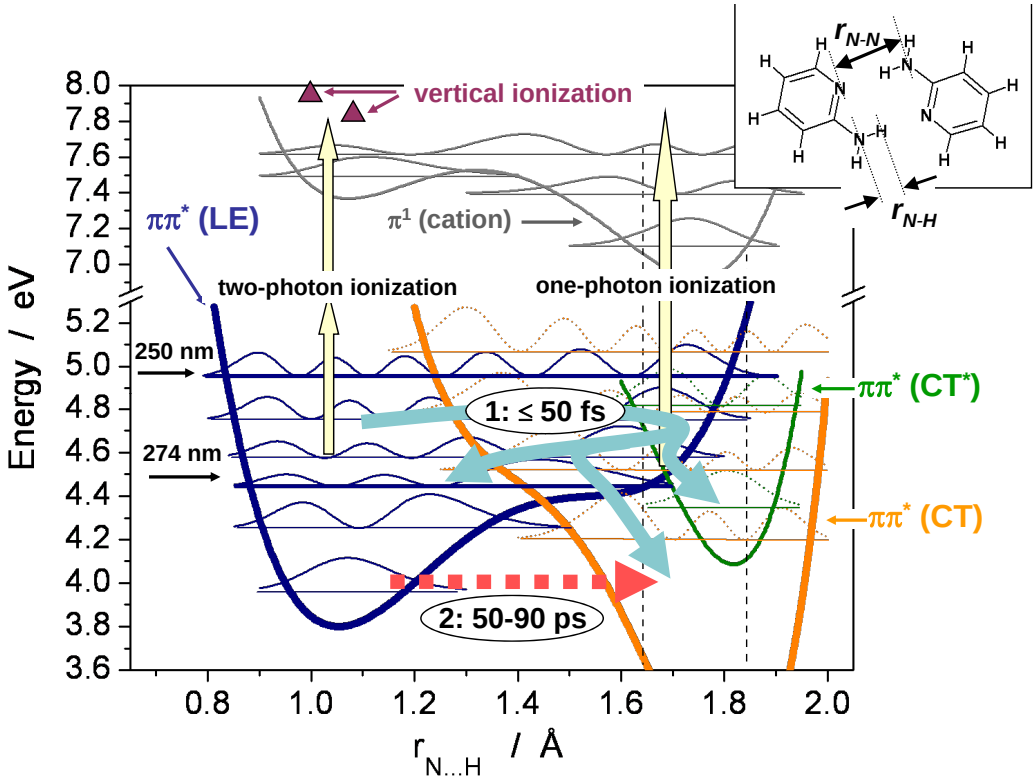

Figure 3.18: Calculated PES of low excited states of $(2\text{-AP})_2$ as a function of the H-transfer coordinate for an intermolecular distance $r_{N...N}$ of 2.8 Å. The full triangles indicate the calculated vertical ionization potentials from the ground and the LE states. The arrow 1:≤50 fs illustrates the proposed relaxation pathway from a vibrationally excited $\pi\pi^*$ state via a fast (≤50 fs) vibrational energy redistribution to CT and CT* states, as well as to the minimum of the $\pi\pi^*$ state. The arrow 2:50-90 ps shows the relaxation pathway via a slow (50-90 ps) internal conversion between the $\pi\pi^*$ and CT states.

To get a better understanding of the photoinduced processes in the dimer with different excitation energies, we carried out *ab initio* calculations[2] of the PES for the LE, CT and the cationic states (fig. 3.18). Similar calculations for neutral ground and excited states were published in literature by Sobolewski and Domcke [7], but these authors investigated the system only with respect to the H-transfer coordinate ($r_{N...H}$), while keeping the planar geometry of the dimer and optimizing the remaining coordinates. In the calculations presented here, we also considered the intermolecular distance, which strongly affects the H-transfer coordinate. The potential-energy surfaces were calculated for three intermolecular distances $r_{N...N}$ = 2.6, 2.8, and 3.0

[2]all *ab initio* calculation in this work were carried out by Dr. H.-H. Ritze, if not stated otherwise

Å. The geometry was optimized for all remaining coordinates. Fig. 3.18 shows the results of the calculations for an intermolecular distance $r_{N...N} = 2.8$ Å. The excitation energies corresponding to 274 and 250 nm are indicated with arrows on the left. The vibrational levels of the N-H mode in the LE electronic state and the CT (also CT*) states are plotted as solid and dashed lines correspondingly. The cationic state was calculated along excited state geometry. The full triangles indicate calculated vertical ionization energies for the ground state equilibrium geometry (7.957 eV) and for the LE $\pi\pi^*$ state equilibrium geometry (7.805 eV) [29]. On the basis of these calculations our experimental results can be interpreted by two distinct relaxation pathways in $(2\text{-AP})_2$ depending on the excitation wavelength. (1) The excited state (ES) relaxation of the dimer at high excitation energy (250 nm), can be understood if we take into account the inharmonicity of the electronic and cationic states. When a lot of vibrational energy is deposited in the LE $\pi\pi^*$ state, ionization is possible from the outer turning point at large $r_{N...H}$ distances along the H-transfer coordinate (one-photon ionization). The geometry of the LE state at the outer turning point is similar to a cationic state geometry at its global minimum. The corresponding low ionization potential allows a low-order (1 + 1') ionization process. The ultrafast relaxation constant ($\leq$50 fs), which was observed in the time-resolved measurements, was therefore assigned to a rapid intramolecular energy redistribution between vibrational degrees of freedom in the dimer. Presence of energetically accessible conical intersections with the CT and CT* states may accelerate the decay of selected vibrationally excited levels of the LE $\pi\pi^*$ state. The equilibrium geometry of both charge transfer states (CT and CT*) is similar to that of the cation. However, ionization of the CT state requires two probe photons, whereas only one photon is needed to ionize the CT* state. The observed intense electronic band in the dimer spectrum in fig. 3.15a therefore could result from 1 + 1' ionization of the LE state at the outer turning point and the CT* state. (2) The second relaxation pathway in the dimer with a time constant $\tau_2 = 50$-90 ps is observed when a moderate amount of vibrational energy is transferred into the LE state at an excitation wavelength of 274 nm. The picosecond relaxation time was assigned to an internal conversion between the LE and the CT state. The conical intersection with the CT* state is not directly accessible and ionization is possible only with two probe photons (1 + 2') from the minimum of the LE state. The ps relaxation pathway is also observed with 250 nm excitation and 400 ionization as a minor contribution in the electron spectra and in the time-resolved signals of the dimer. At 800 nm ionization, however, the ps relax-

ation pathway was observed as the dominant process in time-resolved dimer signals [29].

3.3 Wavelength dependence and isotope effect in 2-AP clusters

In the previous sections, we showed experimental evidence for the theoretically predicted H-transfer in $(2\text{-AP})_2$. With 250 nm excitation, fast ($\tau_0 \leq 50$ fs) vibrational energy redistribution between the LE $\pi\pi^*$and the CT states was observed as well as a slower (τ_2 = 50-90 ps) internal conversion through a reaction barrier. With 274 nm excitation wavelength, only the latter process was found to be active. In this section, the rate of this internal conversion is discussed. The excitation wavelength was varied between 296 nm (close to the excitation threshold) and 250 nm. This experiment allowed us to study the coupling between the LE and CT states as a function of excess energy in the initially excited LE $\pi\pi^*$state. The barrier was also investigated by isotopic substitution of the relevant H-atoms with deuterium.

The section will begin with the detailed characterization of cluster fragmentation, which is a major problem in the interpretation of our data.

3.3.1 Cluster fragmentation channels

In our experiments with clusters, two types of fragmentation were observed: fragmentation in the ionic state or in the excited neutral state. Fragmentation in the ions was briefly mentioned in subsec. 3.2.1. It was noticed that weakly bound bigger clusters can easily fragment into smaller clusters when enough energy is absorbed in the ion. The fig. 3.19 shows excited state dynamics of the dimer (right) measured with the same excitation and ionization wavelengths but with different cluster distributions (seen in the mass spectra, fig. 3.19, left). When larger clusters were absent (narrow CD), the dimer dynamics was fitted with a single-exponential decay (fig. 3.19, bottom). In the presence of bigger clusters, an additional long-lived time constant in the dimer dynamics was observed. We already showed that bigger clusters have a ns life time, therefore this contribution in the dimer dynamics was assigned to fragmented bigger clusters.

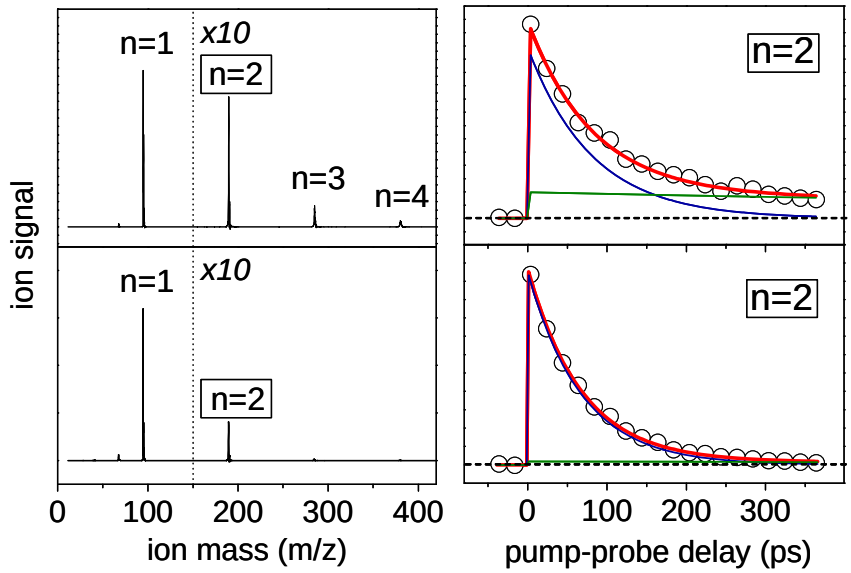

Figure 3.19: Mass spectra (left) and time-resolved ion signals of $(2\text{-AP})_2$ (right) measured with 293 nm excitation and 800 nm ionization. For the broad cluster distribution (top) the dimer dynamics was fitted with a double-exponential decay, where the long-lived component is due to ionic fragmentation of bigger clusters. This component vanishes for the narrow cluster distribution (bottom).

In fig. 3.20 we show the ionic fragmentation mechanism (a) and how this fragmentation changed the observed cluster dynamics (b). Characteristic life times assigned to bigger clusters were found also in the signals of smaller clusters as shown in fig. 3.20b. E. g., in the trimer dynamics, two decay components with the life times τ_1 and τ_2 were identified. After fragmentation in the ion, these life times can be observed in the dimer mass channel ($3 \rightarrow 2$). Since pure dimer dynamics contains only mono-exponential decay with the life time τ_2 (see fig. 3.19), the τ_1 contribution to the dimer signal was assigned to the ionic fragmentation of the trimer and possibly bigger clusters. The same situation was observed in the monomer, the native dynamics of which contains a mono-exponential decay with the life time $\tau_1 = 1.5$ ns in the absence of clusters. The small amount of signal with life time τ_2 originates from fragmented dimer ($2 \rightarrow 1$) and, perhaps, trimer ($3 \rightarrow 1$).

The second type of fragmentation was observed, when the clusters were excited into high vibronic states of the neutral species. Those conditions were fulfilled with 250 nm excitation ($\sim$0.8 eV above 0-0 transition). In this case, clusters have enough

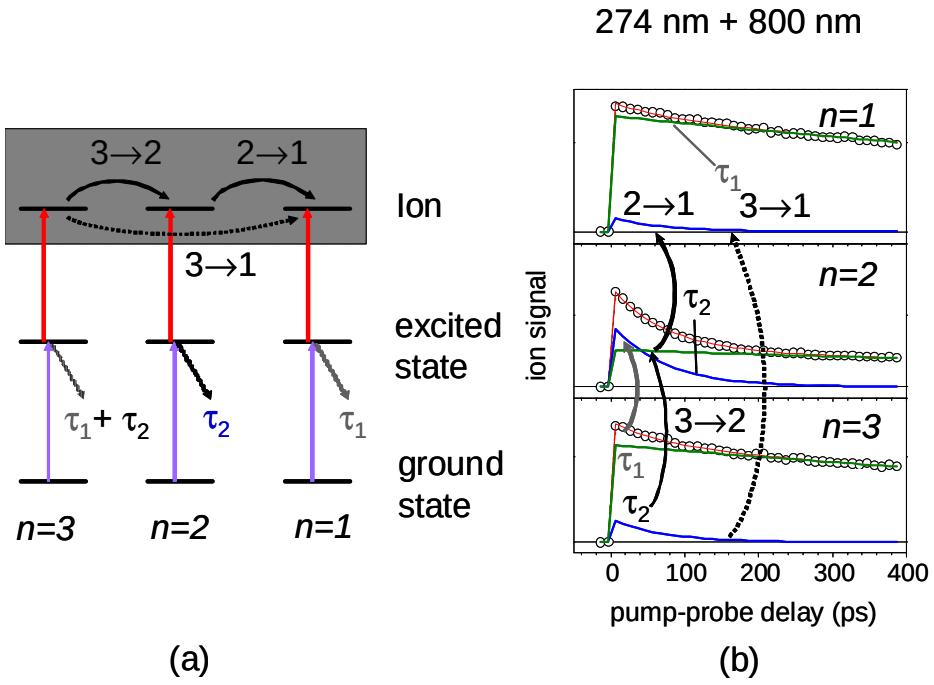

Figure 3.20: Scheme of ionic fragmentation in clusters (a) and the measured excited state dynamics influenced by fragmentation (b). The arrows in (b) show how the signals are transferred from bigger to smaller clusters. The life times of the trimer are observed in the dimer ($3 \rightarrow 2$) and the monomer ($3 \rightarrow 1$) dynamics. The life time of the dimer is also present in the monomer signal ($2 \rightarrow 1$).

vibrational energy to fragment in the excited state (fig. 3.21a). The fragmentation decreases the excited state population of the fragmenting clusters and increases the population of the products. This process was observed in the monomer mass channel as a rising signal with the life time $\tau^{frag(3\rightarrow2\rightarrow1)} \simeq 500$ ps corresponding to the fragmentation of bigger clusters (n=2, 3). Experimentally, the excited state fragmentation was easier distinguishable from the ionic one, because it introduced an additional rate constant in the cluster dynamics. The life time τ_1 observed in the monomer dynamics was due to ionic fragmentation as described above and it disappeared for narrow cluster distribution (fig. 3.12d).

3.3.2 Wavelength dependence of the H-transfer reaction

The rate of the H-transfer reaction in 2-AP dimer as a function of excess energy in the excited state was investigated by pump-probe experiments with different excitation

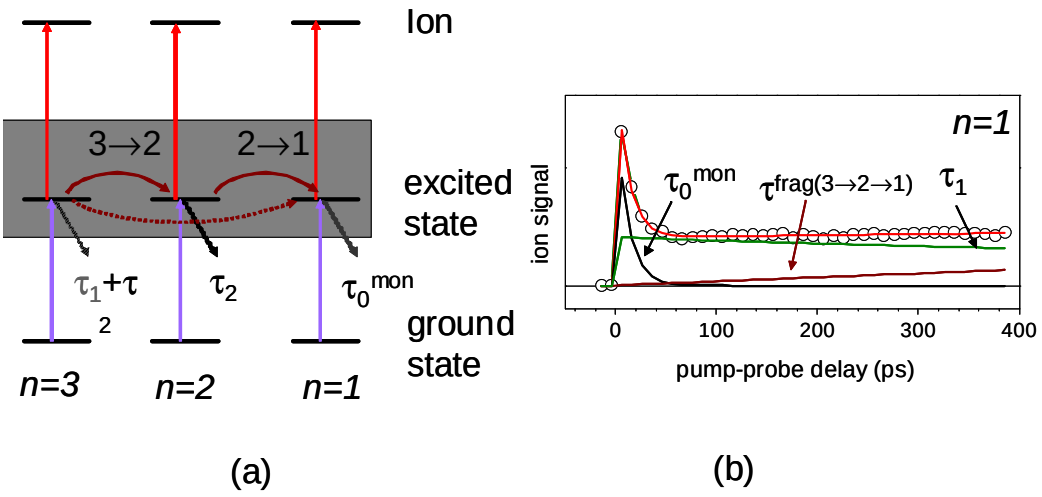

Figure 3.21: Scheme of excited state fragmentation in clusters (a) and the measured dynamics of the monomer where the fragmentation product was observed (b). The $\tau_0^{mon} = 11$ ps is the life time of the LE state in the monomer after 250 nm excitation, whereas $\tau^{frag(3\rightarrow2\rightarrow1)}$ is due to excited state fragmentation of clusters. The time constant $\tau_1 = 1.5$ ns is due to ionic fragmentation of bigger clusters and vanished for narrow cluster distribution.

energies. In these experiments, we expected to excite the same LE $\pi\pi^*$ electronic state, but we increase the internal (vibrational) energy in the system. If the hydrogen-transfer rate is controlled by a reaction barrier, we may expect accelerated reaction rates at higher energies.

Fig. 3.22 shows excited state dynamics measured with 296 nm, 293 nm, 274 nm, and 250 nm excitation and multiphoton 800 nm or 400 nm ionization. The transient signal measured with an excitation wavelength of 293 nm was fitted with a mono-exponential decay with a life time of 50 ps. No signal due to fragmentation of bigger clusters was identified in this time-resolved signal. For all other excitation wavelengths, a fit with a double-exponential decay was necessary to reproduce the measured dynamics. In those traces, the dominant decay contribution τ_2 was assigned to the excited state life time of the dimers, whereas the slower decay with the life time τ_1 was assigned to the fragmentation of larger clusters. The observed fragmentation signals are proportional to amplitude of signals from larger clusters (measured independently) and can therefore be assigned unambiguously. The slowest excited state relaxation rate of the dimer $\tau_2 = 87$ ps was found for 296 nm excitation. This case corresponds to the lowest excess energy (0.24 eV) in the excited state. With increased excitation energy, the excited state relaxation becomes faster and we measured life

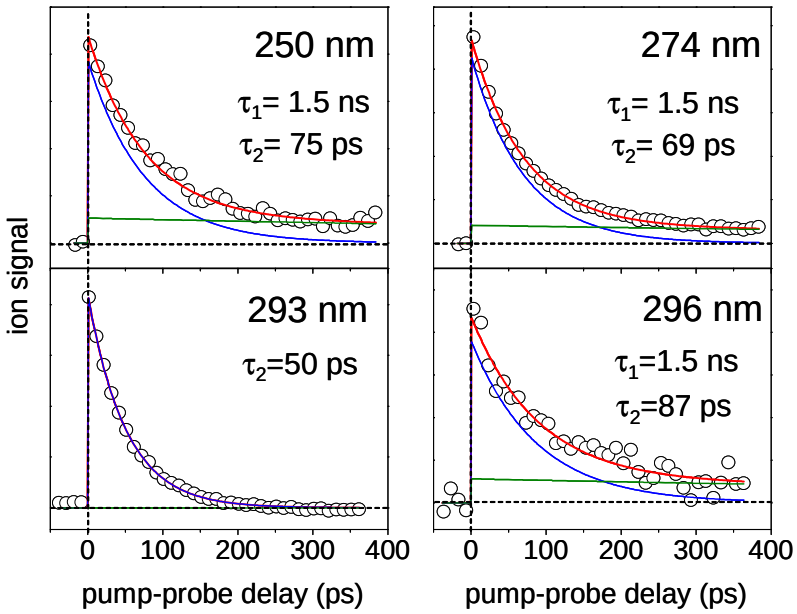

Figure 3.22: Time-resolved ion signals of the $(2\text{-AP})_2$ measured at different excitation wavelengths. The τ_2 constant is the excited state life time of the dimers. The τ_1 life time is due to the ionic fragmentation in the bigger clusters.

times of 50-75 ps, and the fastest ES relaxation was found for 293 nm excitation.

If a H-transfer reaction over a barrier would be the time critical reaction step, we would expect an increasingly faster reaction as a function of excess energy. This is in contradiction to the observed prolongation of the excited state life time between 293 and 250 nm. Our results for the dimer dynamics therefore do not support the picture of a simple reaction barrier. To explain the observed rates we consider the results from *ab initio* calculations performed by H.-H. Ritze. In the calculations the barrier height was investigated as a function of the intermolecular distance for three values $r_{N...N}$ = 2.6, 2.8, and 3.0 Å. The calculated barriers are shown in fig. 3.23. The largest intermolecular distance of 3.0 Å corresponded to the equilibrium distance in the electronic ground state and therefore the geometry for vertical excitation. The intermediate distance of 2.8 Å was close to the equilibrium distance in the $\pi\pi^*$ LE state. The calculations showed that the lowest barrier is expected for the small distance $r_{N...N}$ = 2.6 Å (A). As the intermolecular distance increases, the barrier height also increases (B, C). A higher reaction barrier will lead to a slower reaction rate which is shown by theoretically estimated excited state life times of <1 ps (2.6 Å), ∼40 ps (2.8 Å) and >200 ns (3.0 Å). Although, quantitatively we observed different

reaction rates in our experiment, qualitatively the trend remains: the reaction is fastest for 293 nm and it is slower at 296 nm, 274 nm, and 250 nm excitation.

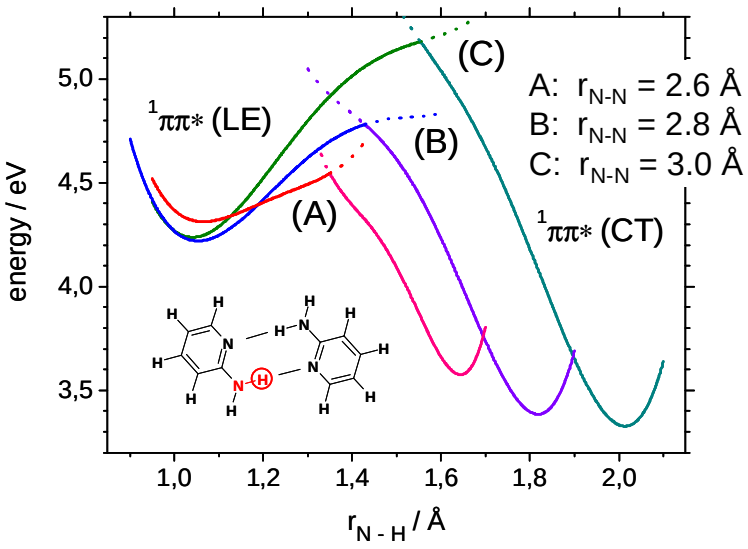

Figure 3.23: *Ab initio* calculated potential energy surfaces along the r_{N-H} coordinate in 2-AP dimer for three fixed intermolecular distances $r_{N...N}$ (A, B, C). The barrier height for the H-transfer reaction (along the r_{N-H} coordinate) increases with increasing the intermolecular distance r_{N-N}. A higher barrier may lead to a slower reaction.

3.3.3 Isotope effect in 2-AP dimer

The barrier for the H-transfer reaction in $(2\text{-AP})_2$ was also probed by isotopic substitution of hydrogen with deuterium. Because of their different masses, H and D have different zero-point vibrational energies. Along the H-transfer coordinate, the difference in zero-point energy leads to a different barrier height. Therefore, we expected to observe a large normal isotope effect for the H-transfer reaction.

Deuterated N,N-aminopyridine (D-AP, see fig. 3.24) was synthesized at the MBI by dissolving 2-AP in a 20-fold excess of deuterated water and by then removing the solvent in a rotary evaporator. This procedure was repeated three times. Before the measurements with the D-AP, we purged the sample lines for 1 hour with deuterated

water, using a bubbler and helium as a carrier gas. Nevertheless, the mass spectra still contained a considerable amount of undeuterated and monodeuterated aminopyridine.

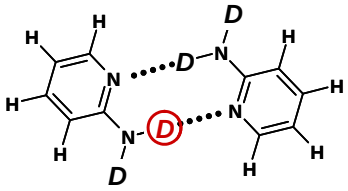

Figure 3.24: Deuterated N,N-aminopyridine dimer.

The isotope effect was measured at several excitation wavelengths: 250, 293, and 296 nm. In all cases ionization (probe) pulses at a wavelength of 800 nm were used. The pump-probe ion signals obtained are shown in fig. 3.25 (right). On the left-hand side we also show the corresponding mass spectra. The narrowest cluster distribution was obtained for the pump wavelength 296 nm, and the broadest - for 250 nm. The time-resolved ion signals were fitted with a double-exponential decay with life times τ_1 and τ_2. The transient with a life time τ_2 reflected the excited state life time of the $(\text{D-AP})_2$, whereas the transient with a life time τ_1 was assigned to ionic fragmentation of bigger clusters (n$\geq$2). The amount of big clusters in the mass spectra was proportional to the amplitudes of the transient with a life time τ_1 in the time-resolved signals (fig. 3.25).

For all excitation wavelengths, the life time τ_2 was found to be several hundred picoseconds, which is considerably longer than the life time of the undeuterated 2-AP dimer (see fig. 3.22).

The wavelength dependence in D-AP dimer was found to be monotonous. The shortest life time was found for the highest excess energy in the excited state (250 nm). Decreasing the excess energy led to increased life times up to a factor of $\sim$7 compared to the life times of undeuterated aminopyridine as can be seen in tab. 3.1. The error bars show the range of measured life times for three or more independent measurements.

Thus, by measuring the excited state dynamics of undeuterated $(\text{2-AP})_2$ and deuterated $(\text{D-AP})_2$, the expected large normal isotope effect was confirmed. This shows that there is a reaction barrier along the H-transfer coordinate as predicted by *ab initio* calculations [7].

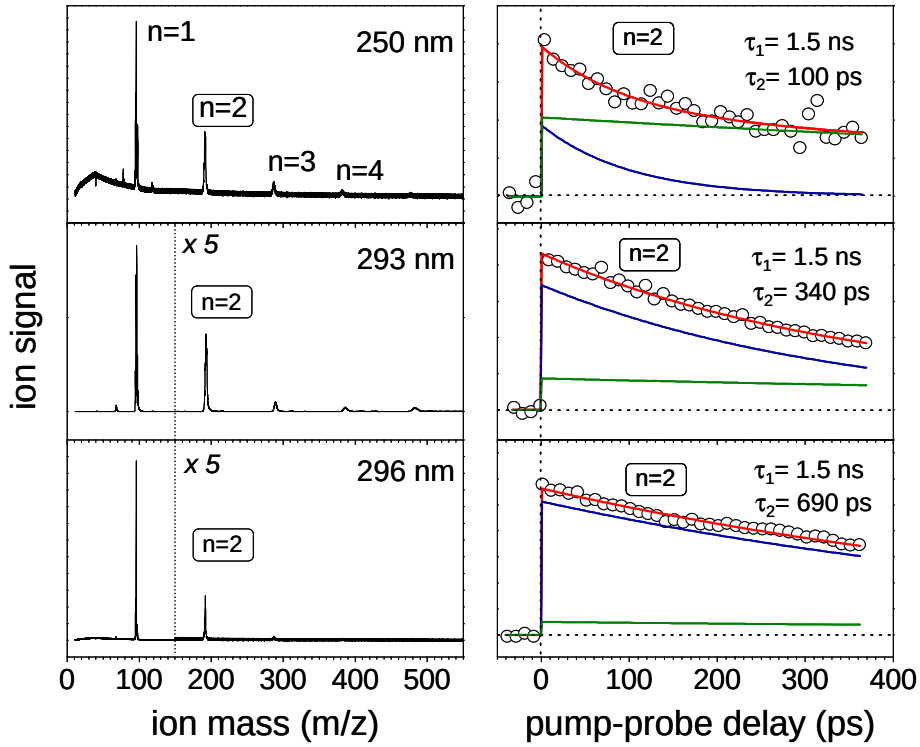

Figure 3.25: Mass spectra (left) and time-dependent ion signals (right) of the deuterated dimer $(D-AP)_2$ measured with 250, 293, and 296 nm excitation and 800 nm ionization. The excited state life time τ_2 increases with decreasing excess energy in the ES. The contribution with the time constant τ_1 was found to be proportional to the concentration of the signal amplitudes of bigger clusters and was assigned to fragmentation thereof.

Table 3.1: Measured life times τ_2(H) and τ_2(D) for undeuterated and doubly-deuterated aminopyridine dimers.

λ_{pump} (nm)	τ_2^H (ps)	τ_2^D (ps)	τ_2^D/τ_2^H
296	87 ± 20	600 ± 100	6.9
293	53 ± 5	340 ± 80	6.4
274	69 ± 10		
250	75 ± 15	160 ± 60	2.1

Chapter 4

Spectroscopy of isolated DNA bases and base pairs

4.1 Electronic excited states in DNA bases

The excited state properties of the nuclear bases adenine(A), thymine (T), cytosine (C), and guanine (G) has captured the interest of theoretical and experimental scientists for many years. As already mentioned, all DNA bases strongly absorb UV radiation. Excess energy in the excited state after absorption of a UV photon can cause photochemical reactions, destroy the DNA bases and therefore damage the genetic material. To be stable against photoinduced reactions, nuclear bases might have specific energy relaxation mechanisms to the electronic ground state. A detailed understanding of the time-dependent energy redistribution in the excited states is therefore an important step to understand the intrinsic photostability of DNA.

This chapter will present a literature overview and our experimental results for the isolated DNA bases adenine and thymine. We combined time-resolved mass spectroscopy with coincidence electron spectroscopy (FEICO) to determine the character of the excited states and their life times.

4.1.1 Adenine: literature overview of experiments and theory

Adenine is the most investigated molecule among the four nuclear DNA-bases. Its structure is shown in fig. 4.1. Adenine belongs to the molecular class of purines and

consists of a six-membered and a five-membered aromatic rings. In the DNA double helix, the H12 and the N1 atoms are hydrogen-bound with the adjacent base thymine and the H14 atom is substituted with a sugar-phosphate group. For isolated adenine several tautomers are discussed in the literature [30–34]. When a hydrogen (H14 atom) is coupled to the N9 atom, the tautomer is called 9H-adenine. Other low-lying tautomers are 7H-, 3H-, 1H-adenine, when hydrogen H14 is bound to the nitrogen atoms 7, 3, or 1 respectively [34].

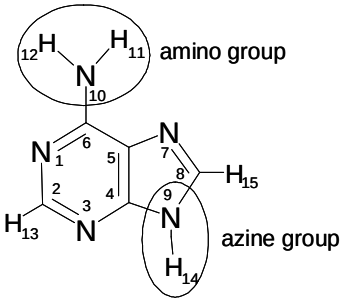

Figure 4.1: Structure of 9H-adenine. Numbering of the atoms according to ref. [35].

In our study of excited states we aimed at determining which electronic states play a role in the photophysics of DNA bases. Based on the molecular structure of the bases, we can make assumptions about the character of low-lying excited states. In adenine, the π-electrons of the aromatic rings give rise to $\pi\pi^*$ electronic excited states. Nitrogen heteroatoms with electron lone pairs participate in the formation of $n\pi^*$ excited states, whereas amino and azine groups contribute to formation of $\pi\sigma^*$ states.

Early experimental studies of adenine used absorption and emission spectroscopy in the liquid phase [36–38]. But the broad featureless spectra did not provide detailed information about the nature of the excited states. However, it was found that the fluorescence quantum yield of adenine, as well as that of the other nuclear bases, was very low, on the order of 10^{-4} [39]. A suitable explanation for this would be the existence of short-lived low-lying excited states or/and the presence of dark singlet or triplet states. Recent high-level theoretical calculations investigated the potential energy surfaces of the ground and electronically excited states of adenine in the gas phase [34, 40–44]. They offered a number of ideas for the interpretation of the experimental results. For the electronic ground state of adenine, many tautomers were found with semiemperical and *ab initio* methods [34]. The canonical form 9H-adenine

(fig. 4.1) is the most stable structure. The two rare amino tautomers, having hydrogens at N3 and N7, were calculated to be about 7 kcal/mol less stable in the gas phase. Whether these two structures can be expected in molecular beam experiments can be estimated based on the van't Hoff equation (Eq. (4.1)). Eq. (4.1) allows us to estimate an equilibrium ratio between the rare and the canonical tautomers at a given temperature:

$$K = exp\Big(- \frac{\Delta G_0}{RT} \Big), \tag{4.1}$$

where K is the equilibrium constant between the minor and the major tautomers, ΔG_0 is the difference in free Gibbs energies between the tautomers, $R = 8.31\ J \cdot K^{-1} \cdot mol^{-1}$ is the gas constant, and T is the temperature. Taking ΔG_0 equal to 7.43 kcal/mol and 7.47 kcal/mol for the 3H and 7H tautomers respectively [34] and setting T to a typical oven temperature of 500 K, we obtain a ratio between the rare tautomers 3H-adenine and 7H-adenine and the canonical 9H-adenine of 0.000564 and 0.000542. Hence, we expect that the amount of rare tautomers in gas phase experiments is negligibly small. Nevertheless, 7H-adenine was detected by IR-UV double resonance spectroscopy of Plützer et al. [45]. Our discussion will only refer to 9H-adenine, since, according to the above estimation, this is the predominant isomer and also the relevant biological structure in DNA.

Multiple theoretical studies were carried out to investigate the electronic states and their dynamics in isolated 9H-adenine [35, 40–44]. It was found that adenine has three low-lying singlet excited states, two of $\pi\pi^*$ type (usually labelled L_a and L_b states) and one of $n\pi^*$ type. There are several relaxation pathways for the excited states suggested in the cited literature. Schematic representation for these pathways are shown in fig. 4.3. The relaxation of the photoexcited L_b state can take place via a conical intersection CI 2 to the lower-lying $n\pi^*$ state [40, 44]. The minimum of the $n\pi^*$ state was found more stable than that of L_b state by approximately 0.2 eV [44]. The L_b state can also mix with the L_a state via a conical intersection CI 1 [35, 42, 44]. The L_a state can rapidly decay to the ground state (GS) via a conical intersection CI 3 or populate the $n\pi^*$ state via a conical intersection CI 2. These pathways were found to be almost barrierless (barrier < 0.1 eV). Another possible relaxation pathway (fig. 4.2b) is the internal conversion of the $n\pi^*$ state to the ground state via the conical intersection CI 4 [42, 44]. A higher activation barrier of 0.5 eV was estimated for this process [44]. Alternatively, the authors suggested that the $n\pi^*$ state population can escape to the ground state via the conical intersection CI 2, shown in fig. 4.2a, where the estimated activation barrier is only 0.1 eV. For each relaxation

pathway shown in fig. 4.2a and b, different reaction coordinates were identified. But because adenine has many degrees of freedom, other relaxation pathways may exist along other reaction coordinates.

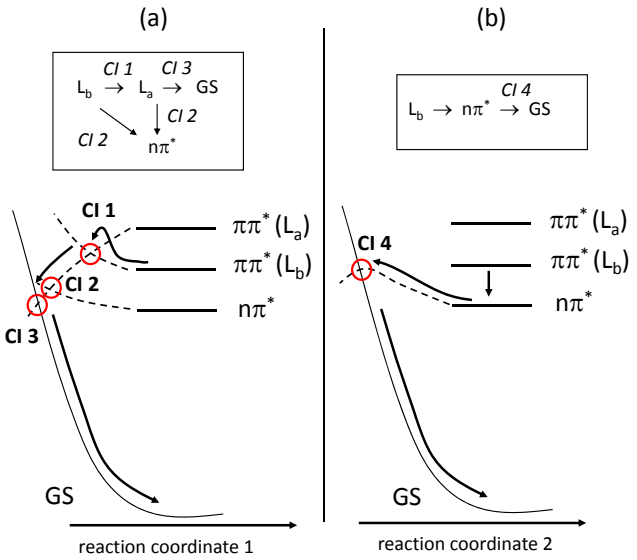

Figure 4.2: Proposed in literature relaxation pathways for 9H-adenine in the gas phase. Conical intersections (circles) between the $\pi\pi^*$ (L_a, L_b), $n\pi^*$, and ground states are labelled as CI 1....CI 4. Arrows on the diagram and inside the boxes schematically show relaxation pathways from the excited states to the electronic ground state (GS) along different reaction coordinates.

Perun and coauthors [43] also discuss the relevance of $\pi\sigma^*$ states for the excited state relaxation in adenine. The PES for two $\pi\sigma^*$ states were calculated with CASSCF (complete-active-space self-consistent-field)/CASPT2 (complete-active-space second-order perturbation theory) methods. For each $\pi\sigma^*$ state, a dissociative reaction coordinate along the NH bond length in the amino (a) and azine (b) groups (fig. 4.3) was calculated. The PES for both $\pi\sigma^*$ states were similar. In the ground state geometry, the $\pi\sigma^*$ states are located above the $\pi\pi^*$ (L_a and L_b) and the $n\pi^*$ states. One important feature of the $\pi\sigma^*$ states is that they cross the ground state at elongated N-H geometries. This means that the $\pi\sigma^*$ states may provide very fast relaxation pathways to the ground state. But this fast relaxation mechanism probably only plays a role at high excitation energies [46].

Experimental results were in good agreement with the described theoretical models. Resonance-enhanced multi-photon photoionization (REMPI) spectroscopy was

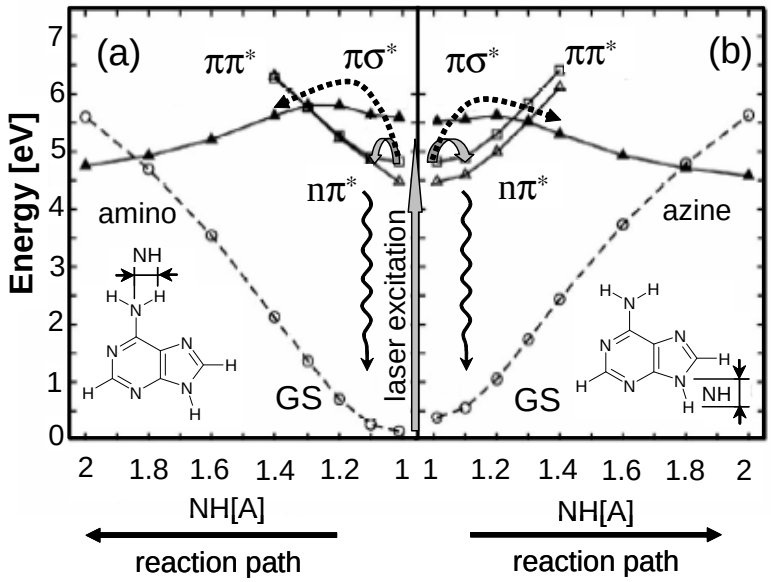

Figure 4.3: Potential energy surfaces of the ground state (open circles) and lowest excited states (open triangles, filled triangles, squares) of adenine along two different reaction coordinates: N-H bond length in the amino and azine groups (reproduced from ref. [43]). Filled and dashed arrows indicate internal conversion pathways for the population of the $n\pi^*$ and the $\pi\sigma^*$ states; waved arrows indicate the nonradiative relaxation pathways discussed above.

used to determine the character of the lowest excited states in adenine [47]. Kim et al. measured REMPI spectra of isolated adenine and found sharp lines in the range of 35430-36700 cm^{-1} (282.4-272.4 nm) and a broad band in the range of 36400-39930 cm^{-1} (274.7-250.4 nm). Based on the intensity of the sharp lines, the authors suggested that the lowest excited state of adenine is of $n\pi^*$ character, followed by a higher-lying $\pi\pi^*$ excited state. This agreed with the theoretically predicted order of the excited states [35, 42, 44]. Later, the group of Kleinermanns [48] confirmed the assignment of the lowest excited states using REMPI method combined with rotational band contour analysis. The strong mixing of the $\pi\pi^*$ and $n\pi^*$ states predicted by theory [35, 40, 42] was also confirmed. The same group used the IR-UV double resonance technique to demonstrate, that two tautomers, 7H-adenine and 9H-adenine, coexist in the molecular beam [45]. The signal from the minor 7H-tautomer was a factor of $\sim$ 13 smaller compared to the signal of the canonical 9H-form.

In time-resolved ionization experiments of adenine, a double-exponential excited state decay was found ([31, 49–55]). All authors agreed that two excited states were

populated. A fast transient with a life time of <100 fs was assigned to the optically bright $\pi\pi^*$ state, which was photoexcited from the ground state with the laser. A slow (0.75-9 ps) transient was assigned to the $n\pi^*$ state, populated via internal conversion (IC) from the $\pi\pi^*$ state. Electron spectroscopy [56] revealed two electronic bands in the spectra. The bands were assigned to the $\pi\pi^*$ and $n\pi^*$ states, based on their ionization potentials. The role of the $\pi\sigma^*$ state in the excited state relaxation was discussed to explain an additional contribution in the electron spectra at an excitation wavelength $\lambda_{ex} = 267$ nm [53, 54]. It is interesting, however, that the $\pi\sigma^*$ state was not detected with a shorter excitation wavelength of $\lambda_{ex} = 250$ nm. Stronger evidence for the $\pi\sigma^*$ state in isolated adenine stems from the observation of H-abstraction after excitation with 243.1 nm, 239.5 nm and 226-233 nm [46, 57, 58]. Detection of H-atoms in these experiments was interpreted as evidence for dissociation along the repulsive PES of the $\pi\sigma^*$ state. We have to mention here, that the source of the H-atoms in such experiments is still under discussion [46]. However, the laser energies, used for dissociation [46, 57, 58] agree with the theoretically predicted values for population of the $\pi\sigma^*$ state [35, 43].

Several groups [59–61] recently carried out excited state absorption and fluorescence up-conversion measurements on adenine in water. Their time-resolved experiments showed a double-exponential decay of the photoexcited states. As opposed to the gas phase results, the two decay components were not assigned to different excited states, but rather to different tautomers. A fast transient with a life time of ∼300 fs ([61]) was assigned to the natural form 9H-adenine, which is also the dominant isomer in the gas phase (shown in fig. 4.1). A slow transient with a life time of ∼8 ps was assigned to the 7H-adenine tautomer where the hydrogen is attached to the N7 position. Based on the existing experimental data, the nature of the excited states of 9H-adenine in solution can not be clearly assigned and high-level *ab initio* theory would be desirable. But because environmental effects must be taken into account, only lower-level computational methods were applied. Only the lowest electronic excited states of $\pi\pi^*$ and $n\pi^*$ character were considered in the calculations. CIPSI (multireference perturbation configuration interaction), CIS (configuration interaction with single electron excitation), and TDDFT (time-dependent density functional theory) methods predict a $\pi\pi^*$ character for the lowest excited state ([30, 62]). Energies of the relaxed excited states (adiabatic energies) were not calculated. Therefore, no predictions about the relaxation pathways can be made.

However, there is a general trend for solvation effects [6]: the $\pi\pi^*$ state is per-

turbed only slightly in polar solvents (usually red-shifted) and the $n\pi^*$ state is blue-shifted. We have to keep in mind, that the adiabatic excited state order is directly connected to the expected relaxation pathways. Since there is no consensus among the existing different theoretical and experimental works about the state order for solvated adenine, we must consider two scenarios. The first scenario is based on an order of the excited states which is the same as in isolated adenine: the $n\pi^*$ state is energetically lower than the $\pi\pi^*$ state. In this case, solvation may modify the life times of the excited states. The $\pi\pi^*$ state might be longer-lived in solution ($\sim$300 fs) as compared to the gas phase ($<$100 fs) or the life time of the $n\pi^*$ state decreases in water ($\sim$300 fs) relative to the gas phase ($\sim$1 ps). In the second scenario, the order of the excited states is exchanged. The $n\pi^*$ state is then energetically higher than the light-absorbing $\pi\pi^*$ state and does not play a role in the relaxation process. Considering the absence of fluorescence, we must then assume a direct coupling of the $\pi\pi^*$ state to the ground state, possibly via conical intersections.

As in the gas phase, the $\pi\sigma^*$ state may also play a role in photophysics of solvated adenine, shortening the excited state life times. The gas phase calculations [41, 43] predicted a large stabilization of the $\pi\sigma^*$ state in polarizable environments. At the same time, the excitation of this state would require a rearrangement of the surrounding solvent molecules to accommodate the large dipole moment of this state. The latter may make the $\pi\sigma^*$ state energetically unfavorable. Since the theoretical investigations of the $\pi\sigma^*$ states in the condensed phase is difficult, the focus returned to experimental work to prove or disprove the existence of the $\pi\sigma^*$ state in solvated adenine. Pancur et al. [61] applied time-resolved fluorescence up-conversion spectroscopy. The authors investigated the excited state dynamics upon excitation with a wavelength between 280 nm and 245 nm. They observed a decrease of the excited state life time with shorter excitation wavelengths and suggested the existence of an additional radiationless relaxation pathway via the $\pi\sigma^*$ state at about λ_{ex}=245 nm (5.06 eV). This statement will be discussed in the light of our own experimental results for microsolvated adenine (sec. 5), where we will show that a few water molecules are enough to dramatically change the ES dynamics, possibly by stabilizing the $\pi\sigma^*$ state.

4.1.2 Time-resolved and electron-ion coincidence experiments in excited adenine

In our experiments, the excited states of adenine were characterized with coincidence electron spectroscopy and the life times of these states were determined with time-resolved mass spectroscopy. Fig. 4.4 shows a coincidence electron spectrum of adenine monomer at a delay time $\Delta t = 0$ between the pump and the probe pulses. In these

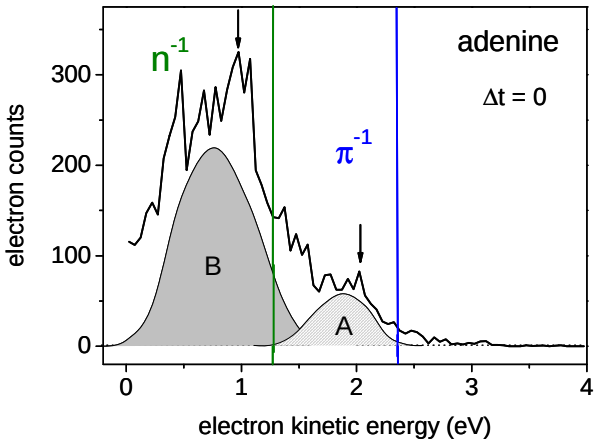

Figure 4.4: Photoelectron spectrum of adenine at a pump-probe delay time $\Delta t = 0$. The two bands A and B, observed in the spectrum are due to ionization of the $\pi\pi^*$ state into the π^{-1} ionic state and $n\pi^*$ state into the n^{-1} ionic state. The gaussian-like shapes for the bands are shown ti guide the eye (not fits). The lines show the electron kinetic energies corresponding to the literature values for the vertical ionization potentials IP_v: 8.48 eV (π^{-1}) and 9.58 eV (n^{-1}). The arrows show the experimentally obtained values IP_v^{exp} = 8.85 eV and 9.89 eV in our pump-probe experiments.

experiments, adenine was photoexcited with 267 nm and ionized with 400 nm pulses. Two electronic bands were observed in the spectrum: band A at higher electron kinetic energies, and band B in the low energy spectral range. For bands A and B, we determined respective vertical ionization potentials IP_v^{exp} = 8.85 eV and 9.89 eV, using Eq. (2.13). The electron kinetic energies that correspond to these values are 2.0 eV and 0.96 eV and are indicated by arrows in fig. 4.4. Our observed vertical ionization potentials IP_v^{exp} were higher than the values for ground state ionization in the literature, 8.48 eV (D_0) and 9.58 eV (D_1) [63]. The electron kinetic energies that

correspond to these values are shown as vertical lines at 2.37 eV and 1.27 eV. The shift towards higher energies between our measured IP_v^{exp} and the literature values could be due to the excess vibrational energy in the excited state, which is transferred to the ionic state according to Frank-Condon probabilities.

We assigned the bands A and B using Koopmans' theorem [4, 64]. According to this theorem, the S_2 ($\pi\pi^*$) state can be only ionized into the D_0 (π^{-1}) state, and the S_1 ($n\pi^*$) state - into the D_1 (n^{-1}) state. Based on the literature values for the ionization potentials, the band A in the spectrum was assigned to the ionization of $\pi\pi^*$ excited state into the π^{-1} ionic state. The second band B was assigned to the ionization of $n\pi^*$ state into the n^{-1} ionic state. Although, the spectrum in fig. 4.4 was measured at a delay time Δt = 0, both excited states were observed. This indicates that the pump-probe cross-correlation time is comparable with the internal conversion (IC) time from the $\pi\pi^*$ to the $n\pi^*$ state.

To determine the life times of the two excited states, we carried out time-resolved measurements with ion detection. The delay between the pump and the probe pulses was varied in steps of 50 fs (fig. 4.5) and the integrated signal in the A mass channel was plotted against the pump-probe delay. The experimental data were fit with a double-exponential decay. The fast decay component (τ_1 = 80 fs) was assigned to the relaxation of the optically bright $\pi\pi^*$ state, which is populated from the GS by one photon absorption. The second decay component with a life time of τ_2 = 1.3 ps was assigned to the relaxation of the $n\pi^*$ state. The mass-spectrum in the insert of fig. 4.5 shows the cluster distribution in the experiment. Only a small amount of the dimer and no other bigger clusters were observed in the spectrum, therefore fragmentation is expected to be negligible. Toluene was added for calibration purposes. The mass 108 is a fragmentation product of adenine (-HCN loss).

We conclude, that our experimental results for isolated adenine agree with one of the theoretically predicted excited state relaxation pathways: $\pi\pi^*(L_b) \rightarrow n\pi^* \rightarrow S_0$ and other experimental data [31, 51, 53, 54]. Two bands in the electron coincidence spectrum were assigned to the low-lying $\pi\pi^*$ and $n\pi^*$ excited states based on their ionization potentials. The life times of these states were determined as 80 fs for the $\pi\pi^*$ state and 1.3 ps for the $n\pi^*$ state. Other electronic states, such as $\pi\sigma^*$ state, were not observed in our experiments.

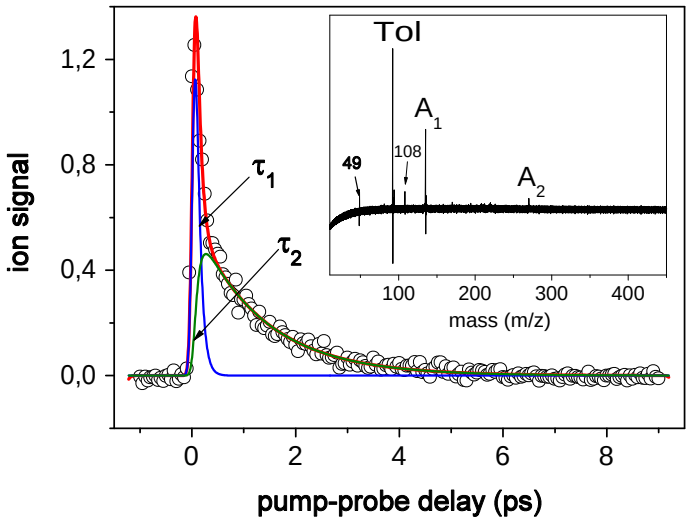

Figure 4.5: Time-dependent ion signal and mass spectrum of isolated adenine. Experimental points (circles) were fit with a double-exponential decay with $\tau_1 = 80$ fs and $\tau_2 = 1.3$ ps. The fs decay is due to the relaxation of the $\pi\pi^*$ state and the ps decay characterizes the relaxation of the $n\pi^*$ state. The insert shows a mass spectrum with the cluster distribution in the experiment. Besides adenine monomer, a small amount of adenine dimer (did not affect the monomer dynamics), toluene (calibration compounds), and fragments (m/z=49, 108) were observed.

4.1.3 Thymine: literature overview of experiments and theory

The molecular structure of thymine is shown in fig. 4.6. Thymine belongs to the molecular class of pyrimidines and contains one aromatic ring. In the natural DNA double helix, the N3 and C4 atoms are H-bound to adenine, and a sugar-phosphate group is attached at the N1 position. Upon UV excitation we can expect low-lying excited states of $\pi\pi^*$, $n\pi^*$ and $\pi\sigma^*$ characters.

The position of the first singlet excited state in thymine at around 290 nm [66, 67] was determined in early works with absorption spectroscopy. Similar to adenine, a low fluorescence quantum yield, on the order of $\sim 10^{-4}$ was measured [39, 66]. In contrast to the fluorescence quantum yield, the phosphorescence quantum yield was found to be relatively high ($1.6 \cdot 10^{-2}$) [67]. A first investigation of the excited state life time was carried out in the group of Nikogosyan [68] with the picosecond tran-

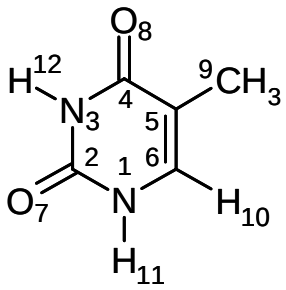

Figure 4.6: Molecular structure of thymine. Numbering of the atoms according to ref. [65].

sient absorption technique. Using an excitation wavelength of 264 nm, Nikogosyan measured an excited state life time for solvated thymine of 4±2 ps. Later, the same authors carried out femtosecond transient absorption measurements [69], and found a life time of the excited state of 1.2 ps with an excitation wavelength of 282 nm. It should be mentioned here, that a transient absorption method can be problematic to determine short excited state life times, if those times are comparable with the experimental time resolution. Nonlinear absorption of solvent will be the dominant contribution at high laser energies. Further experimental work to investigate the thymine dynamics was performed in the group of Gustavsson [70], using 267 nm for excitation and fluorescence up-conversion as detection method. They found a double-exponential excited state decay of solvated thymine with the time constants τ_1= 150 fs and τ_2= 580 fs. The assignment of these time constants, however, was not unambiguous. The time constant τ_1 was tentatively attributed to the decay of the bright fluorescent state, and the authors suggested that the second component τ_2 could be related to the interaction with the solvent.

There were a number of experimental studies of thymine in the gas phase in the recent years. Brady et al. [71] measured the first frequency-resolved spectrum of isolated thymine and identified a broad band with an onset at around 36300 cm^{-1} (275 nm). No sharp absorption lines were found. This was attributed to either a mixing of electronic states or to a large geometry change between the ground and excited electronic states. In time-resolved measurements of isolated thymine, a two-exponential excited state decay [49, 51, 72, 73] was measured. Time constants of 50-130 fs (τ_1) and 5-8 ps (τ_2) were observed in the measurements and were assigned to the relaxation of different excited states of thymine. This assignment was based on results from electron spectroscopy [72] and also on theoretical predictions, which will be

discussed in the next paragraph. Electron spectra [72], measured with excitation and ionization wavelengths of 250 and 200 nm showed two electronic bands. The ionization potentials for these bands were in a good agreement with the literature values [63] for the $\pi\pi^*$ and $n\pi^*$ excited states. Additionally, a long relaxation component was found in time-resolved experiments by Gador et al. [56] and Samoylova et al. [52]. The life time of this component was not characterized exactly, due to a limited scanning interval in their experiments, but was estimated as >1 ns. These results [52, 56] are in agreement with results obtained with nanosecond spectroscopy of thymine in the gas phase [74]. The latter authors measured an excited state decay with a 22 ns life time. The character of the electronic state with ns life time remains unclear. Dark $n\pi^*$ state or a triplet state were suggested [74].

A number of theoretical calculations investigated the excited states of thymine. Most of these calculations were performed for isolated thymine. Vertical excitation energies were obtained by Lorentzon et al. [75][1], Shukla et al. [76][2], and Perun et al. [77][3]. In all cases, two low excited states of $n\pi^*$ and $\pi\pi^*$ character were found. Adiabatic energies were only presented in the work of Perun et al. [77]. It was found that the order of the excited states in the relaxed geometry stays the same as in the geometry of vertical excitation: the $n\pi^*$ is the lowest excited state and the $\pi\pi^*$ is located more than 0.5 eV higher in energy. Conical intersections between the excited states and the ground state were also studied. Fig. 4.7 shows the PES for the ground state and three low energy excited states calculated as a function of three different reaction coordinates.

The lowest energy conical intersections (CI 1, CI 2) leading to the electronic ground state were found along a reaction coordinate, involving the bending of the methyl-group out of the plane of the aromatic ring. The conical intersections CI 1 and CI 2 are accessible with almost no barrier from the $\pi\pi^*$ state minimum and may therefore explain the structureless spectrum [71]. The other two conical intersections, CI 3 and CI 4, are higher in energy and presumably not relevant for the radiationless decay of the lowest excited states [77]. However, the higher CIs may play a role when thymine is excited with larger excess energy. Based on these results, Perun et al.

[1] CASPT2 method (second-order perturbation theory based on the complete-active space self-consistent-field (CASSCF) reference)

[2] single-excitation configuration (CIS) method

[3] CC2 (approximated singles and doubles coupled-clusters) method based on the CASSCF reference

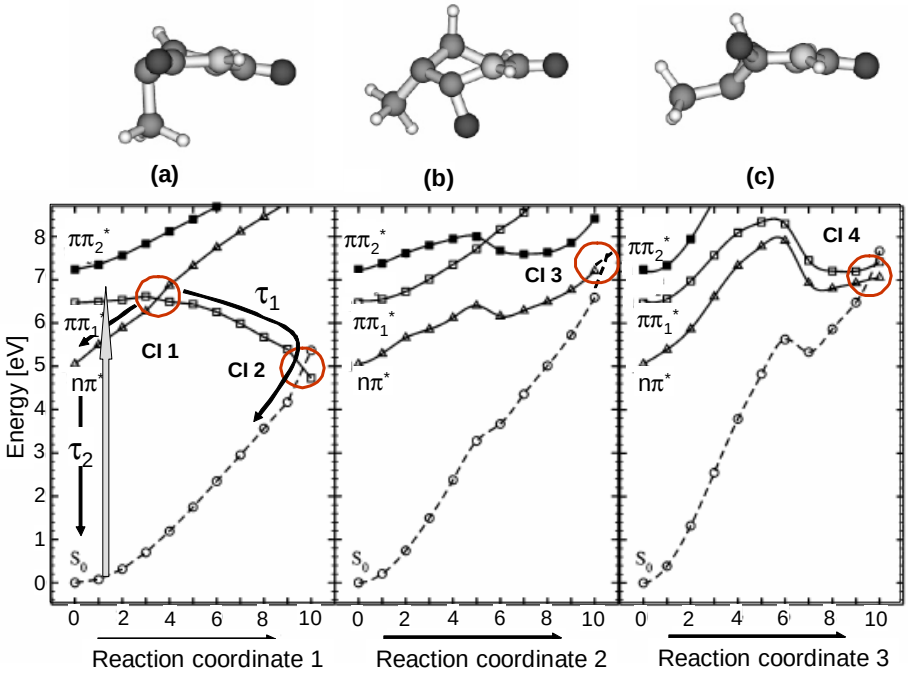

Figure 4.7: Calculated potential energy surfaces for the ground state and three low excited states in thymine (reproduced from ref. [77]) as a function of different reaction coordinates. Structures corresponding to the conical intersections are shown above. Circles show conical intersections between the states. The relaxation coordinate (a) represents the most probable relaxation pathway, with the low-lying conical intersections CI 1 and CI 2. A thick arrow in (a) shows the excitation process, thin arrows indicate possible relaxation pathways to the ground state (τ_1, τ_2). For the reaction coordinates shown in (b) and (c), conical intersections of the lowest-lying excited states with the ground states (CI 3 and CI 4) were also identified. However, these CIs are located higher in energy and may not be relevant for the excited state dynamics of thymine.

suggested that the fs transient τ_1 observed in the experiments can be interpreted as the decay of the $\pi\pi^*$ excited state through the CI 1 and CI 2 conical intersections, while the longer-lived transient τ_2 of several ps may reflect the decay of the $n\pi^*$ state.

An alternative model for the excited state decay in thymine has been presented in the theoretical work of Hudock et al. [78] who used the *ab initio* multiple spawning (AIMS) method to simulate the excited state dynamics. According to their calculations, the result of which is shown in fig. 4.8, the fs transient (τ_1) is due to relaxation from the vertical to the adiabatic minimum in the $\pi\pi^*$ state. Internal conversion between the $\pi\pi^*$ and the $n\pi^*$ states was suggested to take place on the ps (τ_2) time scale. The ns component (τ_3) measured by He et al. [74] could then correspond to

the life time of the $n\pi^*$ state [78].

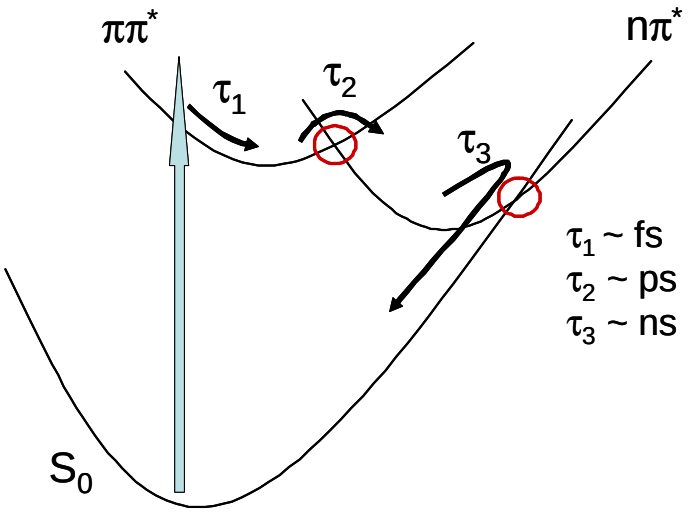

Figure 4.8: Excited state relaxation of thymine, according to Hudock et al. Circles mark conical intersections, thick and thin arrows show excitation process and relaxation pathways with time constants τ_1, τ_2, and τ_3. [78].

To explain the excited state dynamics of thymine in the liquid phase [59], a first theoretical explanation was given by Gustavsson et al. [79]. Absorption energies were calculated for thymine in water environment, which was simulated as a polarizable continuum (PC) or as PC with four explicit waters. Both models gave very similar results: the $\pi\pi^*$ state was found to be the lowest excited state and the $n\pi^*$ state was located 0.17 - 0.3 eV above the $\pi\pi^*$ state, depending on the model used. A conical intersection between the $\pi\pi^*$ excited state and the ground state was found along a reaction coordinate involving the out-of-plane motion of the amino group on the C5 atom and may be responsible for fast excited state relaxation. The theoretical results explain only one component of the double-exponential decay of solvated thymine [70]: the authors assigned the <200 fs decay time to the passage from the $\pi\pi^*$ minimum to the electronic ground state through the mentioned conical intersection, because only a small barrier was calculated for this process. The origin of the second component with a life time of ∼600 fs still remains unclear. Possibly, it can be due to other thymine tautomers, whose presence in the liquid phase was reported [80].

4.1.4 Time-resolved and electron-ion coincidence experiments in excited thymine

To determine the electronic character and life times of the excited states of thymine in the gas phase, we carried out electron-ion coincidence spectroscopy and time-resolved mass spectroscopy. We also initiated efforts to characterize the excited states by *ab initio* calculation in collaboration with Prof. L. González and Dr. J. González-Vázquez (Friedrich-Schiller-Universität, Jena).

An electron spectrum of thymine is presented in fig. 4.9. The spectrum was taken at a delay $\Delta t = 0$ between the excitation and ionization pulses of 267 nm and 400 nm. Two electron bands A and B were observed in the spectrum. Band A is formed by electrons with kinetic energies in the range of 0.82 eV to 1.67 eV. Band B is due to electrons with kinetic energies below 0.82 eV. Experimentally observed vertical ionization potentials of $IP_v^{exp} = 9.49$ eV for band A and 10.08 eV for band B were determined using Eq. (2.13). The electron kinetic energies that correspond to these IPs are 1.36 eV and 0.77 eV and are shown with vertical arrows in fig. 4.9. The observed vertical ionization potentials were higher than the corresponding values for ground state ionization in literature (9.18 eV and 10.03 eV [81]). Vertical lines in fig. 4.9 show electron kinetic energies corresponding to the literature ionization potentials (1.67 eV and 0.82 eV). The shift towards higher energies between the expected literature and measured values can be explained with the vibrational excess energy in the excited states, which is transferred to the ionic states according to Franck-Condon probabilities.

The assignment of the electron bands in the spectrum is based on Koopmans' theorem [4, 64]. The determined vertical ionization potentials allowed an assignment of band A to the $\pi\pi^* \rightarrow \pi^{-1}$ and of band B to the $n\pi^* \rightarrow n^{-1}$ ionization channel. The appearance of both bands in the spectrum at zero time delay between pump and probe pulses has the same explanation, as in the case of adenine. The higher excited $\pi\pi^*$ state internally converts into the lower $n\pi^*$ state within the pulse duration of the pump and the probe pulses.

To observe the population dynamics in the excited states, we scanned the delay between pump and probe pulses in the range of 0 to 220 ps. To determine the excited state life times accurately, the dynamics was investigated in three different time intervals. Fig. 4.10 shows the thymine dynamics on the short (up to 4.5 ps) and intermediate time intervals (up to 45 ps).

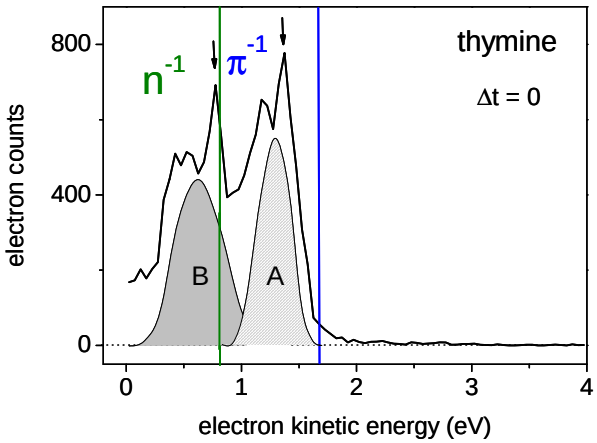

Figure 4.9: Photoelectron spectrum of thymine at a delay time $\Delta t = 0$. The two bands A and B are due to ionization of the $\pi\pi^*$ state into the π^{-1} ionic state and the $n\pi^*$ state into the n^{-1} ionic state. The gaussian-like shapes for the bands are shown ti guide the eye (not fits). The lines show the expected values for the electron kinetic energies, based on the literature values $IP_v = 9.18$ eV (π^{-1}) and 10.03 eV (n^{-1}). The arrows indicate the experimentally observed values of 9.48 eV and 10.08 eV.

In graph (a), the excited state decay was fit with the sum of three exponential decays. The two major decay components had life times $\tau_1 = 100$ fs and $\tau_2 = 7$ ps. They were assigned to the relaxation of $\pi\pi^*$ and $n\pi^*$ states [49]. A third component had to be included to account for a long-lived signal in the decay trace for longer delays. In graph (b) we observe that the decay components τ_1 and τ_2 vanish within 20 ps. But a long-lived signal with the life time τ_3 >1 ns remains. We attributed this component to a long-lived state described in the literature of the ns pump-probe experiments [74]. The mass spectra corresponding to the decay traces are shown on the right-hand side. They are rather complex and show multiple fragments and signals of calibration compounds. All peaks, except of thymine monomer (T_1) and thymine dimer (T_2), are explained in table 4.1. Small amounts of T_2 in the mass spectrum for (a) could lead to fragmentation of the dimer into monomers, whereas cluster fragmentation is not expected for the case (b), because T_2 was not observed.

On the time scale of our measurements (200 ps), the ns trace remains constant (fig. 4.11) and we could not determine the exact life time due to limited size of our translation stage. The amplitude of the ns component is very small in all traces

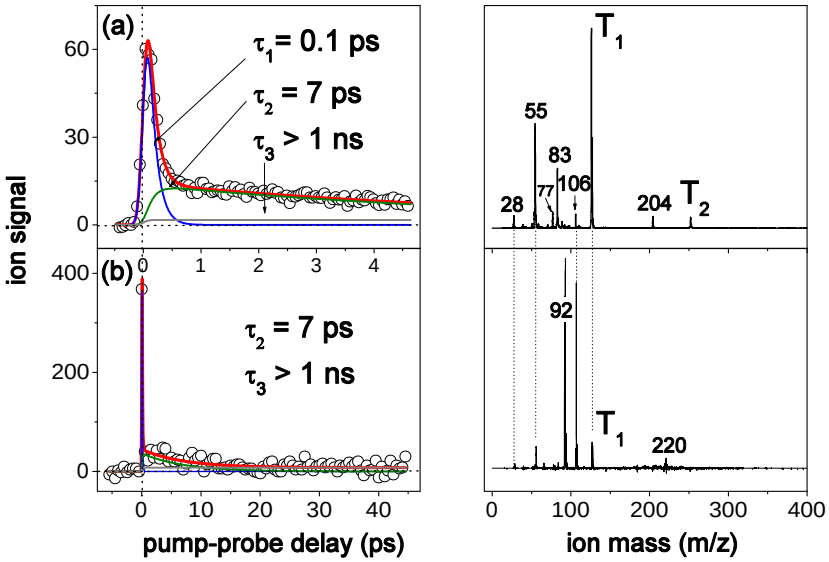

Figure 4.10: Time-dependent ion signal of isolated thymine measured for a short and an intermediate time interval at a pump wavelength of 267 nm and a probe wavelength of 800 nm (a) or 400 nm (b). The experimental points (circles) were fitted with the sum of three exponential decays, $\tau_1 = 100$ fs, $\tau_2 = 7$ ps, and $\tau_3 > 1$ ns. The time constants were assigned to the relaxation of the $\pi\pi^*$, $n\pi^*$ and a dark state, the character of which is, so far, unknown. The cluster distribution in the experiments is shown on the right-hand-side. For assignment of mass signals see table 4.1.

(fig. 4.10 and 4.11). The origin of this component is so far unknown. We attempted to characterize the ns component by electron-ion coincidence spectroscopy, but due to a small signal size we were not able to measure enough signal to characterize the spectrum.

In collaboration with the group of Prof. Leticia González (Friedrich-Schiller-Universität, Jena), we tried to assign the excited states with *ab initio* calculations. This work was done inside the Collaborative Research Center SFB-450 – Analysis and control of ultrafast photoinduced reactions. It was already shown in literature [80, 82, 83], that DNA bases can have several tautomers in the ground state. We investigated the possibility that different T tautomers could be responsible for the three observed transient states. Tautomerization could lead to several ground state structures in the molecular beam, or could occur in the excited state. The ground state

Table 4.1: Assignment of the mass signals in the spectra in fig. 4.10 and 4.11.

mass	compound
126, 252	thymine monomer and thymine dimer
28, 55, 83	covalent fragments of thymine
92, 106, 204	toluene, xylene, iodobenzene - added for calibration purposes
77	covalent fragment of iodobenzene
220	impurity in the chamber

geometries were optimized without any symmetry constraint using the MP2[4] method with a doubly polarized (cc-pVDZ) basis set in the Gaussian 03 program. Vertical excitation energies of all structures were calculated using the RI-CC2[5] method (see also Appendix B). To describe $\pi\sigma^*$ states properly, the Dunning basis set aug-cc-PVTZ with triple polarization and augmented with diffuse functions was employed using the TURBOMOLE software package.

Fig. 4.12 shows six low-energy tautomers of thymine. The *ab initio* calculations found the canonical (biologically relevant) structure T1 to be the most stable tautomer. The other tautomers were found to be less stable by 9.8-23.3 kcal/mol. The results of these calculations agreed well with previously reported data for the stability of thymine tautomers in the literature [80, 82, 83]. The tautomers T2-T6 were formed by migration of one (T2, T3, T5) or two (T6, T4) hydrogens from the N-atoms to the O-atoms. We estimated the propensities of the tautomers for a wide range of temperatures based on the Boltzmann distribution to determine the relevant tautomer populations in the ground state. The temperature of 50 K was estimated to be the temperature of the molecular beam. The temperature of 500 K is the temperature of the oven and valve in our cluster experiments. Table 4.2 shows the resulting populations calculated for the lowest (50 K) and the highest (500 K) temperatures. It was found that the canonical form (T1) is the most populated tautomer at all temperatures. The relative population of T2, T3, T4, T5, and T6 tautomers, even at 500 K, was found to be negligible.

[4]second-order Møller-Plesset

[5]Resolution of the Identity coupled-cluster of second order

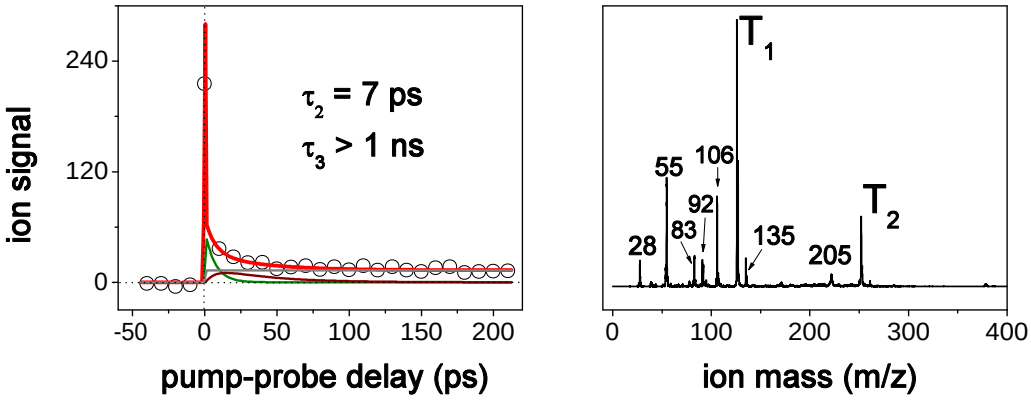

Figure 4.11: Time-dependent ion signal of thymine at a pump wavelength of 267 nm and a probe wavelength of 400 nm measured for a long time interval. The corresponding mass spectrum is shown on the right-hand-side and the assignment of the masses is given in table 4.1.

Table 4.2: Population of thymine tautomers [84] at 50 K and 500 K (in %).

T, K	T1	T2	T3	T4	T5	T6
50	100.00000	0.00000	0.00000	0.00000	0.00000	0.00000
500	99.99223	0.00539	0.00000	0.00212	0.00025	0.00000

For all tautomers, the vertical excitation energies were also calculated and shown in fig. 4.13. For the T2, T3, and T5 tautomers we also calculated the transition state energies. The transition state energy barriers for tautomerization were found to be about 2 eV above the energy of the T1 form. Such high barriers can not be overcome within the experimental conditions in the molecular beam. Therefore, we expect only the canonical form T1 to be present in the molecular beam and to be excited with the laser. Transition states were not calculated for the T4 and T6 forms, because these tautomers are formed by multiple hydrogen migrations. The barriers for these processes are expected to be higher than for migration of one hydrogen atom between neighboring atoms [6].

We also considered tautomerization in the excited state. The lowest excited states

[6] private communication with Leticia González and Jesus González-Vázquez

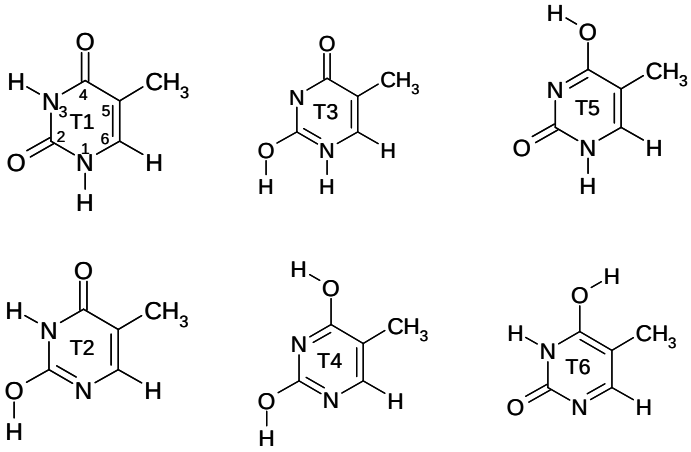

Figure 4.12: The canonical form of thymine (T1) and five other tautomers formed by H-migration (T2-T6).

of $\pi\pi^*$ and $n\pi^*$ character for all tautomers are presented in fig. 4.13. The energies of the optically bright $\pi\pi^*$ states are similar for all tautomers. According to the calculations, the excitation energy of the $\pi\pi^*$ state in the T1 tautomer (5.17 eV above the canonical ground state, fig. 4.13) is comparable with the excitation energy of the $\pi\pi^*$ state in T5 tautomer (5.06 eV above the canonical ground state, fig. 4.13). The $\pi\pi^*$ state energies for the other tautomers (except of T3) are only slightly higher, but these tautomers may still be accessible. However, the calculated tautomerization barriers of $\sim$1.5 eV are too high to allow tautomerization in the $\pi\pi^*$ excited state.

Tautomerization can also occur in the $n\pi^*$ state, which is non-adiabatically populated from the $\pi\pi^*$ state [31, 51, 52, 72]. But the $n\pi^*$ state of the T1 tautomer has a lower energy then the corresponding state in all other tautomers, and we can exclude therefore the tautomerization in the $n\pi^*$ state.

We also calculated the energies for the $\pi\sigma^*$ states in all thymine tautomers (not shown in fig. 4.13, see [84]). The lowest $\pi\sigma^*$ state was found for the T1 tautomer at 5.71 eV above the ground state energy. For the other tautomers, $\pi\sigma^*$ states were found to be higher in energy. Based on these results we do not expect $\pi\sigma^*$ states to be involved in the thymine relaxation upon excitation with 267 nm.

The calculations showed that neither tautomerization in the ground state, nor tautomerization in the excited states can explain the complex excited state dynamics of thymine. No evidence that $\pi\sigma^*$ states are relevant for thymine relaxation was found by the calculations as well. Therefore, the measured triple-exponential decay

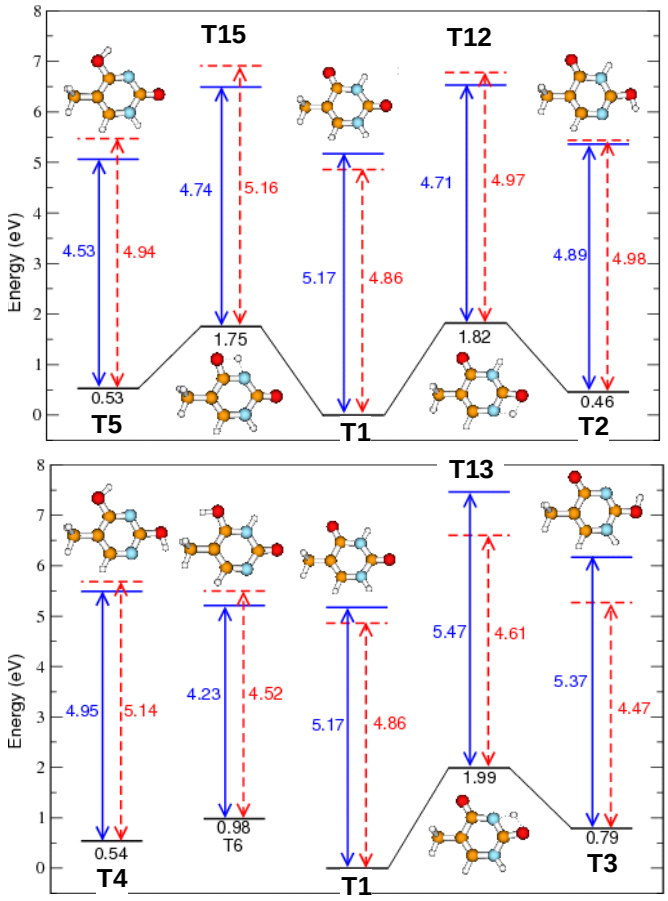

Figure 4.13: Ground state and vertical excitation energies for all expected thymine tautomers (T1-T6) and transition states between them. The solid and dashed lines depict the $\pi\pi^*$ and $n\pi^*$ states, respectively. Arrows show vertical transition energies in eV from the optimized ground state structures to the $\pi\pi^*$ and $n\pi^*$ states. All energy levels are given with respect to the lowest energy tautomer T1.

of thymine must be assign tentatively based on literature. One possible excited state relaxation model was described in the work of Hudock et al. [78], who identified a local minimum on the $\pi\pi^*$ PES. The fs relaxation with a life time τ_1 was assigned to vibrational energy redistribution within the photoexcited $\pi\pi^*$ state. The relaxation of the $\pi\pi^*$ state to the lower-lying $n\pi^*$ state was predicted to occur on the picosecond time scale and can explain the observed decay component with life time $\tau_2 = 7$ ps. The ns component (τ_3) was suggested by Hudock et al. to be the life time of the $n\pi^*$ state. However, the existence of the local minimum on the $\pi\pi^*$ state PES was

disputed [7]. Another possible model, described by Sobolewski and Domcke, is based on the fact that the $\pi\pi^*$ state may be strongly coupled to the $n\pi^*$ state [77, 85]. The fs component then reflects the population transfer from the $\pi\pi^*$ to the $n\pi^*$ state. The $n\pi^*$ state might decay to the ground state or to lower-lying triplet states [86] on the ps time scale. The ns component would then be due to the life time of the triplet states. Our experimentally measured data for thymine are in better agreement with the model offered by Sobolewski and Domcke, because we observed two bands in the electronic spectrum of T (fig. 4.9), assigned to the $\pi\pi^*$ and $n\pi^*$ states. Appearance of both bands at the delay $\Delta t = 0$ indicates that the $n\pi^*$ state is populated within ~100 fs. This contradicts the model of Hudock et al. To check the hypothesis of low-lying triplet states with a ns life time in T, further investigation by *ab initio* theory and photoelectron spectroscopy is in progress.

4.2 Adenine and thymine clusters

In this chapter we present our results for A and T dimers obtained with coincidence electron spectroscopy and time-resolved mass spectroscopy. We tried to address the question whether intramolecular or intermolecular processes dominate the excited state relaxation in the clusters. One such intermolecular process - a charge-transfer reaction in A-T base pair - was predicted by theory [87]. This reaction may play a crucial role in the photophysics of DNA base pairs and distinguish those from single DNA bases.

4.2.1 Photophysics of A_2, T_2, and A-T clusters

The excited states in **adenine dimer** were studied by one color resonant two photon ionization (R2PI) spectroscopy using ns laser pulses [88]. The origin of the first excited $\pi\pi^*$ state was found at 35040 cm^{-1} (285 nm). The significant shift of 1065 cm^{-1} relative to adenine monomer (36105 cm^{-1}) was explained by a large stabilization of the $\pi\pi^*$ state in the cluster. The authors also observed AH radicals after $\pi\pi^*$ state excitation of the dimer and attributed this to a H-transfer reaction in A_2 followed by fragmentation. The H-transfer reaction may be induced by a charge-transfer between the monomers in the excited state followed by a proton-transfer [88]. The same

[7] oral communication with L. Blancafort

reaction was found and investigated in the base pair model system 2-aminopyridine dimer [7, 26, 89]. This relaxation mechanism was proposed to play a crucial role to explain the photostability of DNA [22, 87].

The excited state properties of **thymine dimer** drew a lot of interest because adjacent thymine bases can form cyclobutane pyrimidine dimers (CPD) upon UV irradiation. CPD is formed by a [2+2] photocycloaddition reaction in which the carbon-carbon double bonds of proximal pyrimidine bases react to form a cyclobutane ring (fig. 4.14). The CPD photoproduct is a major reason for DNA damage after exposure to UV radiation.

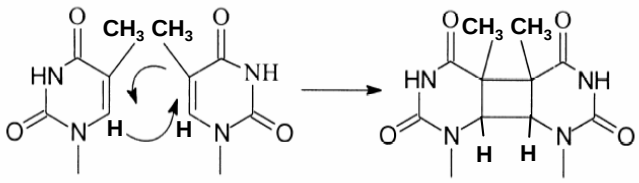

Figure 4.14: Formation of a cyclobutane pyrimidine dimer (CPD).

Thymine dimerization in the gas phase was first discussed by Kim et al. [90, 91]. Using the nanosecond R2PI method, the authors observed a strong intensity alternation between even and odd clusters in their mass spectra. A cluster ion consisting of an even number of molecules predominantly fragmented by losing two molecules, while a cluster consisting of an odd number of molecules predominantly lost one molecule. This behavior was attributed to the formation of CPD based on the fact that a CPD is stronger bound (by covalent bonds) than molecules in a cluster (by hydrogen bonds). The even-odd alternation was only observed at wavelengths between 210 and 280 nm, using high-intensity ns laser pulses. Kim et al. concluded that excitation of the two lowest electronically excited states is necessary to trigger the formation of CPD. A time-resolved study of the photodimerization reaction in thymine oligodeoxynucleotide $(dT)_{18}$ in liquid phase was reported by Schreier et al. [92]. With fs time-resolved infrared spectroscopy, it was shown that complete formation of cyclobutane dimers happens within 1 ps after the excitation to the lowest $\pi\pi^*$ state.

We tried to observe the gas phase dimerization reaction in thymine in the time domain. Using a ns laser with the wavelength of 266 nm, we could reproduce the experiment described by Kim et al. [90, 91]. However, the even-odd intensity alter-

nation in thymine clusters observed by Kim can also be explained by non-covalent bonding (interaction in the cationic clusters). We suggest that if efficient and rapid dimerization takes place in the excited state, it should be possible to observe the corresponding reaction in fs time-resolved spectroscopy of thymine clusters and performed experiments to identify such a reaction.

In biological double-stranded DNA, A and T from the opposing strands form specific hydrogen bonds in the WC **A-T** base pair. It is therefore desirable to understand the photoinduced processes in the WC base pairs of A and T. *Ab initio* theory predicted a hydrogen-transfer reaction for the WC cluster of A-T in the gas phase. The H-transfer might provide a very efficient excited state quenching mechanism, leading to a high photostability of the A-T base pair [87].

The excited states in A-T cluster were investigated by theory [87]. Fig. 4.15 shows potential-energy profiles for the ground state and low-lying excited states calculated with the CC2 (approximated singles and doubles coupled clusters) method.

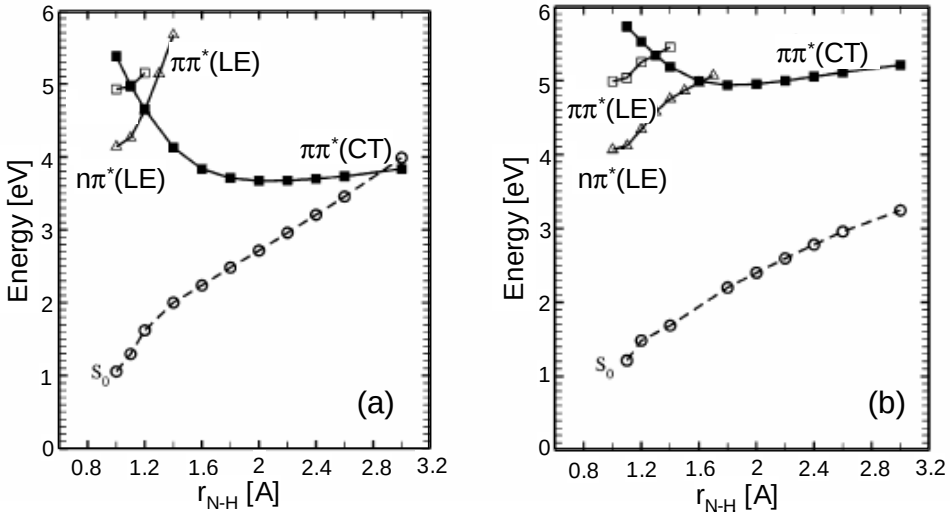

Figure 4.15: Calculated potential energy profiles of the ground state and the lowest $n\pi^*$, $\pi\pi^*$, and $\pi\pi^*$ (CT) excited states along the H-transfer coordinate r_{N-H} for the WC conformer (a) and the most stable conformer MS (b) in molecular beam conditions (reproduced from ref. [87]).

The calculations investigated three low-lying electronic states of $n\pi^*$, $\pi\pi^*$, $\pi\pi^*$ (CT) character, for the WC conformer and for the most stable conformer expected in molecular beam experiments [88]. The CT state did not exist in isolated bases.

This state is formed upon excitation of an electron from the HOMO [8] π orbital of A to the LUMO [9] π^* orbital of T. The vertical excitation energy for the CT state in the WC conformer was calculated to be quite high (6.26 eV), but the state is substantially lowered in energy by the transfer of a proton and its adiabatic energy of 3.7 eV is below the adiabatic energy of the $\pi\pi^*$ and $n\pi^*$ state (fig. 4.15a). The authors also identified a sequence of conical intersections which connect the optically bright $\pi\pi^*$ state with the ground state. The conical intersections may allow a very fast deactivation of the potentially reactive excited states in the WC conformer. In agreement with theoretical prediction, R2PI experiments [88] found that the WC structure is not the most stable isomer under molecular beam conditions. Therefore, the CT reaction coordinate was also calculated for the most stable isomer found experimentally (fig. 4.15b). Similar excitation energies were found for the $n\pi^*$ and $\pi\pi^*$ states. But the CT state was located energetically higher then in the WC isomer and did not cross the electronic ground state. The lack of a low-lying CI with the GS may result in longer life times for all excited states of the MS conformer and therefore lead to higher photochemical reactivity. Thus, the theoretical results support the idea that the WC base pairs may have a unique and efficient excited state deactivation mechanism which minimizes the danger of photochemical reactions.

4.2.2 Experimental results

The discussion of the experimental results will cover homo- and heteroclusters of adenine and thymine. The data analysis requires, however, a detailed understanding of fragmentation pathways in the clusters, which are described first.

Cluster fragmentation.

A typical mass spectrum containing A and T clusters is shown in fig. 4.16. Mass signals of the base monomers A (m/z = 135), T (m/z = 126) and dimers T_2 (m/z = 252), A-T (m/z = 261), A_2 (m/z = 270) are clearly visible. Bigger clusters were avoided as far as possible by choice of the molecular beam expansion conditions. The insert shows a magnified spectral interval at the position of the base monomers and allows the assignment of protonated monomer signals AH and TH with m/z = 136

[8] HOMO - highest occupied molecular orbital

[9] LUMO - lowest unoccupied molecular orbital

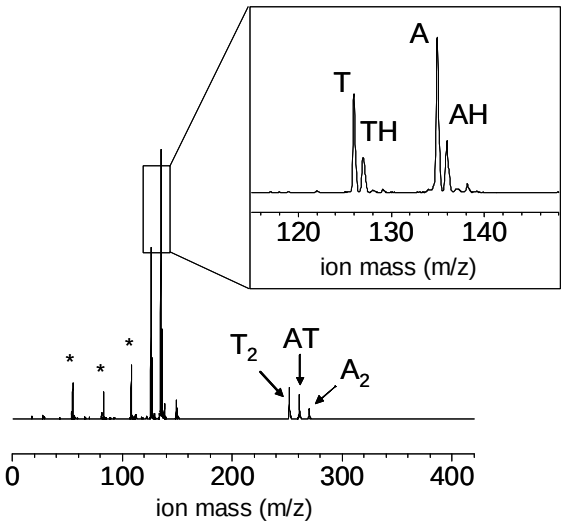

Figure 4.16: Mass spectrum of A (m/z = 135), T (m/z = 126) and their clusters, measured with the excitation wavelength of 267 nm and ionization wavelength of 800 nm. Protonated monomers are shown in the inset. Asterisks mark covalent fragments of A (m/z = 108) and T (m/z = 55, 83).

and m/z = 127, respectively. By varying the width of the cluster distribution, we found that the amplitudes of the AH and TH signals were proportional to the dimer amplitudes and were therefore fragmentation products of the dimers. No significant change in the amplitudes of A and T mass channels was observed upon varying the cluster distribution. In absence of clusters, signals at m/z = 136 and m/z = 127 had an amplitude of ∼6 % of the monomer amplitudes due to the natural abundance of ^{13}C and ^{2}D isotopes. Detection of a significant amount of protonated monomers in the presence of dimers indicates dissociation after proton or H-transfer in the course of the experiment. In the collision-free environment of a molecular beam, the only source of a proton is a neighboring base in the cluster. Fragmentation can occur before ionization in the neutral excited state or after ionization. These two types of fragmentation channels were discussed for the case of 2-aminopyridine clusters in subsec. 3.3.1. For 2-AP clusters we observed that neutral fragmentation changes the excited state dynamics significantly. For A and T clusters, we observed no indications for neutral fragmentation in the time-resolved ion signals (see fig. 4.18 - fig. 4.24) and we assume that fragmentation occurs predominantly in the ions. Both, A and T chromophore can be excited/ionized and we must consider different fragmentation pathways following the excitation and ionization of either chromophore in the cluster.

The four possible proton-transfer reactions in the base dimers are

$$A_2^{\bullet+} \longrightarrow AH^+ + A^{\bullet}(-H) + Q \tag{4.2}$$

$$T_2^{\bullet+} \longrightarrow TH^+ + T^{\bullet}(-H) + Q \tag{4.3}$$

$$AT^{\bullet+} \longrightarrow AH^+ + T^{\bullet}(-H) + Q \tag{4.4}$$

$$TA^{\bullet+} \longrightarrow TH^+ + A^{\bullet}(-H) - Q. \tag{4.5}$$

The ionized base chromophore is a radical cation, while the second base in the cluster stays neutral ground state molecule. Based on the acidity of the radical cation and the proton affinity of the neutral, we can estimate if a proton-transfer reaction will take place (exothermic reaction) or not (endothermic reaction). In adenine dimer, the measured acidity of the A radical cation ($A^{\bullet+}$) is 221 kcal/mol (9.58 eV) [93] and the proton affinity of A is 225 kcal/mol (9.67 eV) [94]. The proton-transfer reaction in $A^{\bullet+}A$ (Eq. (4.2)) is therefore exothermic by 4 kcal/mol (0.17 eV). For $T^{\bullet+}$, the acidity is not available in literature. The measured proton affinity of neutral T is 209 kcal/mol (9.06 eV) [94, 95]. Experimentally, we observe an efficient protonation of T by $T^{\bullet+}$ (Eq. (4.3)), which indicates that the corresponding process is also energetically neutral or exothermic. This means that the acidity of the T radical cation should be <209 kcal/mol (9.06 eV). With this $T^{\bullet+}$ acidity and the A proton affinity of 225 kcal/mol, we expect an exothermic proton-transfer from $T^{\bullet+}$ to A (Eq. (4.4)) by >17 kcal/mol (0.74 eV). On the other hand, the proton-transfer reaction from the $A^{\bullet+}$ to T (Eq. (4.5)) is endothermic by 11 kcal/mol (0.49 eV).

An electron transfer can be a competing process in the T^+A base pair: this reaction is exothermic by 0.7 eV, based on the respective ionization potentials. Protonated monomers can also be formed by a H atom transfer from the neutral to the radical cation followed by dissociation. But thermodynamic data are not available to describe this process.

Thus, we expect AH^+ after exothermic proton transfer in $A_2^{\bullet+}$ and $AT^{\bullet+}$, followed by cluster dissociation, and TH^+ after the corresponding reaction in $T_2^{\bullet+}$. *The charged fragments are observed in the protonated monomers mass channels and therefore, reflect the properties (electron spectra and excited state dynamics) of the cluster.*

Electron spectra of AT clusters.

Fig. 4.17 shows electron spectra from coincidence measurements at a delay $\Delta t = 0$ for A and T, A and T clusters, the A-T base pair and the protonated cluster fragmentation products. The vertical lines mark the electron kinetic energies corresponding to the literature values for vertical ionization potentials of adenine and thymine [63, 81] (see subsec. 4.1.2 and subsec. 4.1.4). The electron spectra of the monomers A

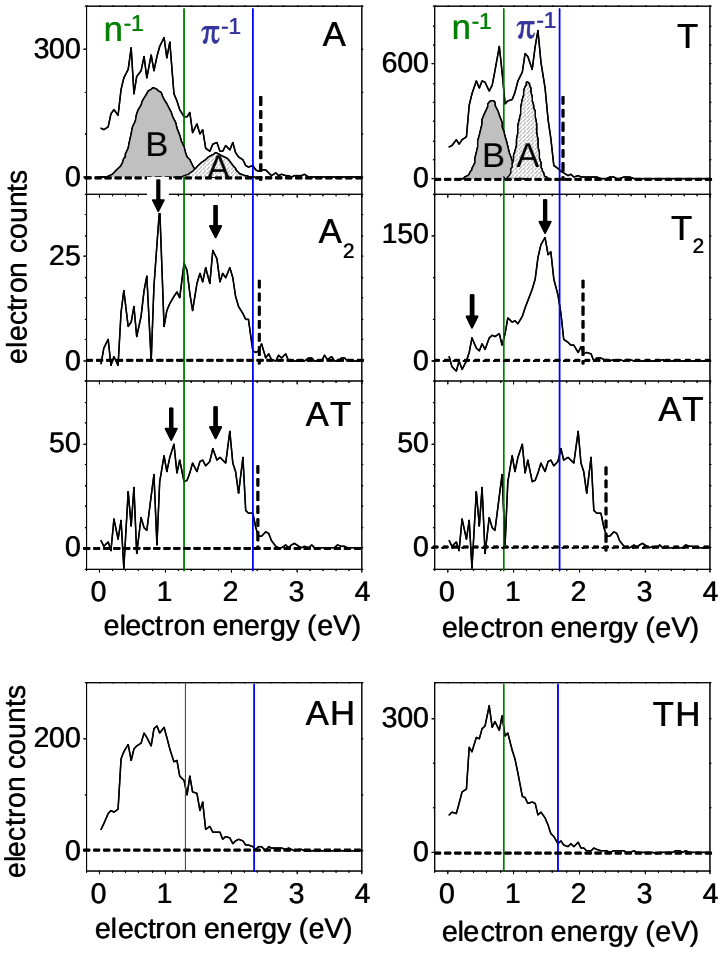

Figure 4.17: Coincidence electron spectra of adenine and thymine clusters, measured at the excitation and ionization wavelengths of 267 and 400 nm. The vertical lines indicate literature values for the vertical ionization potentials into the $D_0(^{-1}\pi)$ and $D_1(^{-1}n)$ states of A and T. Arrows and dashed lines mark electron kinetic energies that correspond to the observed vertical and adiabatic ionization potentials.

and T consist of two bands A and B. For both bases A and T, band A was assigned to ionization of the $\pi\pi^*$ state to the π^{-1} ionic state, and band B was assigned to ionization of the $n\pi^*$ state to the n^{-1} ionic state.

The spectrum of A_2 has a similar shape as that for A, where two electronic bands can be distinguished. The bands appear at similar electron kinetic energies as in the monomer spectrum. The relative intensities of the bands in A_2 are significantly different from those in A. The low-energy band in A_2 is strongly decreased, whereas it dominates in the spectrum of A. The similarity between the A-T and A_2 photoelectron spectra can be interpreted as evidence that the adenine chromophore was excited in both clusters. The T_2 spectrum, as compared to that of T, has a different band shape, because the low-energy band has almost completely vanished. The T_2 spectrum also differs significantly from the A-T spectrum.

We assigned the bands for the cluster spectra using literature ionization potentials for A and T monomers. The low-energy band was assigned to the $\pi\pi^* \rightarrow \pi^{-1}$ and the high-energy band to $n\pi^* \rightarrow n^{-1}$ ionization channels.

The experimentally observed vertical ionization potentials for the π^{-1} and n^{-1} state in A_2 were 9.12 eV and 9.95 eV, higher than those of adenine monomer (vertical arrows). For T_2, these values were 9.37 eV (π^{-1}) and 10.49 eV, lower than IPs for the corresponding monomer. In A-T base pair, the observed vertical ionization potentials of 8.89 eV and 9.74 eV for the π^{-1} and n^{-1} states were comparable to those of A_2.

The experimentally observed adiabatic ionization potentials could be only determined for the π^{-1} ionic states. For A_2 and AT clusters this value is 8.45 eV and it is only slightly different from the observed ionization potential of A monomer (8.43 eV). For T_2 cluster, the observed adiabatic ionization potential is 8.8 eV and it is by 0.3 eV lower than the corresponding value in the monomer (9.1 eV).

In the electron spectra of the dimers, we observed a strong decrease of the amplitude for the n^{-1} ionic state. This observation could indicate that the $n\pi^*$ excited state is not involved in the excited state relaxation of the clusters. Or alternatively, the decrease of the signal from the n^{-1} could be caused by asymmetric fragmentation in the ionic clusters as we discussed above. In order to fragment, ions must be vibrationally excited. Photoelectrons with high kinetic energies are correlated with low cationic states which should not have enough energy for fragmentation (this is the case for the band A and due to ionization into π^{-1} state). Electrons with low kinetic energies correlate with cationic states with large vibrational or electronic excess energy, and those cationic clusters may fragment rapidly. To identify the range of

electron energies where the electron spectrum remains undistorted by fragmentation, RRKM calculations were used to estimate the fragmentation rates[10]. The calculations predicted that ions with kinetic energies < 1.2 eV will fragment within 300 ns, and therefore before the electric field for mass analysis is turned on. Indeed, in the electron spectra of the clusters, we observed a drop of the electron signal at ~ 1.2 eV. At this electron kinetic energy, the "missing" signal was observed in the protonated monomer mass channels (see the bottom row of fig. 4.17). The cluster spectra in the region of high electron kinetic energy stay unperturbed. Thus, the electron spectra of T_2, A-T, A_2 clusters revealed the same electronic bands (due to the $\pi\pi^*$ and $n\pi^*$ states) and, therefore, resemble spectra of the monomers at zero delay tine.

Time-resolved dynamics in A and T clusters.

To investigate further photophysical processes in clusters, also at longer delay times Δt >0, we carried out time-resolved measurements. The delay between pump and probe pulses was scanned in time intervals in the range of few ps, tens of ps and hundreds of ps. For all graphs, the signal amplitudes can be compared within one figure, but not between figures, because the data were collected at different days. Also, for measurements in big time intervals, the ratios between the signal maxima at Δt ~ 0 and the signal amplitudes at positive delays may not reflect the exact population ratio, because the big scanning steps could not properly sample the ultrashort peak near $\Delta t = 0$. Fig. 4.18 and fig. 4.19 show the measured excited state dynamics of the monomers A and T and the protonated monomers AH and TH in the time interval of 0-140 ps.

The protonated monomer signals resulted from asymmetric ionic fragmentation in the A_2, T_2, and A-T clusters, and therefore also reflect the dimer dynamics. The dimer signals are not presented in these figures and will be discussed later. The time-dependent dynamics of A contains two decay components with life times $\tau_1 = 100$ fs and $\tau_2^{(A)} = 1.3$ ps, which were described in sec. 4.1.2. No additional long-lived components were observed in the presence of clusters (fig. 4.18a and fig. 4.19a). The same is true for T, the dynamics of which is characterized by a triple-exponential decay with life times $\tau_1 = 100$ fs, $\tau_2^{(T)} = 7$ ps, and $\tau_3 > 1$ ns (fig. 4.18b and fig. 4.19b). Besides the decay components with characteristic life times of the monomers, additional long-

[10]This work was done in collaboration with David Rayner and Niklas Gador, Steacie Institute for Molecular Science, National Research Council, Ottawa

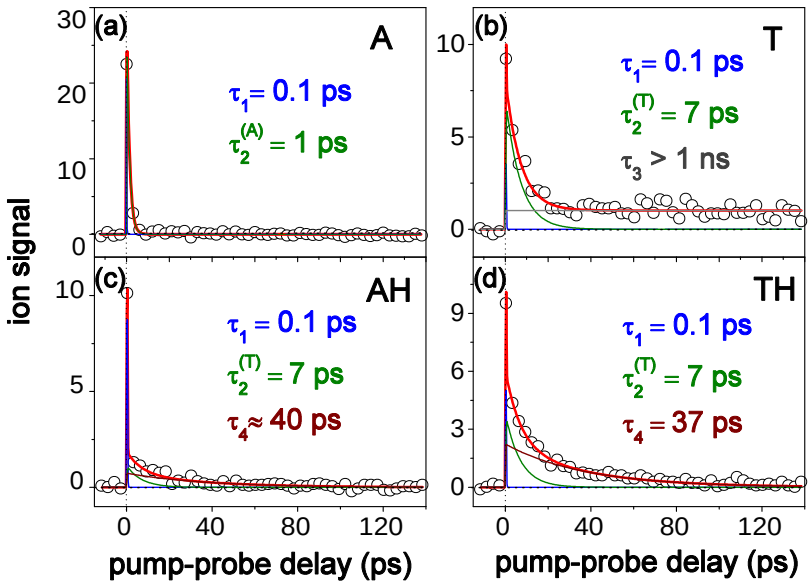

Figure 4.18: Time-dependent ion signals of the mixed A and T clusters measured for a long time interval with a pump wavelength of 267 nm and a probe wavelength of 800 nm. The fit curves (thick lines) for the experimental points (circles) identified four mono-exponential decays (thin lines) with life times τ_1...τ_4.

lived decay components (τ_4) were observed in the protonated monomer mass channels (fig. 4.18c,d and fig. 4.19c,d). The life times of these components were determined as 37 ps for TH and ∼40-50 ps for AH. With different probe energies of 800 nm (fig. 4.18) and 400 nm (fig. 4.19), we observed that the amplitudes of the fit components τ_1...τ_4 depend on the ionization process. With 800 nm ionization, signals with τ_1 and τ_2 are dominant, whereas τ_3 and τ_4 are better visible with 400 nm ionization. Therefore, the fit accuracy for τ_4 is higher with 400 nm ionization.

The time-resolved ion signals for the monomers, protonated monomers and the A_2 and A-T dimers measured on the intermediate time interval are shown in fig. 4.20. The measurements in the delay range between 0 and 45 ps allowed to fit the time constants $\tau_2^{(A)} = 1.3$ ps and $\tau_2^{(T)} = 7$ ps accurately. The values for τ_3 and τ_4 were extracted from experimental traces with a longer delay range (140 ps, fig. 4.18 and fig. 4.19) and used as constants to fit the traces in fig. 4.20. In the A_2 and A-T mass channels (fig. 4.20e,f), we observed only ultrafast dynamics. In the protonated monomer signals (fig. 4.20c,d) we observed characteristic life times of both A and T

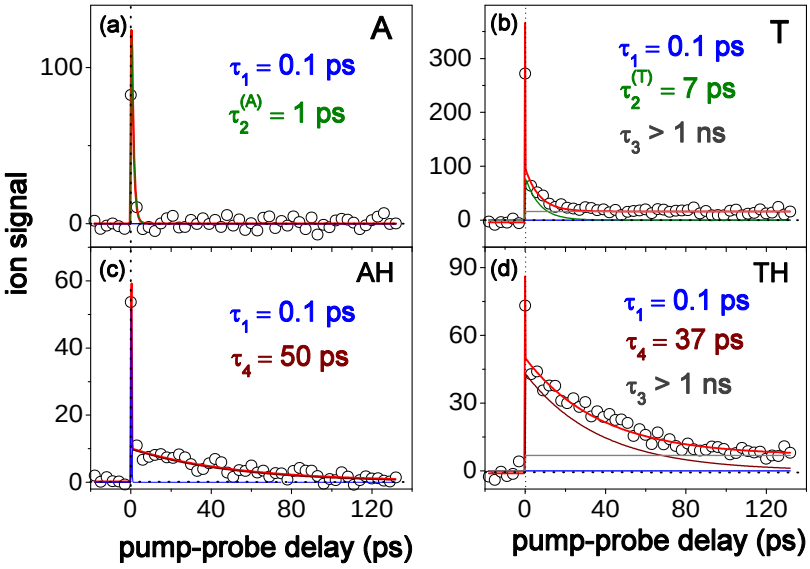

Figure 4.19: Time-dependent ion signals of the mixed A and T clusters measured for a long time interval at a pump wavelength of 267 nm and a probe wavelength of 400 nm. Otherwise as fig. 4.18.

monomers ($\tau_2^{(A)}$ and $\tau_2^{(T)}$). Whereas the signal with a life time $\tau_2^{(T)}$ is very small in the AH mass channel, both $\tau_2^{(A)}$ and $\tau_2^{(T)}$ are clearly seen in the TH mass channel.

On the short time interval (0 - 4 ps), we could accurately analyze short-lived transients (fig. 4.21 and fig. 4.22). These transients were fit with $\tau_1 = 100$ fs for all mass channels, except in the AH mass channel where τ_1 was fit with 200 fs. In these fits, τ_3 and τ_4 contributions were replaced with a constant offset. The decay dynamics of the dimers showed only an ultrafast decay with the time constant $\tau_1 \leq 200$ fs. The negative signals at positive delay times are due to fragmentation of vibrationally excited cationic clusters after probe-only ionization and absorption of an additional pump photon.

So far, we observed a superposition of different decay channels in both A and T species and in the protonated mass channels. To identify which decay components are due to homodimers (A_2, T_2) and which are due to heterodimers (A-T), we carried out time-resolved measurements in pure A clusters and in pure T clusters. The excited state dynamics for A, AH, and A_2 are shown in fig. 4.23.

Measurements within a 6 ps time interval were sufficient to characterize the excited

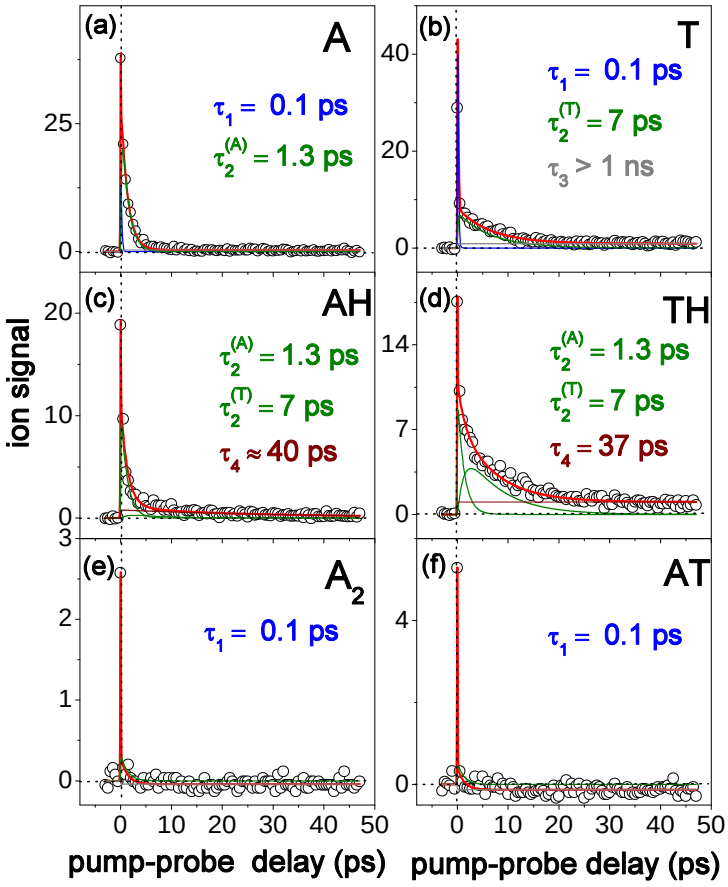

Figure 4.20: Time-dependent ion signals of the mixed A and T clusters measured for the intermediate time interval at a pump wavelength of 267 nm and a probe wavelength of 800 nm. Otherwise as fig. 4.18.

state dynamics in A and no long-lived traces were observed. Decay components $\tau_1 \leq$ 200 fs and $\tau_2 \leq 1.6$ ps were observed in both, A and AH mass channels. The dimer dynamics contained only a τ_1 contribution, due to fragmentation of cluster ions with longer-lived transients.

The excited state dynamics of pure T clusters is shown in fig.4.24. On a time interval 0 - 5 ps (fig. 4.24a, b), the excited state transients of T and T_2 are identical to the corresponding traces in the presence of heteroclusters (fig. 4.21 and fig. 4.22). The same time constants $\tau_1 = 100$ fs, $\tau_2 = 7$ ps, and $\tau_3 > 1$ ns are observed. On the 200 ps time scale, the dynamics of T and TH is dominated by the long-lived components τ_3 and τ_4 (fig. 4.24c, d). In the T signal, relative amplitudes of τ_3 and

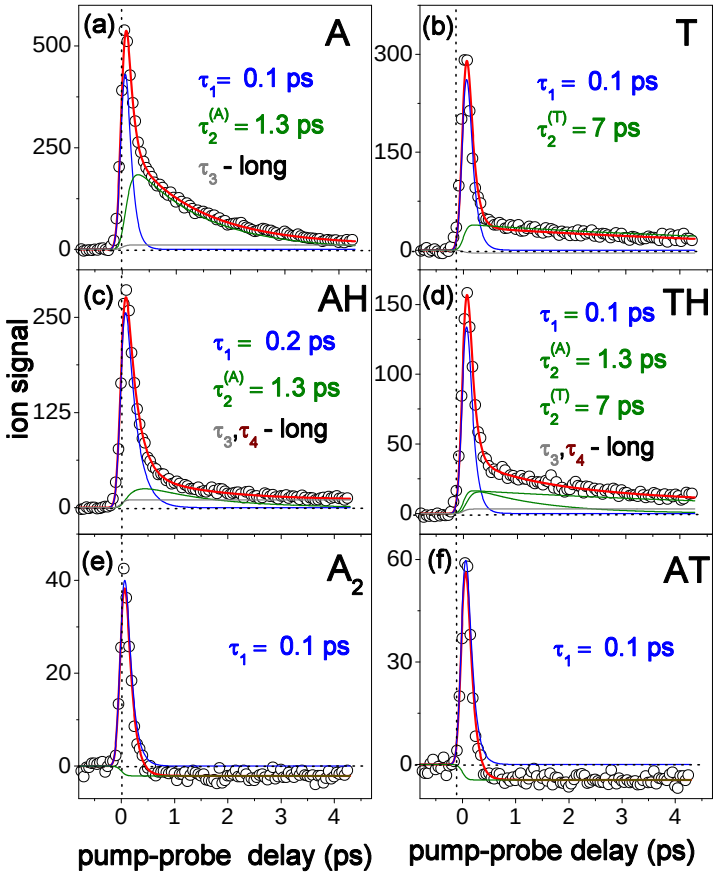

Figure 4.21: Time-dependent ion signals of the mixed A and T clusters measured for the short time interval at a pump wavelength of 267 nm and a probe wavelength of 800 nm. Otherwise as fig. 4.18.

τ_4 are comparable and small (<10 % of total amplitude). In the TH signal, the τ_3 transient has a small amplitude (∼10 % of total amplitude), and the amplitude of the τ_4 transient is the dominant contribution. This indicates that the life time τ_4 = 37 ps originates exclusively from T_2 clusters.

Based on our results we make the following conclusions concerning the excited state decay mechanisms in clusters:

- The time-dependent signals of the dimers A_2, T_2, and A-T exhibited only ultrashort excited state life times of $\tau_1 \leq 200$ fs (fig. 4.21e, f and fig. 4.22e, f). We established experimentally, that the excited state dynamics of the clusters are strongly influenced by fragmentation in the ionic clusters (presence of protonated masses). The ultrashort

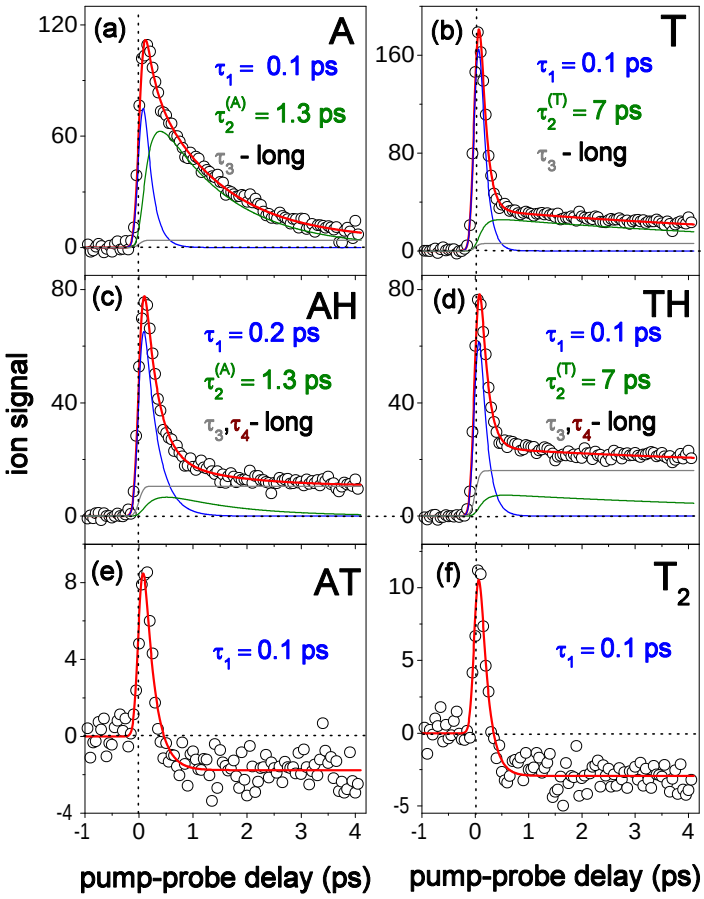

Figure 4.22: Time-dependent ion signals of the mixed A and T clusters measured for the short time interval at a pump wavelength of 267 nm and a probe wavelength of 800 nm. Otherwise as fig. 4.18.

decay components (τ_1) were assigned to $\pi\pi^*$ excited states, as in the monomers, based on their electron spectra. Because the corresponding ions contain little excess energy, signals from these states remain almost unperturbed in the cluster mass channels. The decay contributions with ps life times ($\tau_2^{(A)}$, $\tau_2^{(T)}$) were associated with the $n\pi^*$ excited state. This state was ionized into n^{-1} ionic state. The n^{-1} ionic states of the dimers fragmented very efficiently due to their large excess energy in the ion ($\gtrsim$1.1 eV). The corresponding signals of the n^{-1} states were transferred almost completely into the protonated monomers mass channels after cluster fragmentation.

- The measured excited state dynamics of the monomers and the protonated

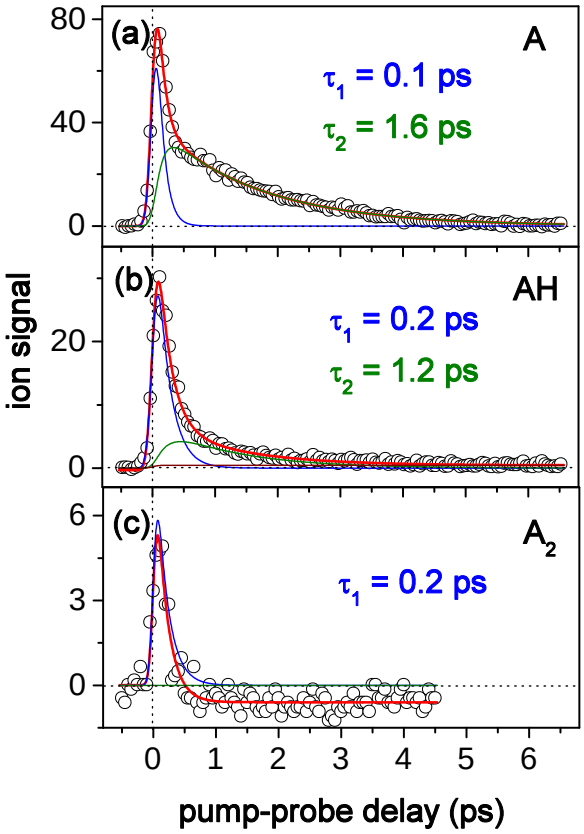

Figure 4.23: Time-dependent ion signals of pure A clusters measured at a pump wavelength of 267 nm and a probe wavelength of 800 nm. Otherwise as fig. 4.18.

monomers on a short and intermediate time intervals (fig. 4.20, fig. 4.21, fig. 4.22) showed that the life times $\tau_2 = 1.3$ ps (for A) and $\tau_2 = 7$ ps (for T) are identical in the monomers and clusters.

- Separate experiments on pure A and T clusters helped to assign the observed decay components. In pure A and A_2 cluster (fig. 4.23), a nearly identical excited state dynamics containing τ_1 and τ_2 components for the monomer and dimer were measured. However, we observed an increase of the τ_1 life time from 100 fs to 200 fs in the dimer and the corresponding fragment AH, which possibly could be due to a slower $\pi\pi^*$ relaxation in the presence of a partner. Since no other relaxation components (besides τ_1 and τ_2) were found in A_2 dynamics, we conclude that intermolecular interactions do not affect the excited state dynamics in A_2 cluster, in contrast to the

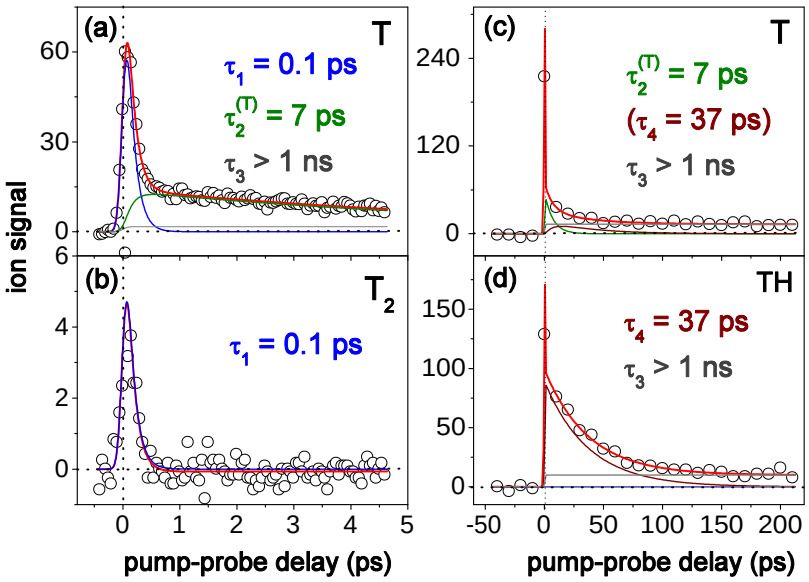

Figure 4.24: Time-dependent ion signals for pure T clusters measured at the pump wavelength of 267 nm and the probe wavelength of 800 nm (a, b) and 400 nm (c, d). Otherwise as fig. 4.18.

results by ns spectroscopy [88], where a proton-transfer in the cationic cluster was observed.

- In pure T clusters, an additional relaxation component with a life time τ_4 = 37 ps was identified (fig. 4.24c, d), which was not observed in the T monomer. The excited state with life time τ_4 was observed in the TH mass channel due to complete fragmentation of the base pair. The presence of the τ_4 component indicates that an additional excited state relaxation channel exists in T clusters. We suggest that an intermolecular interaction, such as a charge-transfer (CT) reaction, may affect the excited state relaxation in T_2. The time constant τ_3 >1 ns was also observed in thymine dimer and may be due to the same electronic state as in the monomer. We suggest that a low-lying triplet state could have a ns life time and explain the corresponding signals in our experiments.

- In the experiments with mixed clusters, we observed a characteristic life time of T ($\tau_2^{(T)}$) in the AH mass channel and a characteristic life time of A ($\tau_2^{(A)}$) in the TH mass channel. We explain this with the fact that in A-T dimer either the A or the T chromophores can be photoexcited. Due to proton-transfer followed by

fragmentation, $A_2^{\bullet+}$ and $AT^{\bullet+}$ can contribute signal to the AH mass channel, whereas $T_2^{\bullet+}$ can contribute signal into the TH mass channel. The transient with a life time τ_4 $\sim$ 40-50 ps can have different explanations. Theory predicted several intramolecular $\pi\pi^*$ and $n\pi^*$ excited states, that may be stabilized in the clusters and therefore trap excited state population on the ps time scale [87]. Alternatively, theoretical calculations of the ground state isomers for the A-T cluster revealed many structures in planar and stacked configuration. Therefore, the long-lived state with a life time τ_4 in A-T clusters could be assigned to an intermolecular state in planar [87] or stacked clusters [96].

Chapter 5

Hydrated DNA bases and base pairs

In the previous chapters we presented experimental results combined with theoretical calculations for the isolated bases and base pairs. We also discussed literature data for liquid phase studies for comparison. It should be mentioned that our detailed understanding of the gas phase experiments, however, can not be extended easily to the liquid phase, where complex interaction with the solvent must be taken into account. Therefore, we carried out microhydration experiments which offer a bridge between gas phase and liquid phase to get a better understanding of excited state dynamics of biological molecules in a complex environment.

5.1 Excited state dynamics of hydrated monomers

The effects of microhydration will be presented first for the monomers (A, T). Only small water clusters with up to three water molecules will be discussed. The excited state dynamics of the hydrated clusters was studied by time-resolved mass spectroscopy. Some of the clusters were also studied by electron spectroscopy.

5.1.1 Hydrated adenine

We start our discussion with microhydrated adenine, since it is the best understood among the three bases presented here. The excited state dynamics of isolated adenine in our experiments was characterized with a double-exponential decay. Two transients identified in our experiments were assigned to the decays of the optically bright $\pi\pi^*$ state ($\tau_1 \leq 100$ fs) and a dark $n\pi^*$ state ($\tau_2 = 1.3$ ps). Another electronic

state of $\pi\sigma^*$ character was theoretically predicted to lie higher in energy. Using an excitation wavelength of 267 nm we did not detect the latter, however, it may play a role at shorter excitation wavelengths. For adenine in solution, a single-exponential decay was measured with a life time $\tau_1 \sim 300$ fs [61]. Theory offers several possible explanations for the shorter excited state life time in solution. One explanation is based on the lowering of the $\pi\sigma^*$ state energy in a polarizable environment. The $\pi\sigma^*$ state has a large dipole moment and can be stabilized in polarizable environments such as water [7]. If the stabilization energy is large enough, relaxation via the $\pi\sigma^*$ state can compete with internal conversion to the $n\pi^*$ state, decreasing or completely removing the contribution of the latter in the excited state decay. The life time of the $\pi\sigma^*$ state is expected to be very short [7, 41] due to the presence of a conical intersection with the ground state or dissociation along a H-stretch coordinate. Experimental detection of the $\pi\sigma^*$ state can, therefore, be difficult. Another possible explanation for the different dynamics in the gas and condense phase was described in the theoretical work of Marian [35]. For isolated adenine it was proposed that one of the bright $\pi\pi^*$ states crosses the ground state in a barrierless manner, providing a fast excited state relaxation pathway. The $n\pi^*$ state was found nevertheless lower in energy and in isolated adenine also plays a role. Environment may possibly increase the energy ("blue shift") of the $n\pi^*$ state, making it energetically no more accessible with our excitation wavelength. Such a "blue-shift" for the $n\pi^*$ state in hydrated bases was mentioned in literature [6, 35, 40], but nowadays there are no theoretical calculations, confirming this effect. In addition, experimental observation of the $n\pi^*$ state can be impeded by a strong fragmentation of fragile weakly-bound water clusters. Fragmentation can be identified and investigated, if fragmentation products are different from the parent molecules, as it was found for A and T clusters. Otherwise, identification of fragmentation with pump-probe ionization spectroscopy in clusters is difficult.

Experimental results

The results of pump-probe measurements for $A(H_2O)_n$ with n=1...3 are shown in fig. 5.1. The major feature of the cluster dynamics is a drastically different excited state decay. In comparison with the monomer (fig. 5.1a), the ps component completely vanished in the dynamics of the clusters and only the ultra short contribution τ_1 remained (fig. 5.1b,c,d). No significant difference in the dynamics of water clusters of different size was observed, except for a slightly varying value for τ_1. To explain the

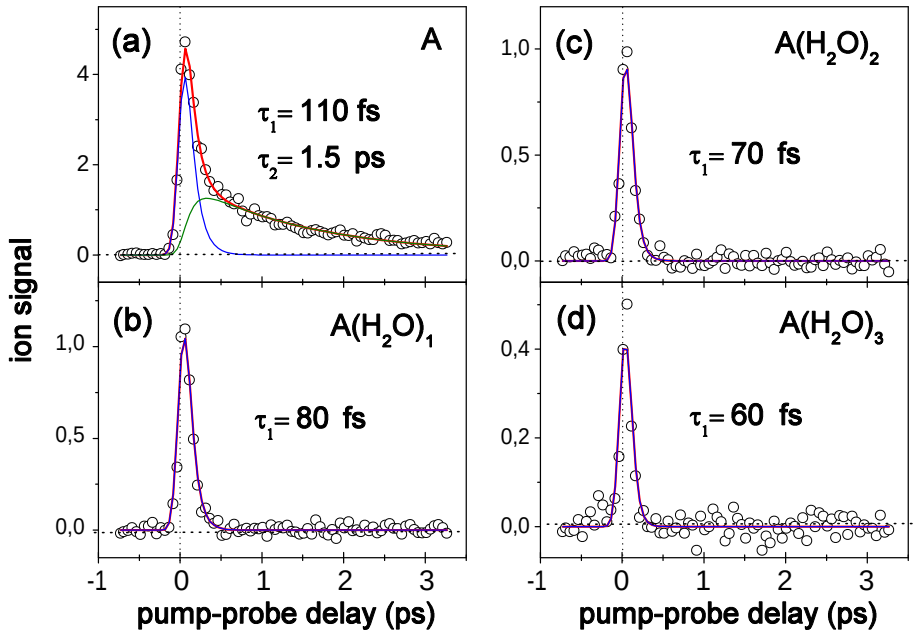

Figure 5.1: Time-dependent ion signals of $A(H_2O)_n$ clusters for n=0...3 measured at a pump wavelength 267 nm and a probe wavelength of 800 nm. Experimental points (circles) were fitted with a double-exponential decay for adenine and a single exponent for water clusters.

results obtained, a theoretical investigation with *ab initio* methods was performed by H.-H. Ritze [61]. In these calculations the stabilization of a $\pi\sigma^*$ state in the hydrated clusters was considered. One water molecule was included in the calculations. The geometry optimization was carried out with the CASSCF [1] method. The energies were obtained with the MRPT2 [2] method where the 1s electrons were kept frozen. The most stable structures of the $A(H_2O)_1$ complex (fig. 5.2) were taken from a previous theoretical study of Hanus et al. [34].

Each of the isomers is characterized by two hydrogen bonds with a water molecule. One of the bonds is formed between N of the adenine ring and H of the water, and the other bond is between O of the water and H in the amino or azine group of adenine. The ground and excited states energies were optimized for the shown isomers. The results of these optimizations are shown in table 5.1.

[1] complete active space self-consistent-field
[2] multireference second-order perturbation theory

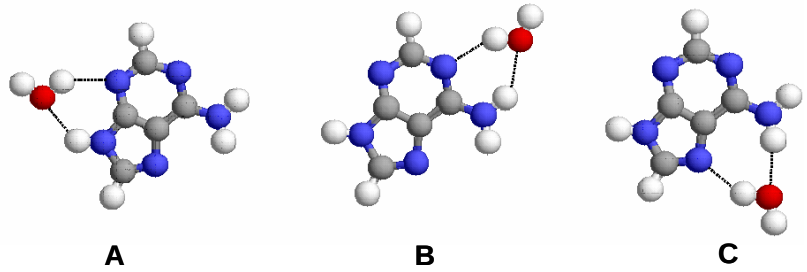

Figure 5.2: Equilibrium structures of three $A(H_2O)_1$ isomers.

Table 5.1: Calculated adiabatic energy differences between the azine and amino σ^* orbitals in bare adenine and in $A(H_2O)_1$ isomers A, B, C.

Isomer	A	B	C
σ^*-orbital (azine)	0.17	0.21	0.18
σ^*-orbital (amino)	0.14	0.15	0.17

The values in the table are the energy difference between the excited state energy of adenine and its hydrated clusters. The energies of the $\pi\sigma^*$ states located on the azine and amino groups for different isomers were found to be lower than the corresponding energies in bare adenine. For all three isomers, the σ^* orbital was strongly stabilized independent of the water position. Despite the energy decrease of 0.14 - 0.21 eV, the $\pi\sigma^*$ state still lies above the optically bright $\pi\pi^*$ state. However, the $\pi\pi^*$-$\pi\sigma^*$ coupling may be expected to increase and may dominate as compared to the $\pi\pi^*$-$n\pi^*$ coupling. As a result, the $n\pi^*$ contribution in the experimentally observed dynamics may be drastically decreased. The measured time-resolved signals shown in fig. 5.1 agree with this statement. Because the relaxation of the $\pi\sigma^*$ state is expected to be very fast and we can not expect to observe the corresponding transient signals. But other possible reasons for observed ultrafast excited state dynamics in hydrated adenine can not be excluded. One is the possibility of a conical intersection of the $\pi\pi^*$ state with the ground state in the absence of the blue-shifted $n\pi^*$ state. Another is the possibility for very efficient cluster fragmentation in the ionic state. The former was not yet theoretically confirmed for adenine-water clusters, it only was suggested to play a role [40], and the latter is very difficult to prove with pump-probe ionization spectroscopy. The ns-fs hole-burning experiments described in sec. 7.1 could help to distinguish native cluster dynamics from fragmentation in the future.

5.1.2 Hydrated thymine

Qualitatively, the hydration picture of thymine was found to be very similar to that observed for adenine. The time-resolved dynamics for $T(H_2O)_n$ clusters with n=0...2 is shown in fig. 5.3. The ps and ns contributions in the cluster with one water

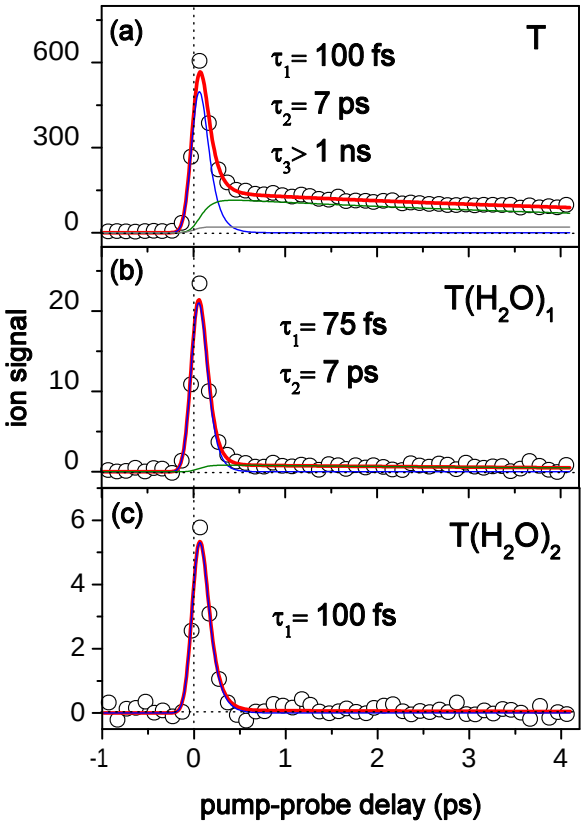

Figure 5.3: Time-dependent ion signals of $T(H_2O)_n$ clusters with n=0...2 measured with a pump wavelength 267 nm and a probe wavelength of 800 nm. Experimental points (circles) were fitted with three exponential decays for T, two exponential decays for $T(H_2O)_1$, and one exponential decay for $T(H_2O)_2$ clusters.

molecule is strongly decreased and represents only $\sim 5\%$ of the total signal (fig. 5.3b). Two water molecules remove completely the long-lived signal.

To explain the obtained results, we considered two possible models: the effect of low-lying $\pi\sigma^*$ states (as for $A(H_2O)_n$ clusters) and the possibility of a changed order of the $\pi\pi^*$ and $n\pi^*$ states. Both models were checked with the help of *ab initio*

calculations in collaboration with L. González. The same theoretical methods as for the calculation of thymine tautomers in subsec. 4.1.3 were applied. One and two water molecules were included in the calculations (fig. 5.4).

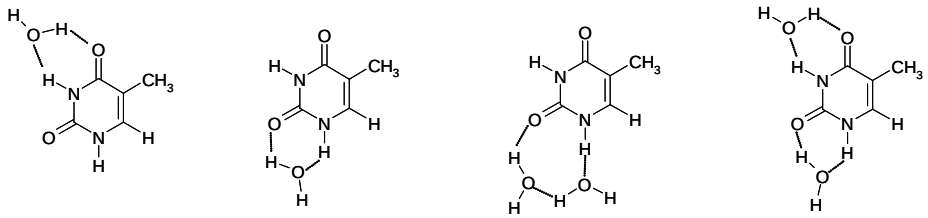

Figure 5.4: Low energy conformations of singly (TW1 and TW2) and doubly (TW3 and TW4) hydrated thymine clusters.

The structures for the most stable water complexes were taken from the work of Kabeláč et al. [97]. The monohydrated clusters (fig. 5.4, TW1, TW2) were formed by two hydrogen bonds between an O of thymine and a H of water, and between the O of water and a H of thymine. The clusters with two water molecules were formed as a sum of the structures TW1 and TW2 (fig. 5.4, TW4), and with two water molecules in a chain assembly (fig. 5.4, TW3). In the ground state, all studied water clusters were found to be nearly degenerate and should be experimentally accessible.

Additionally, all water clusters can be photoexcited, because their vertical excitation energies for the $\pi\pi^*$ states were found to be comparable with those for the T1 tautomer (fig. 5.5). The obtained tautomers can be separated into two groups: one group with a big $\pi\pi^*$-$n\pi^*$ energy gap similar to that in the T monomer (structures TW2, TW3) and the other group, where the $\pi\pi^*$-$n\pi^*$ gap was significantly reduced mostly due to a "blue-shift" of the $n\pi^*$ state (structures TW1, TW4). Since adiabatic energies were not calculated in our study, we can make only tentative conclusions. For the structures TW2 and TW3, an excited state decay similar to that in T1 could be expected, because the order of the excited states is the same, and the gap between the states is similar to that of T1. For the second group of structures (TW1 and TW4), the order of the excited states remains the same as for T1, but the energy gap between the states becomes very small. We may therefore expect a different relaxation pathway for these clusters, dominated by a fast decay of the $\pi\pi^*$ excited state directly to the ground state via a conical intersection. The $n\pi^*$ contribution in this case should be small or vanishing as observed in our experimental data (figs. 5.3b, c).

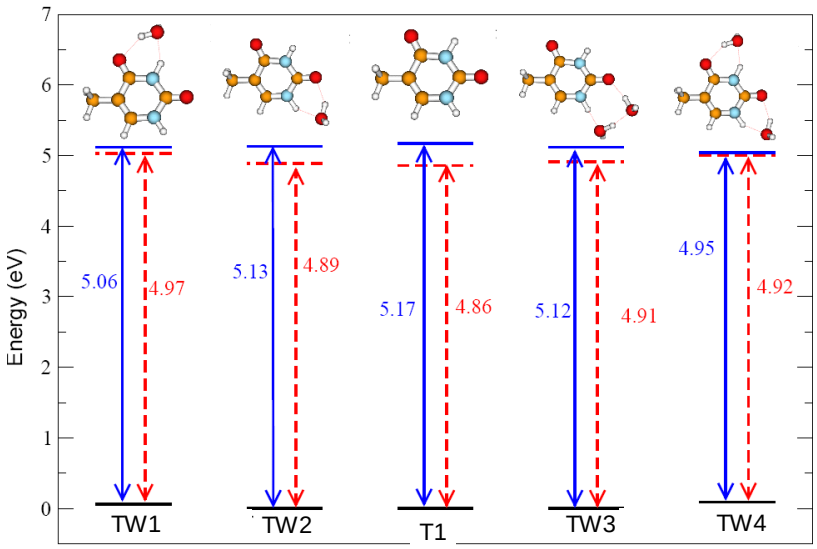

Figure 5.5: *Ab initio* calculated ground state energies (relative to respective lowest energy tautomers T1, TW2 and TW3) and vertical excitation energies for thymine-water tautomers (TW1-TW4) and the canonical tautomer of thymine (T1). Solid and dashed lines show $\pi\pi^*$ and $n\pi^*$ states respectively. The energy of the lowest energy tautomer (T1, TW2, TW3) was set to 0.

We, however, can not explain why no monomer-like contribution from the TW2 and TW3 tautomers is observed, i.e., a $n\pi^*$ signal with ps life time. A possible explanation for the absence of the $n\pi^*$ contribution is ionic fragmentation of the clusters. In this case, the $n\pi^*$ state signals are observed in the fragment mass channel (T) but not in the parent mass channel ($T(H_2O)_n$). This suggestion can be only tested with a ns-fs hole-burning method when different clusters can be selectively excited and investigated.

The energies of the $\pi\sigma^*$ states in water clusters of thymine were also calculated (not shown in fig. 5.5). The lowest $\pi\sigma^*$ with a vertical excitation energy of 5.78 eV (more than 0.5 eV above the bright $\pi\pi^*$) was found for the TW1 tautomer. For the remaining tautomers, higher $\pi\sigma^*$ energies were calculated. Similar situation was found in the T1 canonical tautomer. Based on the calculated $\pi\pi^*$ - $\pi\sigma^*$ energy difference we propose that $\pi\sigma^*$ states play only a minor role in the relaxation dynamics of hydrated thymine.

5.2 Excited state dynamics of hydrated dimers

We investigated the excited state processes in hydration adenine dimer and the results were drastically different from those for the hydrated monomers. Fig. 5.6 shows the time-resolved dynamics for A, A_2 and their clusters with three water molecules. The

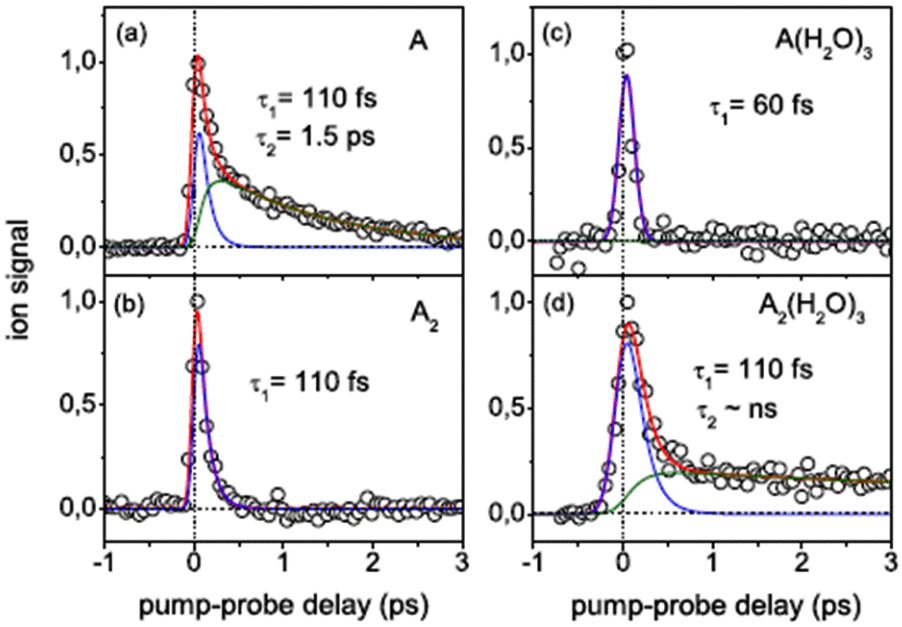

Figure 5.6: Time-dependent ion signals of A, A_2, $A(H_2O)_3$, and $A_2(H_2O)_3$ clusters measured with a pump wavelength 267 nm and a probe wavelength of 800 nm.

dynamics of A, A_2, $A(H_2O)_3$ was already discussed in sec. 5.1. In adenine and adenine dimer, two excited states with life times $\tau_1 < 160$ fs and $\tau_2 < 1.6$ ps (fig. 4.23) were identified. In $A(H_2O)_3$, only a fast relaxation process with $\tau_1 = 60$ fs was observed (fig. 5.1). The dynamics of the $A_2(H_2O)_3$ cluster contains two major contributions: an ultrafast decay ($\tau_1 = 110$ fs) and a slow component with a long life time ($\tau_2 \sim$ ns). The latter was characterized in longer scans, but the life time could not be exactly determined due to the limited range of the delay stage (~400 ps). The long-lived contribution τ_2 was observed in all $A_2(H_2O)_n$ clusters for n>2, but it vanished when we reduced the cluster distribution to n≤2. Similar observations of a long-lived excited state were made in single-stranded adenine polymers in the liquid phase. The nature of this state was not identified by the authors but it was suggested that the long-lived state might be delocalized over several stacked adenine bases [98]. Stacked

structures were also predicted by an exhaustive theoretical investigation of hydrated A_2 clusters in the gas phase [96]. Calculations showed that adenine dimer has a planar H-bound structure. In the presence of more then two water molecules the stacked structure of the cluster becomes dominant (fig. 5.7). Calculated populations

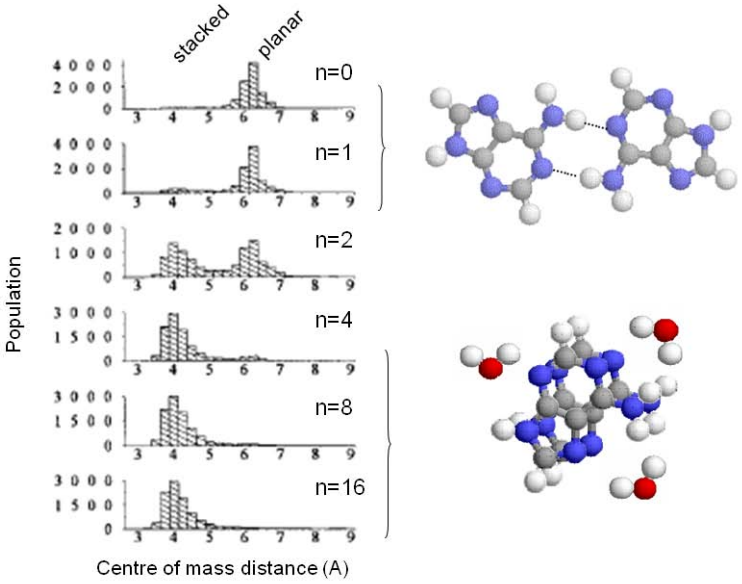

Figure 5.7: Calculated populations (left) of $A_2(H_2O)_n$ clusters for n=0 (top), $n = 1$, $n = 2$, $n = 4$, $n = 8$, and $n = 16$ (bottom) (reproduced with permission from ref. [96]). The small center of mass distances correspond to stacked cluster structures, the large distances correspond to H-bound planar structures. The pictures on the right illustrate possible planar and stacked structures.

of hydrated A_2 clusters are shown as a function of an intermolecular distance for different numbers of water molecules. For pure A_2 and $A_2(H_2O)_1$ the maximum population was found for the distance of 6.2 Å. This distance corresponds to the planar configuration of the clusters [96]. For the $A_2(H_2O)_2$ cluster approximately equal populations for a small ($\sim$ 4 Å) and a large (6.2 Å) intermolecular distances were found. The small distance corresponds to the stacked configuration of the cluster, because the chromophores are located closer to each other. When 4 and more water molecules are clustered with A_2, only the stacked structures were found. Based on this calculation we can propose that the long-lived trace in the measured dynamics (fig. 5.6d) is due to a structural change from a planar to a stacked geometry of the

cluster. We aimed to determine the origin of the unknown state in the stacked clusters and carried out FEICO experiments for A, A_2, $A(H_2O)_3$, and $A_2(H_2O)_3$ clusters (fig. 5.8). The spectrum of adenine showed two electronic bands corresponding to

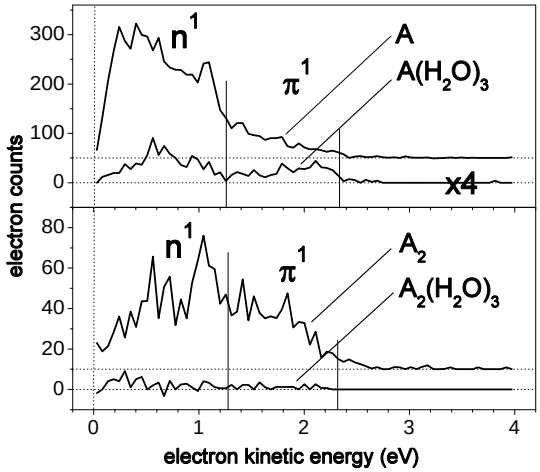

Figure 5.8: FEICO spectra of A and A_2 with three water molecules measured with a pump wavelength of 267 nm and a probe wavelength of 400 nm at $\Delta t = 0$. For easier viewing, the spectra of A and A_2 were shifted. The spectrum of $A(H_2O)_3$ was multiplied by a factor of 4. The vertical lines indicate the electron kinetic energies that correspond to the IPs for the $\pi\pi^*$ and $n\pi^*$ excited states of adenine.

the $\pi\pi^*$ state ionized into the π^{-1} ionic state (2.37 eV) and the $n\pi^*$ state ionized into the n^{-1} state (1.27 eV). The $n\pi^*$ contribution decreased in A_2 and $A(H_2O)_3$ cluster. Characterization of the spectrum for the $A_2(H_2O)_3$ cluster was rather difficult due to the very small size of the corresponding signal. This is not surprising because the intensity of the corresponding cluster signal in the mass spectrum was only a tiny fraction of the total signal (fig. 5.9). Therefore, the pump-probe contrast was poor for bigger clusters and we could not get enough electron signal after subtraction of the one-color signals even after summing up many data sets. To circumvent this problem we measured the integrated electron spectrum at the time delay of 50 ps. At such long delays in the time-resolved spectra we observed only the long-lived signal from the $A_2(H_2O)_n$ clusters for n>2 (fig. 5.6d). All short-lived signals from the remaining clusters decayed to zero. By measuring the total electron spectrum we could not assign, however, photoelectron spectra for individual cluster species, but observed the sum of the spectra of all larger clusters with long-lived transients. Fig. 5.10 shows the

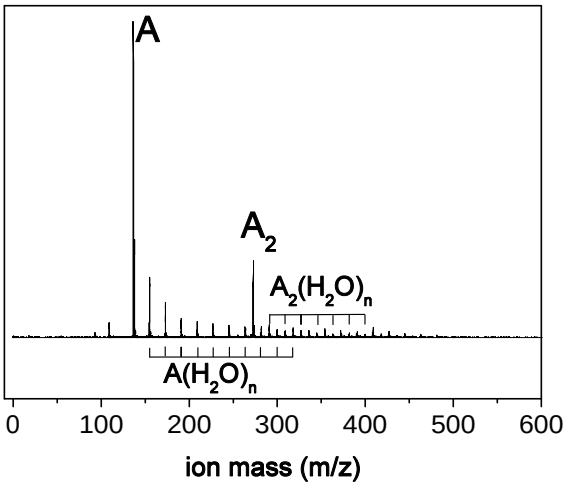

Figure 5.9: Mass spectrum of A- and A_2-water clusters corresponding to the FEICO spectra in fig. 5.8.

first electron spectrum of the stacked $A_2(H_2O)_n$. Two bands were observed in the spectrum. The bands do not correlate with the expected electron kinetic energies for the ionization to the π^{-1} and n^{-1} ionic states of adenine monomer (EKE = 2.37 eV and 1.27 eV respectively). The character of the new long-lived state could be the same as for the single-stranded A in solution [98], where the formation of an excimer state was suggested. In our group we carried out preliminary *ab initio* calculations, which indicated a presence of a low-lying excimer state in the stacked A_2. The results of these calculations are depicted in fig. 5.11. On the left hand side of fig. 5.11 we show the π (HOMO) and π^* (LUMO) orbitals for adenine monomer. The vertical excitation energy was calculated to be 4.95 eV. The electronic configuration of a stacked adenine dimer on the right hand side was constructed by linear combination of HOMO and LUMO orbitals of monomers. The symmetric and antisymmetric linear combinations of molecular orbitals show considerable splitting. The arrows show allowed transitions between the obtained states. The calculated energies for these transitions are 4.53 eV (sym-antisym) and 4.92 eV (antisym-antisym). By comparison the excitation energies for the monomer and the dimer we show that there is an additional low-lying excited state in the stacked A dimer (sym-antisym, 4.53 eV). The difference of 0.42 eV between excitation energy in the monomer (4.95 eV) and the lowest excitation of the

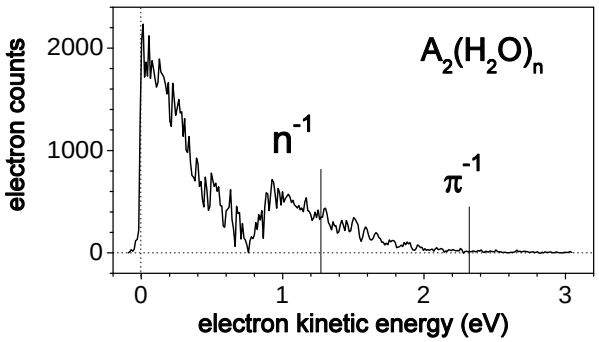

Figure 5.10: Integrated electron spectrum of $A_2(H_2O)_n$ clusters measured with a pump wavelength of 266 nm and a probe wavelength of 400 nm at a time delay of 50 ps. The vertical lines show the electron kinetic energies corresponding to the ionization potentials of the $\pi\pi^*$ and $n\pi^*$ excited states of adenine. The observed bands differ strongly from those observed for isolated adenine.

dimer (4.53 eV) may be sufficient to trap dimer population in the lowest excited state and lead to excited state life times longer than in the monomer. We, therefore, may expect a ns life time for this excimer state which agrees with the observed dynamics shown in fig. 5.6b.

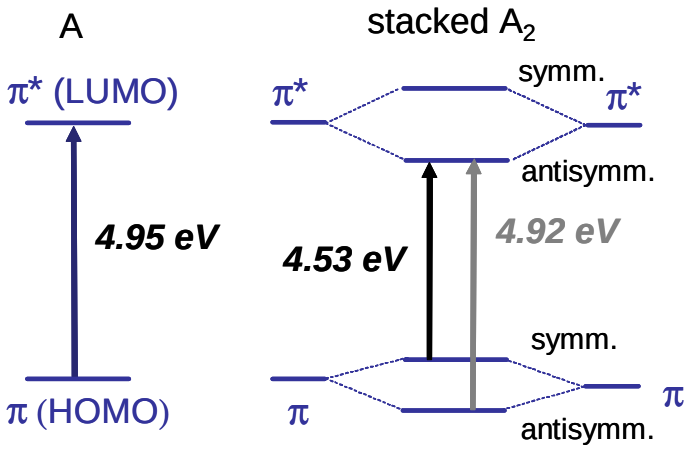

Figure 5.11: Calculated adiabatic excitation energies of the π (HOMO) and π^* (LUMO) orbitals of A and stacked A_2. Vertical arrows show allowed transitions. A new low-energy (possibly excimer) state with an adiabatic excitation energy of 4.53 eV was identified. This state might be photoexcited directly, or trap the excited state population after the excitation of local excited states. We propose that this excimer state is responsible for the long-lived transient in fig. 5.6d and the observed photoelectron bands in fig. 5.10.

Chapter 6

Methylated DNA bases and base pairs

Methylated bases A and T and their base pairs were investigated with time-resolved mass spectroscopy. Excited state life times were determined in the monomers and in the clusters. Our results for the monomers are in good agreement with previous studies in literature. The results for clusters, however, should be considered as preliminary.

6.1 Methylated A and T monomers

We investigated the methylated compounds of A and T with methyl groups (CH_3) in the 9-position in adenine and in the 1-position in thymine (fig. 6.1). As in these positions sugar and phosphate group are attached in DNA, we could consider the methylated A and T bases as small mimetic systems for their nucleosides (base + sugar) and nucleotides (base + sugar + phosphate).

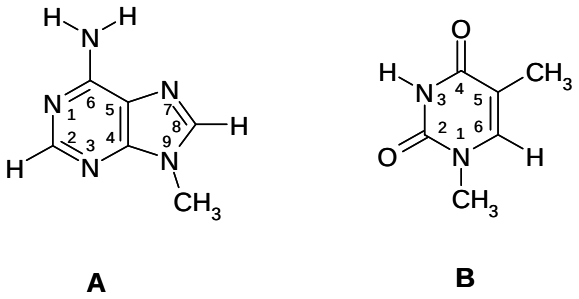

Figure 6.1: Structures of 9-methyladenine (A) and 1-methylthymine (B).

Previous time-resolved measurements of 9-MA in the gas phase showed a double-exponential decay with time constants τ_1=110 fs [51] and τ_1=1-1.3 ps [31, 51]. The life times were very similar to those observed for pure adenine. It was concluded that methylation in the 9-position does not change the photophysics of this molecule dramatically. To remind you, according to the calculation of Domcke and Sobolewski [7, 41], $\pi\sigma^*$ states were predicted to play a role in isolated adenine. One of them is localized on the azine group (9N-H). Methylation in the 9-position should, therefore, strongly modify the coupling between the $\pi\pi^*$ and $\pi\sigma^*$ states and cause a change in the excited state dynamics. Similar dynamics for A and 9-MA indicate that the $\pi\sigma^*$ states are not involved in the excited state relaxation of adenine. The excited state dynamics of 1-MT in the gas phase was not yet investigated to the best of our knowledge. Time-resolved data for a similar component, 1,3-dimethylthymine (1,3-DMT) were only published [74]. The nanosecond REMPI experiments applied in ref. [74] revealed a long-lived state for this molecule with a life time of 170 ns.

We present time-resolved measurements for the 9-MA, that are in accordance with the earlier results and for the first time for 1-MT. The fig. 6.2 shows the dynamics for the methylated monomers of A and T. The time-resolved signal of 9-MA was fitted with a double-exponential decay with a life times of τ_1=120 fs and τ_2=1 ps (fig. 6.2a). These values are very similar to those for pure adenine (<100 fs and 1.3 ps), and we suggest that the same excited states of $\pi\pi^*$ and $n\pi^*$ character contributed to the relaxation dynamics. For 1-MT, three components were identified. The short (τ_1 = 80 fs) and the intermediate (τ_2 = 2.9 ps) transients were also assigned to the $\pi\pi^*$ and $n\pi^*$ states as in T. Compared to pure thymine, however, the life time τ_2 was found to be shorter by more than a factor of two. The reason for this life time shortening is so far unknown due to a lack of theoretical calculations and comparable experimental results in the literature. We also introduced a third decay τ_3 to better reproduce the experimental points based on the fact that ns life times for T and 1,3-DMT were reported in literature [74]. The amplitude of the ns trace was rather very small in all measured time intervals (fig. 6.2b,c). Therefore, we showed that methylation does not change the excited state dynamics of thymine significantly.

6.2 Methylated A and T base pairs

We also carried out pump-probe ionization measurements on methylated base pairs of adenine and thymine. The obtained dynamics is shown in the fig. 6.3. The signal

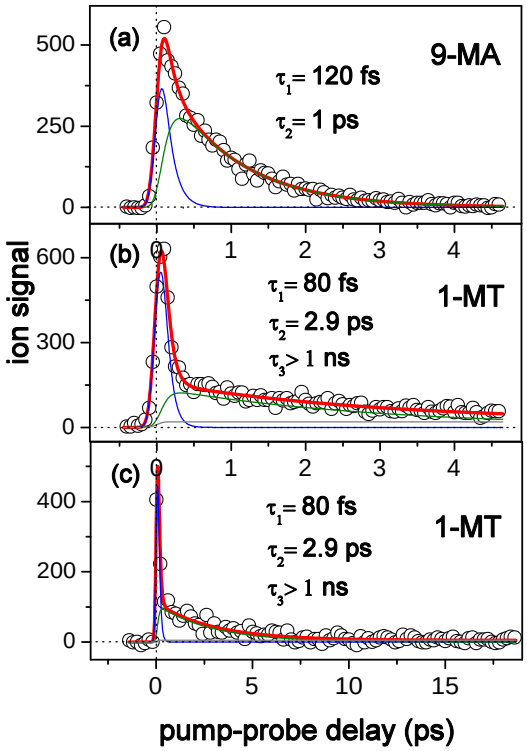

Figure 6.2: Time-resolved ion signals of methylated A (9-MA) and T (1-MT) measured with a pump wavelength 267 nm and a probe wavelength of 800 nm for a very narrow cluster distribution. Experimental points (circles) were fitted with two exponential decays for 9-MA and three exponential decays for 1-MT. In 9-MA, all transients decay rapidly to zero and we show only a short interval scan (a), whereas for 1-MT we show scans for a short (b) and intermediate (c) time interval because of the long-lived transient τ_3.

for 9-MA_2 was fitted with a triple-exponential decay to reproduce the experimental points. The τ_1 life times were adapted from the corresponding monomer signals measured with a very small cluster distribution (fig. 6.2a,b). The $\tau_2 = 1.6$ ps life time for 9-MA_2 and the $\tau_2 = 5$ ps life time for 1-MT_2 were obtained from the monomer dynamics (not shown) of the same data set as the dimers and kept constant. The τ_3=12 ps for 9-MA_2 and τ_3>1 ns were fitted as free parameters. To fit the mixed 9-MA-1-MT cluster, it was assumed that it could show features of one or the other chromophore. Better fit was obtained with the τ_1 and τ_2 for the 9-MA. The τ_3 was fitted as a free parameter and almost exactly matched the 12 ps found in 9-MA_2.

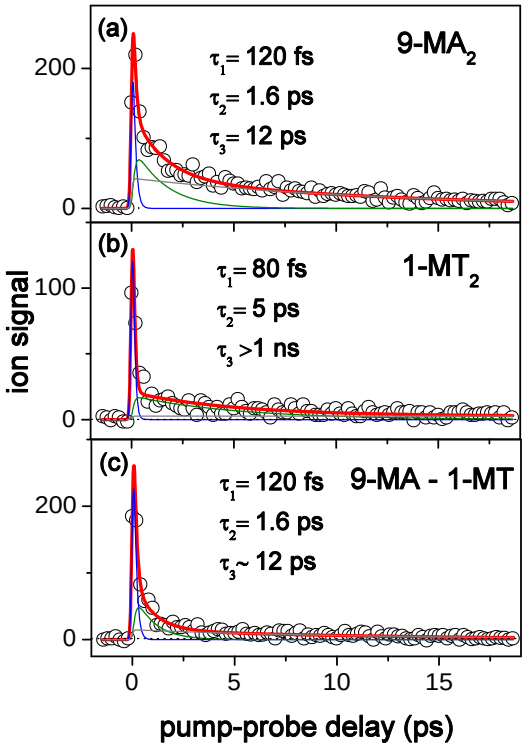

Figure 6.3: Time-resolved ion signals of methylated A and T dimers measured at a pump wavelength 267 nm and a probe wavelength of 800 nm for the broader cluster distribution (n=1,2). Experimental points (circles) were fitted with three exponential decays.

The obtained life times allowed us to make the following preliminary conclusions. The τ_1 and τ_2 contributions could be assigned to an excited state relaxation via the $\pi\pi^*$ and the $n\pi^*$ states, respectively, as in non-methylated base pairs. Somewhat longer τ_2 life times for 9-MA and 1-MT in the presence of clusters (fig. 6.3) as compared to the isolated 9-MA and 1-MT (fig. 6.2) may be due to fragmentation of bigger clusters. The longer-lived τ_3 life times might originate from clusters of stacked geometry. Theoretical *ab initio* calculations for methylated A and T clusters [96] predict a significant amount of these structures in the gas phase: ∼50 % for 9-MA_2, ∼77 % for 1-MT_2 and ∼80 % for 9-MA-1-MT. For non-methylated base pairs, the amount of stacked structures was predicted to be smaller. This fact may explain the difference in the dynamics of methylated and non-methylated base pairs. Alternatively, τ_3 life times may be a result of intermolecular processes in the clusters. We

can also agree with statements in the literature [7, 41] that the similarity in the excited state dynamics of A and 9-MA rules out relaxation via the $\pi\sigma^*$ state in isolated adenine. Otherwise, a drastic change in the excited state dynamics due to the methyl substitution in the azine group would be expected.

Chapter 7

Isomer separation

The experimental results presented in the previous chapters showed that the interpretation of pump-probe experiments of clusters can be difficult due to the factors: presence of many isomers, the dynamics of which can not be distinguished so far, and fragmentation processes, which change the dynamics observed for the parent and the daughter masses. To overcome these limitations, we worked towards an isomer separation method - hole-burning - which can be combined with the fs pump-probe experiments.

7.1 Introduction to the hole-burning technique

The spectral hole-burning method is based on the fact that a selected molecular species can be removed from a molecular beam by absorption of light from a "burn" laser. In ns REMPI experiments [45, 88, 99], a selected species is excited and ionized, hence this excited species will be detected. In hole-burning experiments, this species is removed from the sample (burned out), e. g. no longer observed in a following spectroscopic experiment. We plan to use a ns ("burn")-fs (pump-probe) combination of pulses to get time-resolved information about the selected (burnt) isomer. The principle of a such experiment is illustrated in fig. 7.1. We assume for simplicity that only two isomers are in the molecular beam. If their excited states are close in energy, a fs pump pulse will excite both isomers and we can not selectively assign the dynamics of the isomers. Instead, a ns laser pulse could be used to selectively excite only one isomer prior the fs pump-probe measurements. Because of its narrow bandwidth (0.07 cm^{-1} = 2.1 GHz) and a tunable output, the ns pulse excites one particular vibrational transition of isomer 1. Because of the high power of the ns

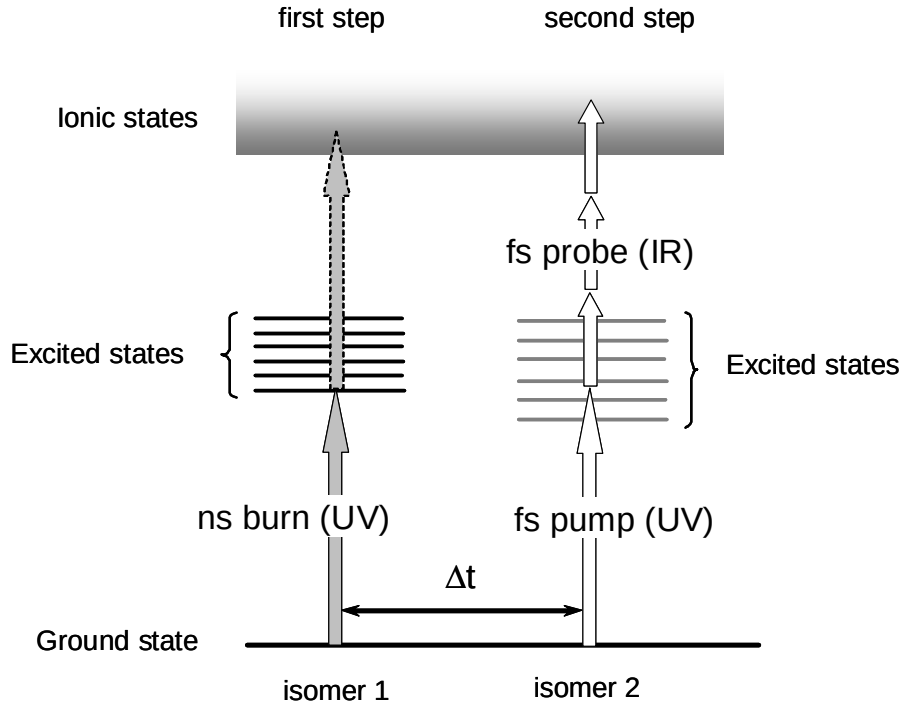

Figure 7.1: Schematic depiction of the hole-burning experiment for the case of two isomers. The ns "burn" laser depletes a resonant transition in one of the isomers by photoexcitation or possibly multiphoton ionization. The remaining isomer is excited (1 UV photon) and ionized (3 IR photons) with the fs laser to measure pump-probe spectra.

laser, this transition will be saturated and the ground state of this isomer will be depleted. The depletion can occur via ionization (isomer 1, shown with the dotted arrow) or through fragmentation of excited species. In both cases the isomer 1 is removed from the molecular beam. After a time delay Δt, a fs pump and a fs probe pulses interact with the remaining isomer 2, the time-resolved excited state dynamics of which can be then analyzed. If several isomers are present in the molecular beam, the dynamics of each can be extracted by burning out one isomer after the other by the ns hole-burning.

7.2 Experimental setup

To carry out the combined ns-fs experiments no modifications to the fs setup was done. The ns pulses were obtained from a dye laser (Spectra Physics, PDL-3) operated with Rhodamine 6G , which was pumped with the second harmonic of a Nd:YAG

(532 nm) laser (Spectra Physics, GCR-270). The tunable output of the dye laser was frequency doubled in an autotracking nonlinear crystal with a wavelength extender (Quanta-Ray, WEX-2). The resulting ns UV pulses crossed the molecular beam, counterpropagating the fs pulses. The molecules in the molecular beam interacted first with the ns pulse and then with the fs pulses. Since the ns laser created a large number of ions that were not of interest, and had to be removed from the interaction region, the fs laser was delayed in time. The ns ions were removed with an electric field, accelerating the ions away from the detector. Neutral excited molecules continued flying with the molecular beam velocity and interacted with the fs laser. To compensate the introduced time delay the two laser beams were spatially moved apart by distance D as shown in fig. 7.2. After the interaction with both lasers, the

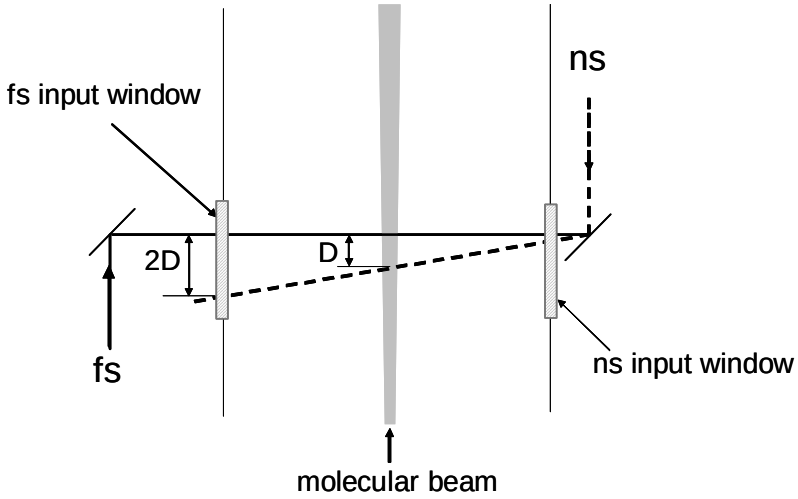

Figure 7.2: Top-view of the ns and fs laser beams crossing the molecular beam in the vacuum chamber for the hole-burning experiments.

ions formed by fs pump-probe ionization were collected in the mass-spectrometer.

The synchronization in time between the ns and the fs lasers was possible via a chain of frequency dividers and delay units as shown in fig. 7.3. We had to decrease the 1 kHz repetition rate of the fs laser to ∼100 Hz to match the repetition rate of the pulsed valve. The ns laser operated at 10 Hz and a second pulse divider was introduced to convert 100 Hz into 10 Hz. This frequency with a certain delay was used to trigger the flash lamps and Q-switch of the ns laser. The output of the lasers was measured with photodiodes (PD (ns) and PD (fs)) and displayed on an oscilloscope. The delay Δt was adjusted to be constant for our measurements.

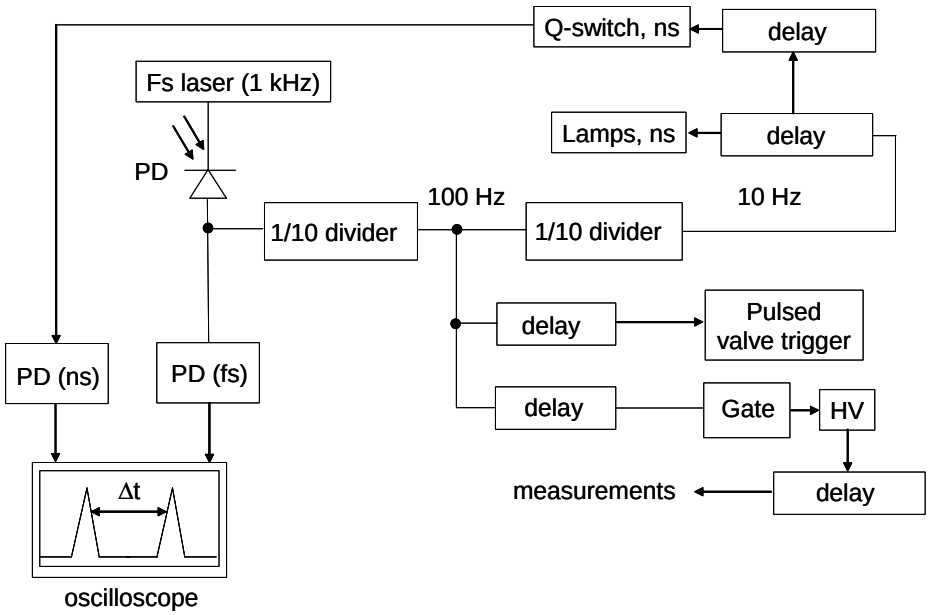

Figure 7.3: Block diagram of the synchronization of ns and fs lasers for hole-burning experiments.

7.3 First results

7.3.1 High-resolution spectroscopy of indole

We started the hole-burning experiments with the measurement of REMPI spectra of the indole molecule, because it has a good absorption in UV spectral range of DNA base absorption and it can be easily evaporated without heating. For REMPI experiments, the ns laser was tuned between 277.5 and 284.5 nm to cover the wavelength range of the 0-0 transition and several higher vibrational bands [100–102]. The resulting spectrum is shown in fig. 7.4. The displayed spectrum was composed of three measurements in different wavelength intervals. The intervals where the signal dropped to zero between 280 and 281 nm are due to a failure of the WEX autotracking mechanism. The amplitudes of the 0-0 band and the remaining peaks can not be compared because they were measured at different days. The position of the 0-0 band of indole was found at 283.76 nm, which is in good agreement with the literature values of 283.78 nm ([100]), 283.82 nm ([101]), and 283.68 nm ([102]). The other bands (marked with circles) were assigned to different vibronic transitions ([102, 103]). The bands marked with stars were not found in literature and may be due to “hot” bands due to transitions from higher vibrational levels of the ground

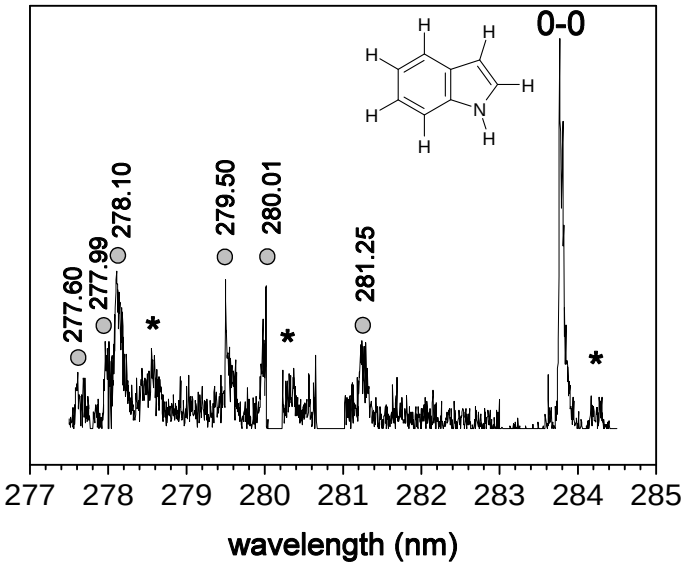

Figure 7.4: Jet-cooled R2PI spectrum of indole. The highest band is the 0-0 transition of indole. Peaks marked with filled circles are vibronic bands, whereas peaks marked with stars are "hot" bands. The bands were assigned according to ref. [102].

state or due to the presence of clusters. This spectrum of indole was obtained in the early days of our spectroscopic efforts and is therefore not of the spectroscopic quality of literature spectra. The observed bands are broad due to power broadening in the high intensity of the ns laser. The signal-to-noise was rather poor due to saturation effects. Spectra with better resolution and S/N ratio were measured for individual lines only.

7.3.2 Hole-burning of indole

A first necessary requirement for the hole-burning experiments is that the same molecules interact with the ns and the fs lasers pulses. If this condition is fulfilled, we expect a drastic decrease of the fs signal due to a reduced number of ground state indole molecules. The ns laser was tuned to the 0-0 transition of indole (283.76 nm). Only a single fs beam with a wavelength of 275 nm was used for resonant femtosecond 2-photon ionization (no pump-probe experiments). The time delay between the fs and the ns laser pulses was set to 650 ns to have enough time to remove the ns ions.

The two laser beams were separated in space by introducing a small angle between the fs and ns beams, as shown in fig. 7.2. The distance D inside the chamber was determined by measuring the distance $2D$ outside the chamber. We estimated the expected D value for our hole-burning experiments based on the speed of sound in Helium, which was used as a carrier gas, and the delay time of 650 ns. With the speed of sound of 965 m/s in helium [1], the estimated D was 0.63 mm. The ns beam was then scanned in vicinity of this position along the X- and Y-axis until the population hole was found. An example of the population hole is given in fig. 7.5. The

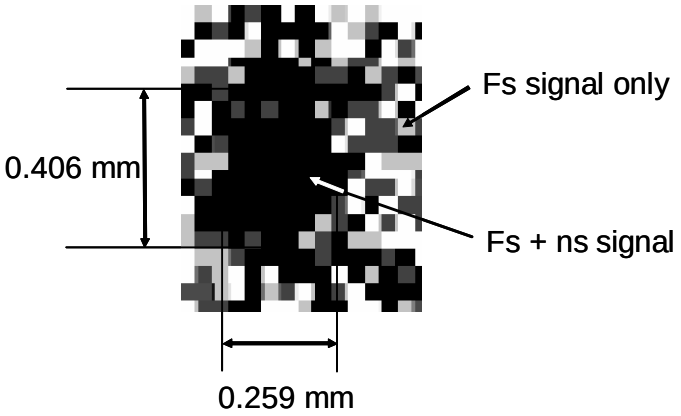

Figure 7.5: Image of the ns-fs population hole.

spatial dimensions of the hole were estimated from the number of scanning steps and the known beam displacement D per step. Longitudinal and transversal dimensions were 290 × 1.4 μm = 0.406 mm, and 140 × 1.85 μm = 0.259 mm, respectively. We also estimated the molecular beam velocity. From the obtained image of the hole, we recalculated the flight distance of the molecular beam in the chamber, which was 700 steps × 1.4 μm = 0.98 mm (longitudinal direction). This distance and the time delay between the laser pulses of 650 ns gave a molecular beam velocity of 1507.7 m/s. This value is significantly higher than the speed of sound in helium (965 m/s), which confirms the supersonic nature of the molecular beam.

[1] at 101325 Pa, 0 °C

Chapter 8

Conclusions

This thesis addressed important questions related to photophysical properties of DNA and its photostability. Experimental results supported by theoretical calculations shed new light on fundamental photoinduced processes in isolated DNA biochromophores and small clusters. Using a reductionist approach, a small model system 2-aminipyridine dimer, isolated DNA bases and base pairs, as well as small clusters with water were investigated. This approach can possibly help to understand complex photophysics of DNA by extrapolating detailed knowledge about simple DNA constituents.

To investigate isolated DNA bases and clusters in the molecular beam, a unique combination of femtosecond electron-ion coincidence spectroscopy (FEICO) and time-resolved pump-probe measurements was applied (Chapter 2). By analyzing electron-ion coincidence spectra and extracting information about electron kinetic energy, it was possible to directly assign the character of excited electronic states in multiple cluster species simultaneously. The life times of the excited states were determined with help of the pump-probe technique, where the pump pulse resonantly excited the species in the molecular beam and the probe pulse probed changes in the excited states by ionization.

The information obtained about the electronic structure and the time-dependent behavior of the electronically excited states allowed us to conclude that a key to the high intrinsic photostability of DNA could be the rapid decay from the electronic excited states to the stable ground state.

For a mimetic base pair model system 2-aminopyridine dimer (Chapter 3) dynamic data revealed a photoinduced H-transfer in a hydrogen-bound dimer. As predicted by theory, the same H-transfer reaction can be an efficient mechanism for excited state

quenching in DNA base pairs, thereby providing a high resistance to photoinduced damage for the genetic information. In the 2-aminopyridine dimer, the H-transfer, indeed, caused a shortening of the excited state life time by two orders of magnitude compared to the monomer, from 1.5 ns to 50-90 ps. Only a slight variation in the excited state life time (50-90 ps) was observed with different excitation energies. A relatively large isotope effect was observed which is in accordance with the moderate energetic barrier along the reaction coordinate found by our *ab initio* calculations. It was also shown experimentally that the H-transfer takes place in some cluster isomers of the 2-aminopyridine trimer, whereas it was not observed in the tetramer which – according to calculations – does not form Watson-Crick type bonds.

The next challenging question was whether the predicted intermolecular H-transfer plays a role in photophysics of DNA base pairs and whether this reaction can be observed and investigated? Isolated bases adenine and thymine were studied first to identify excited state properties in the monomers (Chapter 4). It was shown with the coincidence electron and pump-probe spectroscopy that intramolecular relaxation via low-lying $\pi\pi^*$ and $n\pi^*$ electronic states is a general relaxation mechanism in both bases upon 266 nm photoexcitation. The life times of the light absorbing $\pi\pi^*$ states were found to be extraordinary short, $\sim$100 fs for A and T, whereas dark $n\pi^*$ states have longer life times: 1.3 ps for A, and 7 ps for T. The experimental results were in good agreement with high-level theoretical calculations. No $\pi\sigma^*$ electronic states were observed, but these states could be involved in the excited state relaxation of the DNA bases at higher excitation energies. Therefore, the data obtained allow to conclude that isolated DNA bases should be highly stable against photodamage because of their ultrashort excited state life times.

To investigate DNA base pairs (Chapter 4), coincidence electron spectroscopy and pump-probe measurements were carried out. Although interpretation of the results was hampered by cluster fragmentation, it was shown that excited state dynamics of DNA base pairs adenine-adenine (A-A), thymine-thymine (T-T), and adenine-thymine (A-T) on the short time scale is dominated by the dynamics of $\pi\pi^*$ and $n\pi^*$ states in the monomer constituents. In the A-A base pair, only intramolecular processes were identified, and the dynamics and the electron spectra of the cluster were similar to those of the monomers. In A-T and T-T base pairs, additional longer-lived (37 ps, 40-50 ps) transients were observed, and were assigned to an intermolecular interaction within the clusters. Further theoretical studies are necessary to identify the slower relaxation process unambiguously. Moreover, no direct observation of a fast

intermolecular H-transfer in the A-T base pair was made in our experiments despite predictions by *ab initio* theory. Two reasons can explain this: (1) the Watson-Crick tautomer is not the most stable tautomer in the gas phase and its contribution to the observed excited state dynamics can be small, (2) electronic states involved in the H-transfer reaction are energetically high and are not accessible under our experimental conditions.

It was also demonstrated, that an aqueous environment affects excited state properties of DNA bases and base pairs (Chapter 5). The excited state dynamics of hydrated bases and base pairs was found to be drastically different from those of the isolated bases. In the dynamics of hydrated monomers, only a fast decay (<100 fs) was observed. A possible role of a $\pi\sigma^*$ state may explain this observation, assuming that this state can be stabilized in a polarizable environment and may thus become an efficient excited state quencher. For hydrated thymine, other quenching mechanisms were proposed, such as a conical intersection between the light absorbing $\pi\pi^*$ and the ground state. Such a conical intersection may lead to a very fast relaxation of the excited state. In contrast to microhydrated A, microhydrated A-A dimer exhibited a long-lived excited state. This excited state was suggested to be an excimer state and was assigned to a stacked A-A configuration as opposed to the H-bound configuration in the non-hydrated A-A base pair.

Outlook

Although this thesis discovered many interesting aspects concerning the excited state photophysics of DNA constituents with and without environment, some of the questions discussed here require additional investigation. Introduction of an isomer-selective hole-burning method (Chapter 7) would bring DNA base pair research to a new level. The separate investigation of different tautomers, including the Watson-Crick tautomer, could prove or disprove the predicted H-transfer in DNA base pairs. Also, isomer-selective measurements could help to distinguish native cluster dynamics from fragmentation processes. Another question which was not considered in this thesis is the excited state dynamics of the guanine-cytosine base pair. As guanine thermally decomposes upon heating above 200 °C, it could not be studied at the current experimental conditions. A new molecular source based on laser ablation is needed to study such nonvolatile molecules. Decomposition of molecules is then avoided by rapid cooling in the molecular beam after laser ablation. This method

would also allow to study bigger biologically relevant molecules (e.g. nucleosides, nucleotides, peptides etc.) Additionally, high-level theoretical calculations are required for a complete understanding of some results presented here, e.g., the identification of the long-lived states in thymine, adenine-thymine and thymine-thymine clusters.

All mentioned improvements of the experimental method are currently in progress and, when completed, will bring new insights into the challenging DNA photophysics.

Appendix A

Characteristic parameters of time-of-flight mass and electron spectrometers

Table A.1: Characteristic parameters of time-of-flight mass and electron spectrometers used in this thesis (see fig. A.1 and fig. A.2).

Mass spectrometer		
Length of the TOF mass spectrometer	L_{MS}	40-106 cm
Total extraction voltage for ions	U_{tot}	700-2000 V
Voltage applied in the repeller region	U_{rep}	$\sim 10\% U_{tot}$
Voltage applied in the accelerator region	U_{acc}	$\sim 90\% U_{tot}$
Length of the repeller region	L_{rep}	1 cm
Length of the accelerator region	L_{acc}	5 cm
Electron spectrometer		
Length of the TOF electron spectrometer	L_{ES}	50 cm
Magnetic field in the interaction region	B_{strong}	100-150 mT
Magnetic field gradient in the interaction region	$\frac{\Delta B}{\Delta z}$	22 T/m
Distance between the magnets	d_m	1 cm
Molecular beam and laser beams		
Diameter of the skimmer orifice	D_{sk}	1 mm
Slit (two razer blades at 45 °C to limit the molecular beam) size	d_{slit}	1 mm
Size of the molecular beam (in the interaction region)	d_{MB}	2-3 mm
Volume of the interaction region	$V_{INT.R}$	~ 0.016 mm^3
Diameter of laser beams	D_{LAS}	~ 100 μm
Distance between the valve and the skimmer	d_{v-sk}	~ 5 cm

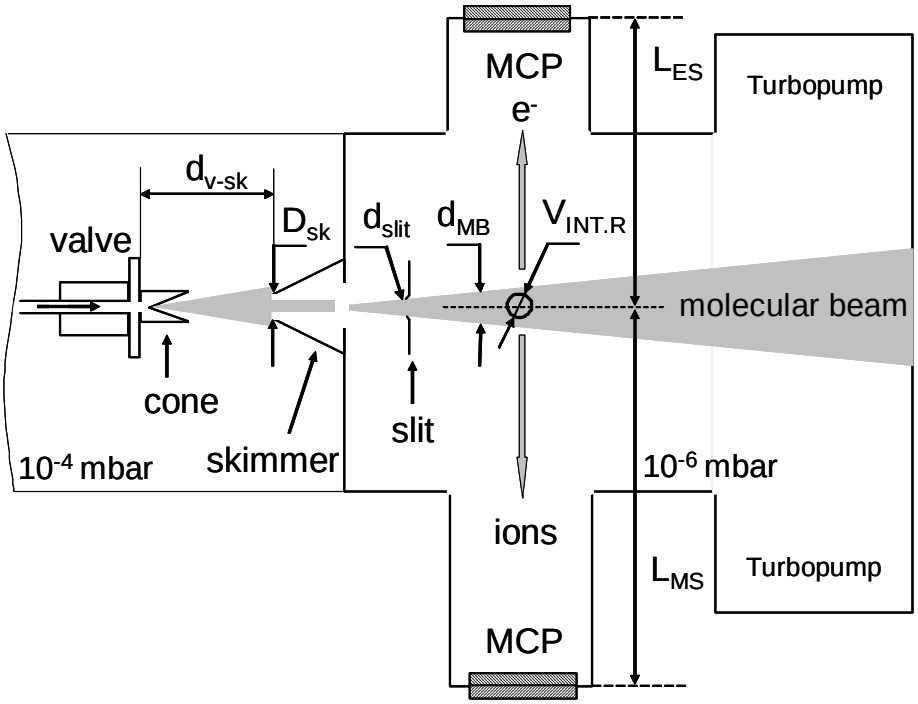

Figure A.1: Schematic representation of the experimental apparatus in a coincidence setup (proportions are not kept).

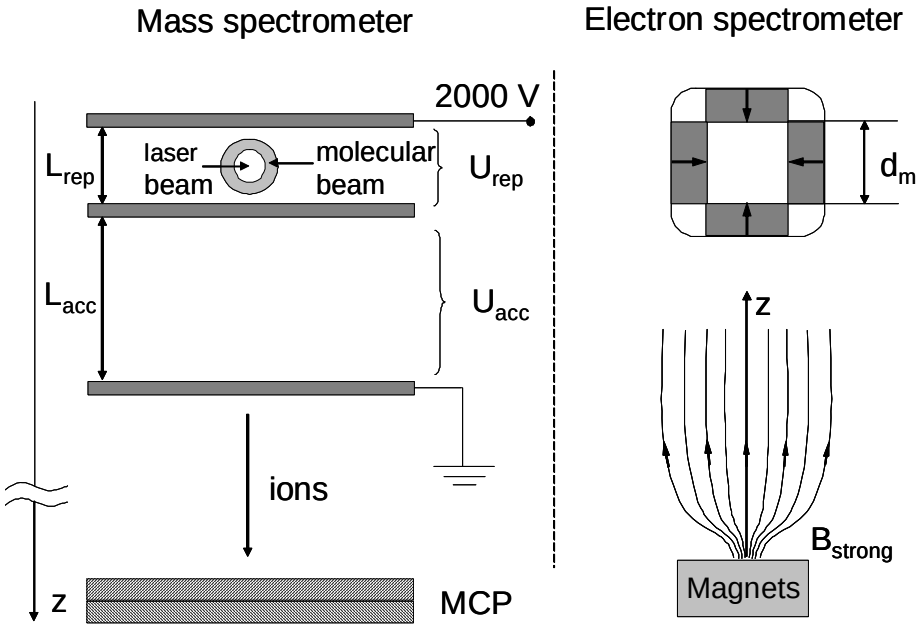

Figure A.2: Schematic representation of the mass and electron spectrometers (proportions are not kept).

Appendix B

Brief glossary of chemical notations used

Although, this thesis is an experimental work, many experimental results presented here are compared with theoretical calculations. Some *ab initio* calculations were performed in our group by Dr. H.-H. Ritze, some were done in collaboration with other groups (Dr. M. Kabeláč, Prof. L. González), and additionally we also discuss theoretical calculations from literature. A simple glossary for the terms used in the text are given below.

Orbitals

While describing the experimental results we referred to different types of the excited states: optically bright $\pi\pi^*$ states, and dark $n\pi^*$ and $\pi\sigma^*$ states. Assuming that only one electron changes its state, in the electro-magnetic field these excited states are formed by a transition of the electron from a highest occupied molecular orbital (HOMO) – n, π to a lowest unoccupied molecular orbital (LUMO) – π^*, σ^*. The shape of a molecular orbital (MO) is a space within which an electron belonging to that orbital spends 95 % (or some other arbitrary fraction) of its time. While detailed computation of these shapes from the Schrödinger theory may be extremely difficult, a very good qualitative idea of their approximate shape may be obtained by considering molecular orbitals to be made up of sums and differences of the atomic orbitals of the constituent atoms – linear combination of atomic orbitals (LCAO) approximation. For a simple example, a diatomic molecule, one can imagine the formation of two different molecular orbitals whose wavefunctions would be

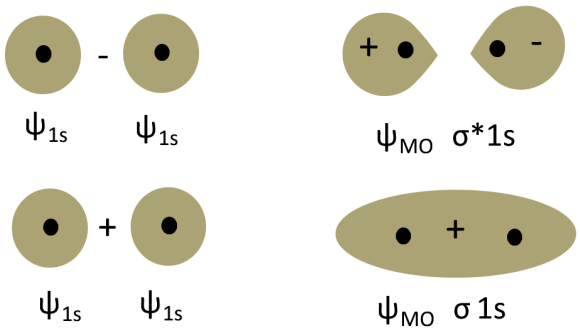

Figure B.1: Bonding ($\sigma 1s$) and antibonding ($\sigma^* 1s$) molcular orbitals for H_2 molecule.

$$\psi_{MO} = \psi_1 \pm \psi_2 \tag{B.1}$$

where ψ_1 and ψ_2 are the relevant atomic orbitals of the two atoms. For an example a hydrogen molecule (H_2), molecular orbitals are built as

$$\psi_{H_2} = \psi_{1s} + \psi_{1s}. \tag{B.2}$$

This molecular orbital is called bonding ($\sigma 1s$). The other orbital, which is formed as

$$\psi_{H_2} = \psi_{1s} - \psi_{1s} \tag{B.3}$$

is called antibonding ($\sigma^* 1s$). Fig. B.1 shows shapes of the two orbitals. Plus and minus indicate the sign of the wavefunction. Two $2s$ atomic orbitals can form $\sigma 2s$ and $\sigma^* 2s$ bonding and antibonding orbitals with identical shape to $\sigma 1s$ and $\sigma^* 1s$ orbitals but larger and with higher energy.

Two $2p$ orbitals can overlap in two different ways depending on their relative orientation. Fig. B.2 shows the two types of overlapping (horizontal, top and vertical, bottom) and shapes of molecular orbitals for a sum and a difference of the $2p$ atomic orbitals. In case of the horizontal overlap, the resulting MOs are of a σ-type (bonding σ and antibonding σ^*). For the vertical overlap, 2p orbitals form π-type molecular orbitals (bonding π and antibonding π^*).

For molecules containing a big number of atoms, molecular orbitals can have significantly more complex shapes. In fig. B.3 we show examples of molecular orbitals for thymine calculated with the *ab initio* method (see also ref.[84]). Only the orbitals for the relevant electronic states are shown.

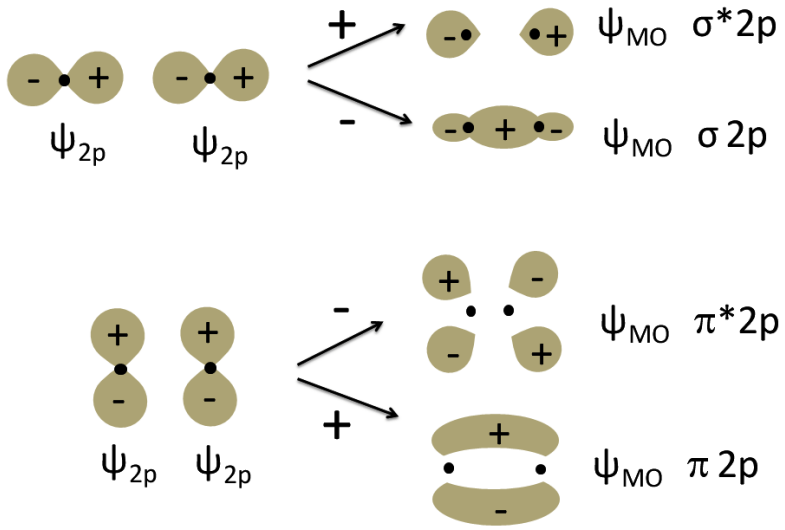

Figure B.2: Bonding ($\sigma 2p$, $\pi 2p$) and antibonding ($\sigma^* 2p$, $\pi^* 2p$)) orbitals for H_2 molecule.

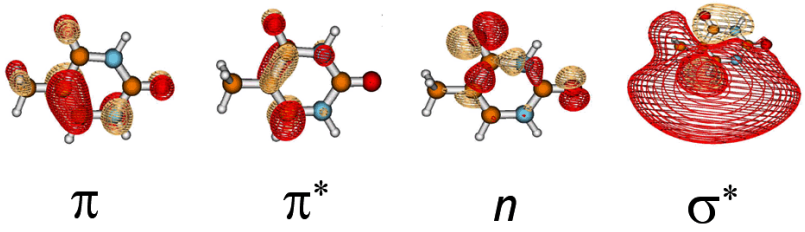

Figure B.3: Orbitals involved in the lowest singlet excited states of the canonical form of thymine [84].

Methods

Ab initio methods are methods of quantum mechanical calculations independent of any experiment other than the determination of fundamental constants. The methods are based on the use of the full Schrödinger equation to treat all the electrons of a chemical system. In practice, approximations are necessary to restrict the complexity of the electronic wavefunction and to make its calculation possible.

To start *ab initio* calculations one has to select a basis set – a set of functions used to create the molecular orbitals, which are expanded as a linear combination of such functions with the weights and coefficients to be determined. In the calculations described in the text, aug-cc-pVDZ and aug-cc-pVTZ data sets were used. They

belong to basis sets developed by Dunning and coworkers and designed to converged systematically to the complete basis set limit using extrapolation techniques. Double zeta (DZ) and triple zeta (TZ) valence (V) basis sets contained polarization functions (p) and are correlation consistent (cc). They were augmented (aug) with diffuse functions to describe properly states of Rydberg character ($\pi\sigma^*$).

To calculate ground and excited state energies as well as to determine ionization potentials, RI-MP2 and RI-CC2 approaches were used. Resolution-of-the-identity (RI) is a numerical approximation to calculate Coulomb integrals. Møller-Plesset perturbation theory of the second order (MP2) was used to take into account electron correlation effects. Better results however can be obtained with the second order coupled-cluster (CC2) approximation method because it gives good results also for excited states. Multi-configurational self-consistent-field (MCSCF) is a general method for obtaining qualitatively correct wavefunctions for highly strained molecules. The most commonly used MCSCF procedure is the complete-active-space self-consistent-field approach (CASSCF), which includes all possible determinants that can be formed by distributing a set of active electrons among a set of active orbitals. Dynamic correlation energy of a molecular system can be then calculated using CASPT2 – complete-active-space second-order-perturbation theory – which gives a second order perturbation estimate of the full configuration interaction (CI) energy using the CASSCF wavefunction of the system. The CASPT2 method was also used to obtain ionization potentials, since RI-CC2 breaks down for low-lying cationic excited states.

Other notations

For interpretation of some of the experimental and theoretical results we often used terms “isomer” and “tautomer”. **Isomers** are compounds with the same molecular but different structural formulae. There are two main forms of isomerism: structural isomerism and stereoisomerism. In structural isomers, atoms are joined together in different ways, e. g., chain isomerism, position isomerism and functional group isomerism. In stereoisomers the bond structure is same, but geometrical positioning of atoms and functional groups in space differs, e. g., cis-trans isomers, conformers, rotamers. **Tautomers** are structural isomers of organic compounds that readily interconvert by a chemical reaction. Commonly this reaction results in a formal migration of hydrogen atom or proton, accompanied by a switch of a single bond and adjacent double bond, e. g., keto/enol tautomerism, where the proton is alternatively on the carbon or oxygen.

For interpretation of the electron-ion coincidence spectra, we used the **Koopmans theorem**, which relates experimental ionization potentials with energy levels of molecular orbitals. The theorem states that the ionization potential required to remove an electron from from the orbital is given by the negative value of the energy of the orbital. Koopmans theorem assumes that the distribution of the remaining electrons remains unchanged. If ions are formed in different electronic excited states, it corresponds to different first vertical ionization potentials; the lowest of them is simply called "ionization potential".

Bibliography

[1] Ryan, W. L.; Gordon, D. J.; Levy, D. H. *J. Am. Chem. Soc.*, **2002**, *124*(21), 6194–6201.

[2] Southern, C. A.; Levy, D. H.; Florio, G. M.; Longarte, A.; Zwier, T. S. *J. Phys. Chem. A*, **2003**, *107*(20), 4032–4040.

[3] Zewail, A. *J. Phys. Chem. A*, **2000**, *104*, 5660–5694.

[4] Stolow, A.; Bragg, A.; Neumark, D. *Chem. Rev.*, **2004**, *104*, 1719–1757.

[5] Hertel, I. V.; Radloff, W. *Rep. Prog. Phys.*, **2006**, *69*, 1897–2003.

[6] Crespo-Hernandez, C. E.; Cohen, B.; Hare, P. M.; Kohler, B. *Chem. Rev.*, **2004**, *104*, 1977–2019.

[7] Sobolewski, A. L.; Domcke, W. *Chemical Physics*, **2003**, *294*, 73–83.

[8] Miller, D. R. *Atomic and molecular beam methods, edited by Scoles, G., Oxford University Press, New York*, **1988**, *Vol.1.*

[9] Levy, D. H. *Annu. Rev. Phys. Chem.*, **1980**, *31*, 197–225.

[10] *General valve (user manual), Parker Instrumentation.*

[11] Wiley, W. C.; McLaren, I. H. *Review of Scientific Instruments*, **1955**, *26*(12), 1150–1157.

[12] Lippert, H. *PhD thesis, Freie Universität Berlin*, **2005**.

[13] Kruit, P.; Read, F. H. *J. Phys. E*, **1983**, *16*, 313–324.

[14] Albritton, D. L.; Schmeltekopf, A. L.; Zare, R. N. *J. Chem. Phys.*, **1979**, *71*(8), 3271–3279.

[15] Jarvis, G. K.; Evans, M.; Ng, C. Y.; Mitsuke, K. *J. Chem. Phys.*, **1999**, *111*(7), 3058–3069.

[16] Stert, V.; Radloff, W.; Freudenberg, T.; Hertel, I. V.; Jouvet, C.; Dedonder-Lardeux, C.; Solgati, D. *Europhys. Lett.*, **1997**, *40*, 515–520.

[17] Stert, V.; Radloff, W.; Schultz, C. P.; Hertel, I. V. *Eur. Phys. J. D*, **1999**, *5*, 97–106.

[18] Svelto, O. *Principles of lasers, Plenium Press, New York*, **1998**.

[19] Douhal, A.; Kim, S. K.; Zewail, A. H. *Nature*, **1995**, *378*, 260–263.

[20] Takeuchi, S.; Tahara, T. *Chem. Phys. Lett.*, **2001**, *347*, 108–114.

[21] Sakota, K.; Hara, A.; Sekiya, H. *Phys. Chem. Chem. Phys.*, **2004**, *6*, 32–36.

[22] Sobolewski, A. L.; Domcke, W. *Phys. Chem. Chem. Phys.*, **2004**, *6*, 2763–2771.

[23] Borst, D. R.; Roscioli, J. R.; Pratt, D. W. *J. Phys. Chem. A*, **2002**, *106*, 4022–4027.

[24] Sobolewski, A. L.; Domcke, W.; Hättig, C. *Proc. Natl. Acad. Sci. USA*, **2005**, *102*, 17903–17906.

[25] Abo-Riziq, A.; Grace, L.; Nir, E.; Kabeláč, M.; Hobza, P.; de Vries, M. S. *Proc. Natl. Acad. Sci. USA*, **2005**, *102*, 20–23.

[26] Samoylova, E.; Smith, V. R.; Ritze, H.-H.; Radloff, W.; Kabeláč, M.; Schultz, T. *J. Am. Chem. Soc.*, **2006**, *128*(49), 15652–15656.

[27] Lin, J. L.; Wu, R. H.; Tzeng, W. B. *Chem. Phys. Lett.*, **2002**, *353*, 55–62.

[28] Ritze, H.-H. *Private communication.*

[29] Schultz, T.; Samoylova, E.; Radloff, W.; Ritze, H.-H. *J. Phys. Chem. A*, **2009**, *submitted.*

[30] Mishra, S. M.; Shukla, M. K.; Mishra, P. C. *Spectrochimica Acta Part A*, **2000**, *56*, 1355–1384.

[31] Kang, H.; Jung, B.; Kim, S. K. *J. Chem. Phys.*, **2003**, *118*, 6717–6719.

[32] Fülscher, M. P.; Serrano-Andres, L.; Roos, B. O. *J. Am. Chem. Soc.*, **1997**, *119*, 6168–6176.

[33] Sabio, M.; Sid, T.; Lumma, J. W. C. *J. Phys. Chem.*, **1990**, *94*, 1366–1372.

[34] Hanus, M.; Kabeláč, M.; Rejnek, J.; Ryjacek, F.; Hobza, P. *J. Phys. Chem. B*, **2004**, *108*, 2087–2097.

[35] Marian, C. M. *J. Chem. Phys.*, **2005**, *122*, 104314.

[36] Clark, L. B.; Peshcel, G. G.; Tinoco, J. I. *J. Phys. Chem.*, **1965**, *69*(10), 3615–3618.

[37] Clark, L. B.; Tinoco, J. I. *J. Am. Chem. Soc.*, **1965**, *87*(1), 11–15.

[38] Cohen, B. J.; Goodman, L. *J. Am. Chem. Soc.*, **1965**, *87*(23), 5487–5490.

[39] Daniels, M.; Hauswirth, W. *Science*, **1971**, *171*(3972), 675–677.

[40] Broo, A. *J. Phys. Chem. A*, **1998**, *102*, 526–531.

[41] Sobolewski, A. L.; Domcke, W. *Eur. Phys. J. D*, **2002**, *20*, 369–374.

[42] Perun, S.; Sobolewski, A. L.; Domcke, W. *Chemical Physics*, **2005**, *313*, 107–112.

[43] Perun, S.; Sobolewski, A. L.; Domcke, W. *J. Am. Chem. Soc.*, **2005**, *127*, 6257–6265.

[44] Blancafort, L. *J. Am. Chem. Soc.*, **2006**, *128*, 210–219.

[45] Plützer, C.; Kleinermanns, K. *Phys. Chem. Chem. Phys.*, **2002**, *4*, 4877–4882.

[46] Nix, M. G. D.; Devine, A. L.; Cronin, B.; Ashfold, M. N. R. *J. Chem. Phys.*, **2007**, *126*, 124312.

[47] Kim, N. J.; Jeong, G.; Kim, Y. S.; Sung, J.; Kim, S. K.; Park, Y. D. *J. Chem. Phys.*, **2000**, *113*(22), 10051–10055.

[48] Lee, Y.; Schmitt, M.; Kleinermanns, K.; Kim, B. *J. Phys. Chem. A*, **2006**, *110*, 11819–11823.

[49] Samoylova, E.; Lippert, H.; Ullrich, S.; Hertel, I. V.; Radloff, W.; Schultz, T. *J. Am. Chem. Soc.*, **2005**, *127*, 1782–1786.

[50] Ritze, H.-H.; Lippert, H.; Samoylova, E.; Smith, V. R.; Hertel, I. V.; Radloff, W.; Schultz, T. *J. Chem. Phys.*, **2005**, *122*, 224320.

[51] Canuel, C.; Mons, M.; Piuzzi, F.; Tardivel, B.; Dimicoli, I.; Elhanine, M. *J. Chem. Phys.*, **2005**, *122*, 074316.

[52] Samoylova, E.; Schultz, T.; Hertel, I. V.; Radloff, W. *Chemical Physics*, **2008**, *347*, 376–382.

[53] Ullrich, S.; Schultz, T.; Zgierski, M. Z.; Stolow, A. *J. Am. Chem. Soc.*, **2004**, *126*, 2262–2263.

[54] Satzger, H.; Townsend, D.; Zgierski, M. Z.; Patchkovskii, S.; Ullrich, S.; Stolow, A. *Proc. Natl. Acad. Sci. USA*, **2006**, *103*(27), 10196–10201.

[55] Lührs, D. C.; Viallon, J.; Fischer, I. *Phys. Chem. Chem. Phys.*, **2001**, *3*, 1827–1831.

[56] Gador, N.; Samoylova, E.; Smith, V. R.; Stolow, A.; Rayner, D. M.; Radloff, W.; Hertel, I. V.; Schultz, T. *J. Phys. Chem. A*, **2007**, *111*(46), 11743–11749.

[57] Hünig, I.; Plützer, C.; Seefeld, K.; Loewenich, D.; Nispel, N.; Kleinermanns, K. *ChemPhysChem*, **2004**, *5*, 1427–1431.

[58] Zierhut, M.; Roth, W.; Fischer, I. *Phys. Chem. Chem. Phys.*, **2004**, *6*, 5178–5183.

[59] Gustavsson, T.; Sharonov, A.; Onidas, D.; Markovitsi, D. *Chemical Physics Letters*, **2002**, *356*, 49–54.

[60] Cohen, B.; Hare, P. M.; Kohler, B. *J. Am. Chem. Soc.*, **2003**, *125*, 13594–13601.

[61] Pancur, T.; Schwalb, N. K.; Renth, F.; Temps, F. *Chemical Physics*, **2005**, *313*, 199–212.

[62] Mennucci, B.; Toniolo, A.; Tomasi, J. *J. Phys. Chem. A*, **2001**, *105*, 4749–4757.

[63] Peng, S.; Padva, A.; LeBreton, P. R. *Proc. Natl. Acad. Sci. USA*, **1976**, *73*(9), 2966–2968.

[64] Stolow, A. *Ann. Rev. Phys. Chem.*, **2003**, *54*, 89–119.

[65] Chandra, A. K.; Nguyen, M. T.; Zeegers-Huyskens, T. *J. Phys. Chem. A*, **1998**, *102*, 6010–6016.

[66] Callis, P. R. *Ann. Rev. Phys. Chem.*, **1983**, *34*, 329–357.

[67] Callis, P. R. *Chem. Phys. Lett.*, **1979**, *61*(3), 563–567.

[68] Oraevsky, A. A.; Sharkov, A. V.; Nikogosyan, D. N. *Chem. Phys. Lett.*, **1981**, *83*(2), 276–280.

[69] Reuther, A.; Nikogosyan, D. N.; Laubereau, A. *J. Phys. Chem.*, **1996**, *100*, 5570–5577.

[70] Gustavsson, T.; Sharonov, A.; Markovitsi, D. *Chem. Phys. Lett.*, **2001**, *351*, 195–200.

[71] Brady, B. B.; Peteanu, L. A.; Levy, D. H. *Chem. Phys. Lett.*, **1988**, *147*(6), 538–543.

[72] Ullrich, S.; Schultz, T.; Zgierski, M. Z.; Stolow, A. *Phys. Chem. Chem. Phys.*, **2004**, *6*, 2796–2801.

[73] Kang, H.; Lee, K. T.; Jung, B.; Ko, Y. J.; Kim, S. K. *J. Am. Chem. Soc.*, **2002**, *124*, 12958–12959.

[74] He, Y.; Wu, C.; Kong, W. *J. Phys. Chem. A*, **2003**, *107*(26), 5145–5148.

[75] Lorentzon, J.; Fülscher, M. P.; Roos, B. O. *J. Am. Chem. Soc.*, **1995**, *117*, 9265–9273.

[76] Shukla, M. K.; Mishra, P. C. *Chemical Physics*, **1999**, *240*, 319–329.

[77] Perun, S.; Sobolewski, A. L.; Domcke, W. *J. Phys. Chem. A*, **2006**, *110*, 13238–13244.

[78] Hudock, R. H; Levine, B. G.; Thompson, A. L.; Satzger, H.; Townswnd, D.; Gador, N.; Ullrich, S.; Stolow, A.; Martinez, T. J. *J. Phys. Chem. A*, **2007**, *111*, 8500–8508.

[79] Gustavsson, T.; Banyasz, A.; Lazzarotto, E.; Markovitsi, D.; Scalmani, G.; Frisch, M. J.; Barone, V.; Improta, R. *J. Am. Chem. Soc.*, **2006**, *128*, 607–619.

[80] Morsy, M. A.; Al-Somali, A. M.; Suwaiyan, A. *J. Phys. Chem. B*, **1999**, *103*, 11205–11210.

[81] Urano, S.; Yang, X.; LeBreton, P. *J. Mol. Struct.*, **1989**, *214*, 315–328.

[82] Ha, T.; Gunthard, H. H. *J. Am. Chem. Soc.*, **1993**, *115*, 11939–11950.

[83] Piacenza, M.; Grimme, S. *J. Comp. Chem.*, **2003**, *25*(1), 83–98.

[84] González-Vázquez, J.; González, L.; Samoylova, E.; Schultz, T. *Phys. Chem. Chem. Phys.*, **2009**, *11*, 3927–3934.

[85] Merchan, M.; Gonzalez-Luque, R.; Climent, T.; Serrano-Andres, L.; Serrano-Perez, J. J.; Riguero, M.; Pelaez, D. *J. Phys. Chem. B*, **2006**, *110*, 26471–26476.

[86] Serrano-Perez, J. J.; Gonzalez-Luque, R.; Merchan, M.; Serrano-Andres, L. *J. Phys. Chem. B*, **2007**, *111*, 11880–11883.

[87] Perun, S.; Sobolewski, A. L.; Domcke, W. *J. Phys. Chem. A*, **2006**, *110*, 9031–9038.

[88] Plützer, C.; Hünig, I.; Kleinermanns, K.; Nir, E.; de Vries, M. S. *ChemPhysChem*, **2003**, *4*, 838–842.

[89] Schultz, T.; Samoylova, E.; Radloff, W.; Hertel, I. V.; Sobolewski, A. L.; Domcke, W. *Science*, **2004**, *306*, 1765–1768.

[90] Kim, N. J.; Kang, H.; Jeong, G.; Kim, Y. S.; Lee, K. T.; Kim, S. K. *Proc. Natl. Acad. Sci. USA*, **2001**, *98*(9), 4841–4843.

[91] Kim, N. J.; Kang, H.; Jeong, G.; Kim, Y. S.; Lee, K. T.; Kim, S. K. *J. Chem. Phys.*, **2001**, *115*(15), 702–705.

[92] Schreier, W. J.; Schrader, T. E.; Koller, F. O.; Gilch, P.; Crespo-Hernandez, C. E.; Swaminathan, V. N.; Carell, T.; Zinth, W.; Kohler, B. *Science*, **2007**, *315*, 625–629.

[93] Hwang, C. T.; Stumpf, C. I.; Yu, Y.-Q.; Kenttämaa, H. I. *Int. J. Mass Spectrom.*, **1999**, *182/183*, 253–259.

[94] Hunter, E.; Lias, S. *NIST Chemistry Web Book*.

[95] Russo, N.; Toscano, M.; Grand, A.; Jolibois, F. *J. Comput. Chem.*, **1989**, *19*, 989.

[96] Kabeláč, M.; Hobza, P. *J. Phys. Chem. B*, **2001**, *105*, 5804.

[97] Kabeláč, M.; Hobza, P. *Phys. Chem. Chem. Phys.*, **2007**, *9*, 903–917.

[98] Crespo-Hernandez, C. E.; Kohler, B. *J. Phys. Chem.*, **2004**, *108*, 11182.

[99] Nir, E.; Plützer, C.; Kleinermanns, K.; de Vries, M. *Eur. Phys. J. D*, **2002**, *20*, 317–329.

[100] Hager, J. W.; Demmer, D. R.; Wallace, S. C. *J. Phys. Chem.*, **1987**, *91*, 1375–1382.

[101] Bersohn, R.; Even, U.; Jortner, J. *J. Chem. Phys.*, **1984**, *80*, 1050–1058.

[102] Barstis, T. L. O.; Grace, L. I.; Dunn, T. M.; Lubman, D. M. *J. Phys. Chem.*, **1993**, *97*, 5820–5825.

[103] Bickel, G. A.; Demmer, D. R.; Outhouse, E. A.; Wallace, S. C. *J. Chem. Phys.*, **1989**, *91*, 6013–6019.

Acknowledgements

I would like to thank greatly all my colleagues and friends who contributed into the development of this work.

Prof. I. V. Hertel - for giving me an opportunity to conduct my PhD work at the Max Born Institute, for fruitful discussions, and helpful advices during the work.

Dr. T. Schultz - for being my direct supervisor, who was a "scientific guru" for me and stimulated me during the research work, for his endless optimism and sense of humor, for his support and countless discussions in the frames of this research work and outside, and for spending many hours to carefully read and correct my thesis.

Prof. Robert Bittl - for taking on a responsibility of being my second supervisor and providing helpful comments to this PhD thesis.

Prof. Wolfgang Radloff - for his help in discussion of the experimental results and in writing publications, for his helpful advices concerning the experiments and for reading and correcting my thesis.

Dr. Hans-Hermann Ritze - for participating in the discussions of the results and for providing most of the *ab initio* calculations of this work.

All former and present colleagues, PhD student and technical help: **Dr. V. Stert, Dr. C. P. Schulz, Dr. T. Laarmann, Dr. D. Nolting, Dr. A. Lübcke, Hr. A. Hentschel, Fr. H. Gromilovich, Y. Rulyk, I. Shchatsinin, P. Singh, J. Müller, H. Lippert, M. Boyle, V. R. Smith, A. Stalmashonak, K. Shainurova.**

I would also like to thank our external collaborators:

Prof. L. González and Dr. J. González-Vázquez (Friedrich-Schiller Universität, Jena) - who provided *ab initio* calculations for interpretation of the results on thymine and thymine-water clusters.

Dr. M. Kabeláč (Institute of Organic Chemistry and Biochemistry, Academy of Sciences of the Czech Republic, Prague) - for performing molecular dynamics calculations for 2-aminopyridine clusters.

Prof. W. Domcke (Technische Iniversität München, Garching) and **Prof. A. L. Sobolewski** (Institute of Physics, Polish Academy of Sciences, Warsaw) - for fruitful discussions of the experimental and theoretical results on 2-aminopyridine and DNA bases and base pairs.

Dr. N. Gador, Dr. S. Ullrich, Prof. A. Stolow (Steacie Institute for Molecular Science, National Research Council, Ottawa) - for their help in conducting difficult experiments with DNA base pairs and for discussion and interpretation of the experimental results.

The German Science Foundation (DFG) through Collaborative Research Center SFB-450, TP-4 for financial support of this thesis.

Finally, I would like to thank **my parents** for their support and love during all these years.

Curriculum Vitae

For reasons of data protection,
the curriculum vitae is not included in the online version